



Professorship of Lunar and Planetary
Exploration Technologies
Prof. Dr.-Ing. Philipp Reiß



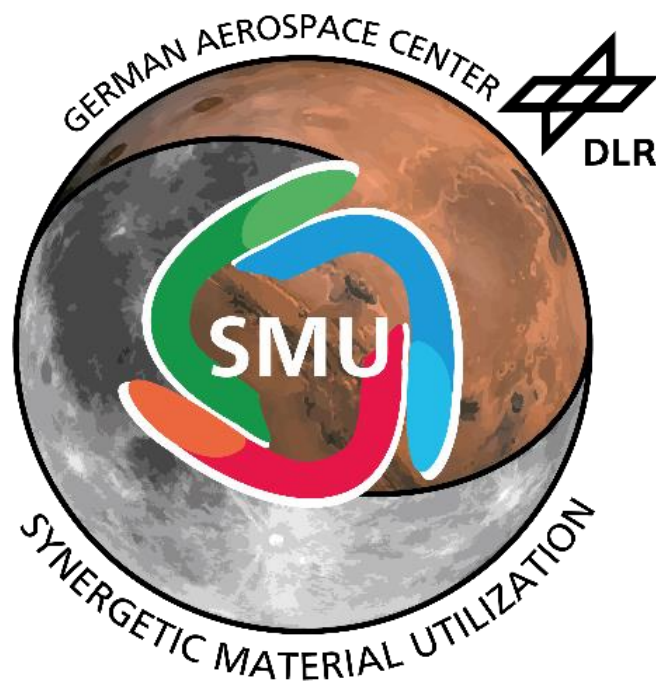
Master's Thesis

Modeling, Simulation and Comparison of Lunar Thermal Water Extraction Methods for Space Resource Utilization

LPE-MA 2022/01

Author:

Niklas Hab



Supervisors:

M.Sc. Luca Kiewiet

Institute of Space Systems, German Aerospace Center

M.Sc. Francisco Javier Guerrero González

Professorship of Lunar and Planetary Exploration Technologies,
Technical University of Munich

LPE-Nummer: LPE-MA 2022/01

Titel der Arbeit: Modeling, Simulation and Comparison of Lunar Thermal Water
Extraction Methods for Space Resource Utilization

Autor: Niklas Hab

Matrikelnummer: 03670105

Erklärung

Mir als vertraulich genannte Informationen, Unterlagen und Erkenntnisse werde ich nach meiner Tätigkeit am Lehrstuhl nicht an Dritte weitergeben.

Ich erkläre mich außerdem damit einverstanden, dass meine Bachelor-, Semester-, Master-, oder Diplomarbeit von der Professur auf Anfrage fachlich interessierten Personen, auch über eine Bibliothek, zugänglich gemacht wird, und dass darin enthaltene Ergebnisse sowie dabei entstandene Entwicklungen und Programme von der Professur für Lunare und Planetare Explorationstechnologien uneingeschränkt genutzt werden dürfen. (Rechte an evtl. entstehenden Programmen und Erfindungen müssen im Vorfeld geklärt werden.)

Ich erkläre außerdem, dass ich diese Arbeit ohne fremde Hilfe angefertigt und nur die in dem Literaturverzeichnis angeführten Quellen und Hilfsmittel benutzt habe.

Ottobrunn, den 25.11.2022



Unterschrift

Zusammenfassung

Die In-situ-Ressourcennutzung (ISRU) gilt als Schlüssel für eine beständige und nachhaltige Erforschung des Weltraums durch den Menschen. Insbesondere Wasser ist eine der wichtigsten Ressourcen, da es sowohl zur Lebenserhaltung als auch zur Herstellung von Raketentreibstoff verwendet werden kann. Dafür ist es wichtig zu wissen, welche Methoden am besten geeignet sind, um Wasser zu gewinnen und welche Parameter den Extraktionsprozess beeinflussen können.

Diese Arbeit umfasst die Simulation und den Vergleich von drei verschiedenen thermischen Wasserextraktionsmethoden: 1) Oberflächenbeheizung, 2) beheizte Bohrstäbe und 3) Erhitzung in einer Heizkammer. In einer Parameterstudie wurde der Einfluss unterschiedlicher Eisgehalte von 1 Gew.-% bis 15 Gew.-% und einer Leistung von max. 2,5 kW auf die durchschnittliche Extraktionsrate und die Energieeffizienz des Systems untersucht. In Anbetracht der geringen Designtreue umfasst die Bewertung auch Kriterien wie Lebensdauer, Zugänglichkeit von Wasser-Eis und Komplexität.

Generell hat sich vor allem die geringe Wärmeleitfähigkeit des Regoliths als wesentlicher Engpass für die thermische Extraktion herausgestellt. Außerdem wurde festgestellt, dass der Wassergehalt des Bodens den größten Einfluss auf den Ertrag hat, da er die thermophysikalischen Eigenschaften des Regoliths stark beeinflusst.

Es wurde festgestellt, dass die Heizkammer die beste Methode darstellt, um Wasser zu extrahieren, da sie thermisch isoliert und ein vollständig geschlossenes System ist. Maximal hat die Heizkammer eine durchschnittliche Extraktionsrate von bis zu ~ 0,9 kg/h für eine optimierte Heizdauer (Oberflächenheizung: ~ 0,09 kg/h; beheizte Stäbe: ~ 0,32 kg/h). Das Design hat jedoch Nachteile im Vergleich zur Oberflächenbeheizung und den beheizten Stäben, z.B. in Bezug auf die Lebensdauer und die Komplexität. Diese müssen für die individuellen Missionsziele berücksichtigt werden müssen.

Abstract

In-situ Resource Utilization (ISRU) is considered to be the key to consistent and sustainable human space exploration. Especially water is one of the most essential resources since it can be used for both life support and rocket fuel production. For that, it is important to know what methods are most suitable to obtain water and what parameters may influence the extraction process.

This work covers the simulation and comparison of three different thermal water extraction methods: 1) in-situ surface heating, 2) heated drills, and 3) heating inside a crucible after excavation. A parameter study was conducted investigating the influence of varying icy deposits from 1 wt.% to 15 wt.% and power inputs of max. 2,5 kW on the average extraction rate and energy efficiency of the system. Given the low fidelity of the designs, the evaluation also includes criteria like lifetime, water ice accessibility, and complexity.

In general, especially the low thermal conductivity of the regolith was shown as a major bottleneck for thermal extraction. Furthermore, the water content of the soil was determined to have the biggest impact on the yield by greatly influencing the thermophysical properties of the regolith.

It was found that the crucible was the best-performing method due to being thermally insulated and a completely closed system reaching an average extraction rate of up to ~ 0,9 kg/h for an optimized heating time (surface heating: ~ 0,09 kg/h; heated rods: ~ 0,32 kg/h). Yet, the design has downsides regarding the lifetime and complexity compared to both surface heating and heating via drills, which need to be considered for individual mission objectives.

Keywords: ISRU, Moon, Water, Optimization, Extraction, Heat and Mass Transfer

Table of Contents

1	INTRODUCTION	2
1.1	Initial Situation and Motivation	2
1.2	Problem Statement and Objective	3
1.3	Scope	4
1.4	Research Methodology and Outline	5
2	THEORETICAL FRAMEWORK	7
2.1	State of Water on the Moon	7
2.1.1	Lunar Water Resource Exploration	7
2.1.2	Form and Distribution of Water Ice	10
2.1.3	Future Exploration Missions	12
2.2	State of the Art	12
2.2.1	Existing Thermal Water Extraction Approaches	13
2.2.2	Heating Methods for Thermal Water Extraction	17
2.2.3	Existing Simulation Approaches	17
2.3	Scientific Gap	19
3	MISSION CONTEXT	21
3.1	Lunar Water Mining Business Case	21
3.2	Scenario description and Use cases	25
3.3	System Requirements and Comparison Methods	27
4	HEAT AND MASS TRANSFER IN LUNAR REGOLITH	30
4.1	Heat Transfer	30
4.1.1	Phase Change & Regolith Density	30
4.1.2	Thermal Conductivity Model	32
4.1.3	Heat Capacity	37
4.2	Mass Transfer	39
4.2.1	Diffusion	40
4.2.2	Advection	42
4.2.3	Sublimation Model	42
5	COMPUTATIONAL SETUP	45
5.1	Implementation of the Models	45
5.1.1	Design variables	45
5.1.2	Assumptions	46
5.1.3	Geometry Description and Boundary Conditions	48
5.1.4	Mesh and Solver Setup	53
5.1.5	Performance Metric	59

5.2	Design Optimization	60
6	RESULTS AND DISCUSSION	62
6.1	Design Parameter Study	62
6.1.1	In-Situ Surface Heating	62
6.1.2	In-Situ Rod Heating	67
6.1.3	Heating inside a Crucible after Excavation	69
6.2	Method Comparison	71
6.2.1	Quantitative Comparison	71
6.2.2	Qualitative Comparison	75
6.2.3	Overview of the Comparison	77
6.3	Additional Regolith and Ambient Parameter Variations	78
7	CONCLUSION	82
8	OUTLOOK	84
A	REFERENCES	85
B	APPENDICES	95
B.1	Lunar Regolith Thermal conductivity model according to Parzinger (2014) and Reiß (2018)	95

List of Figures

FIGURE 1-1: RESERVES VS. RESOURCES REGARDING THEIR ECONOMIC POTENTIAL	3
FIGURE 1-2: SIMPLIFIED ISRU VALUE CHAIN (ISECG 2021)	4
FIGURE 1-3: APPLIED RESEARCH METHODOLOGY WITH THE RELATED CHAPTERS OF THE WORK BASED ON BLESSING AND CHAKRABARTI (2009: P. 15).....	5
FIGURE 2-1: HISTORY OF LUNAR WATER RESOURCES EXPLORATION (SONG ET AL. 2021)	8
FIGURE 2-2: MAP OF WATER EQUIVALENT HYDROGEN (WEH) ABUNDANCE IN THE (A) LUNAR NORTH- AND (B) SOUTH POLE (ADAPTED FROM (SANIN ET AL. 2017))	8
FIGURE 2-3: DISTRIBUTION OF WATER-ICE-BEARING PIXELS (GREEN AND CYAN DOTS) OVERLAIN ON THE DIVINER ANNUAL MAXIMUM TEMPERATURE FOR (A) NORTHERN- AND (B) SOUTHERN POLAR REGIONS (LI ET AL. (2018))	9
FIGURE 2-4: POTENTIAL PHYSICAL TEXTURES OF ICE AND REGOLITH IN LUNAR COLD TRAP ENVIRONMENTS (CANNON 2020).....	11
FIGURE 2-5: SCHEMATIC CROSS-SECTION SHOWING THE EVOLUTION OF POLAR WATER ICE DEPOSITS (CANNON AND BRITT 2020)	11
FIGURE 2-6: IN-SITU THERMAL MINING CONCEPT (SOWERS AND DREYER 2019; KORNUTA ET AL. 2019).....	14
FIGURE 2-7: POSSIBLE COMBINATION FOR CRUCIBLE HEATING WITH A HEATING CHAMBER SETUP (LEFT) (REISS 2018B) AND A BUCKET DRUM EXCAVATOR TO DELIVER THE REGOLITH (RIGHT) (MODIFIED FROM JUST ET AL. (2020)).....	14
FIGURE 2-8: CONSECUTIVE WATER EXTRACTION SYSTEMS WITH HEATING INSIDE THE BOREHOLE: HEATED DEEP-FLUTED AUGER (LEFT) (BASED ON HE ET AL. (2021) AND HEATED DUAL WALL CORING AUGER (RIGHT) (BASED ON ZACNY ET AL. (2016))	15
FIGURE 3-1: PROPELLANT PRICES IN CISLUNAR SPACE (KORNUTA ET AL. 2019; SOWERS 2021)	24
FIGURE 3-2: OVERVIEW OF THE INVESTIGATED DESIGNS.....	25
FIGURE 3-3: PHASE DIAGRAM FOR WATER DISPLAYING THE TEMPERATURE AND PRESSURE- DEPENDENT BOUNDARIES BETWEEN THE SOLID, LIQUID, AND VAPOR PHASES (ZHANG ET AL. 2015)	26
FIGURE 4-1: MATERIAL PHASE INDICATORS θ_1 AND θ_2 , PHASE CHANGE TEMPERATURE T_{pc} AND PHASE CHANGE TRANSITION INTERVAL $\Delta T_{1 \rightarrow 2}$	31
FIGURE 4-2: COMPARISON OF DENSITY AND POROSITY FITS OF DRY LUNAR REGOLITH CONCERNING THE SOIL DEPTH	32
FIGURE 4-3: RATIO OF CONTACT, RADIATION, GAS, AND SOLID-GAS COUPLING FOR THE EFFECTIVE THERMAL CONDUCTIVITY ACCORDING TO REISS (2018A). THE LEFT DASHED LINE INDICATES $KN = 10$, AND THE RIGHT DASHED LINE INDICATES $KN = 0.1$	34
FIGURE 4-4: COMMON THERMAL CONDUCTIVITY MODELS FOR DRY LUNAR REGOLITH AT LUNAR AMBIENT PRESSURES	36
FIGURE 4-5: OVERVIEW OF COMMON SPECIFIC HEAT APPROXIMATIONS FOR DRY LUNAR REGOLITH	38
FIGURE 4-6: APPLICATION RELEVANCE ACCORDING TO THE CORRESPONDING KNUDSEN NUMBER FOR WATER VAPOR PRESSURES p_g AT 400 K (SCHIEBER ET AL. 2020)	40
FIGURE 4-7: MICROSCOPIC IMAGES OF THE LUNAR SIMULANT JSC-1A, INCLUDING (A) FINES < 90 MM, (B) PARTICLES IN THE SIZE RANGE OF 90 MM–150 MM, AND (C) PARTICLES THAT ARE >150 MM (SCHIEBER ET AL. 2020)	41
FIGURE 5-1: GEOMETRY OF THE INVESTIGATED DESIGNS WITH THEIR RESPECTIVE TOP-LEVEL BOUNDARY CONDITIONS: (1) IN-SITU SURFACE HEATING, (2) IN-SITU ROD HEATING (A) WHOLE GEOMETRY B) SIMULATED SECTION), (3) HEATING INSIDE A HEATING CHAMBER AFTER EXCAVATION	49
FIGURE 5-2: ROD CONSTELLATION OF THE INVESTIGATED ROD-HEATING DESIGN (2).....	51
FIGURE 5-3: COMPARISON OF SURFACE EMISSIVITY FITS FOR DIFFERENT LUNAR REGOLITH SIMULANTS (BASED ON MCCLOY ET AL. (2011)).....	53
FIGURE 5-4: VISUALIZATION OF THE MESH USED FOR THE BASELINE IN-SITU SURFACE HEATING.....	55
FIGURE 5-5: SOLUTION ACCURACY PROGRESSION OF THE AVERAGE TEMPERATURE DURING THE MESH REFINEMENT STUDY FOR THE BASELINE IN-SITU SURFACE HEATING	55
FIGURE 5-6: VISUALIZATION OF THE MESH USED FOR THE IN-SITU ROD HEATING	56

FIGURE 5-7: SOLUTION ACCURACY PROGRESSION OF THE AVERAGE TEMPERATURE DURING THE MESH REFINEMENT STUDY FOR THE IN-SITU ROD HEATING	56
FIGURE 5-8: VISUALIZATION OF THE MESH USED FOR THE HEATING INSIDE A CRUCIBLE	57
FIGURE 5-9: SOLUTION ACCURACY PROGRESSION DURING THE MESH REFINEMENT STUDY FOR THE HEATING INSIDE A CRUCIBLE	57
FIGURE 5-10: QUALITY OF THE SKEWNESS OF THE MESH ELEMENTS FOR THE RESPECTIVE EXTRACTION MODELS: A) IN-SITU SURFACE HEATING, B) IN-SITU ROD HEATING, C) CRUCIBLE HEATING.....	58
FIGURE 5-11: FLOWCHART OF THE DESIGN OPTIMIZATION PROCESS (KIEWIET ET AL. 2022)	61
FIGURE 6-1: EXEMPLARY TEMPERATURE DISTRIBUTION AFTER ~17,5 DAYS FOR IN-SITU SURFACE HEATING FOR THE BASELINE CONFIGURATION	63
FIGURE 6-2: DESICCATED VOLUME AFTER ~17,5 DAYS FOR IN-SITU SURFACE HEATING FOR THE BASELINE CONFIGURATION (1: FULLY DESICCATED; 0: FULLY ICY)	63
FIGURE 6-3: TOTAL TIME-DEPENDENT WATER YIELD FOR IN-SITU SURFACE HEATING WITH VARYING WATER CONTENTS	65
FIGURE 6-4: WATER ICE CONTENT AND POWER DENSITY INFLUENCE ON THE EXTRACTION RATE FOR IN-SITU SURFACE HEATING FOR A POWER INPUT OF 1500 W	66
FIGURE 6-5: TOTAL TIME-DEPENDENT WATER YIELD FOR IN-SITU ROD HEATING	68
FIGURE 6-6: EXEMPLARY TEMPERATURE DISTRIBUTION AFTER ~17,5 DAYS FOR IN-SITU SURFACE HEATING FOR THE BASELINE CONFIGURATION (LEFT: 3D CONTOURS; RIGHT: 2D CROSS-SECTION THROUGH THE ROD PLANE)	69
FIGURE 6-7: OUTGASSING ABILITY OF THE WATER VAPOR FOR IN-SITU ROD HEATING WITH AN INITIAL WATER CONTENT OF 5 WT.% (1: FULLY DESICCATED; 0: FULLY ICY): A) 500 W POWER INPUT, B) 1500 W POWER INPUT, C) 1500 W POWER INPUT PLUS ADDITIONAL SURFACE HEATING.....	69
FIGURE 6-8: EXEMPLARY TEMPERATURE DISTRIBUTION AFTER ~17,5 DAYS FOR CRUCIBLE HEATING FOR THE BASELINE CONFIGURATION.....	70
FIGURE 6-9: DESICCATED VOLUME AFTER ~17,5 DAYS FOR CRUCIBLE HEATING FOR THE BASELINE CONFIGURATION (1: FULLY DESICCATED; 0: FULLY ICY)	70
FIGURE 6-10: TOTAL TIME-DEPENDENT WATER YIELD FOR HEATING INSIDE A CRUCIBLE AFTER REGOLITH EXCAVATION	71
FIGURE 6-11: OPTIMIZED TOTAL WATER YIELD FOR IN-SITU SURFACE HEATING AND CRUCIBLE HEATING, CONSIDERING A SYSTEM RELOCATION FOR THE FORMER, AS WELL AS EXTRACTION, EMPTYING, AND REFILLING OF A REGOLITH BATCH FOR THE LATTER.	72
FIGURE 6-12: RELATIVE WATER YIELD FOR VARYING INITIAL REGOLITH TEMPERATURES WITH CORRESPONDENT WATER CONTENTS ACCORDING TO THE USE CASES (LEFT) AND WITH CONSTANT WATER CONTENTS (RIGHT)	79
FIGURE 6-13: PRODUCTION PROGRESSION FOR VARIOUS PHASE CHANGE TRANSITION INTERVALS FOR IN-SITU SURFACE HEATING	79
FIGURE 6-14: IMPACT OF VARYING THERMAL CONDUCTIVITIES OF THE REGOLITH ON THE TOTAL WATER YIELD (AT CONSTANT PRESSURE)	80
FIGURE 6-15: IMPACT OF VARYING SPECIFIC HEAT CAPACITIES OF THE REGOLITH ON THE TOTAL WATER YIELD.....	81

List of Tables

TABLE 2-1: SUMMARY OF THE TOTAL WATER VAPOR, ICE, AND EJECTA DUST IN THE NEAR-INFRARED INSTRUMENT FIELD OF VIEW OF THE LACROSS MISSION (COLAPRETE ET AL. 2010)	9
TABLE 2-2: SUMMARY OF VIABLE THERMAL WATER EXTRACTION METHODS ON THE MOON	16
TABLE 2-3: OVERVIEW OF EXISTING SIMULATION APPROACHES CONCERNING THE GOALS OF THIS WORK.	19
TABLE 3-1: PROPELLANT AND WATER DEMAND FOR INITIAL LUNAR PROPELLANT CUSTOMER SCENARIOS	23
TABLE 3-2: PROPELLANT COST ESTIMATES FROM BOTH EARTH AND THE MOON (KORNUTA ET AL. 2019)	24
TABLE 3-3: TOP-LEVEL REQUIREMENTS FOR THE SYSTEM DESIGNS.....	27
TABLE 4-1. EFFECTIVE THERMAL CONDUCTIVITY MODELS FOR DRY LUNAR REGOLITH (GREY: MODEL CHOSEN FOR THIS STUDY)	35
TABLE 4-2: OVERVIEW OF COMMON SPECIFIC HEAT APPROXIMATIONS FOR DRY LUNAR REGOLITH (GREY: MODEL CHOSEN FOR THIS STUDY).....	38
TABLE 4-3: COMMON MODELS FOR THE SUBLIMATION PRESSURE OF WATER.....	44
TABLE 5-1: OVERVIEW OF THE MODEL VARIABLES FOR THE PARAMETER STUDY WITH VALUES IN BOLD ACCOUNTING FOR THE BASELINE SCENARIO.....	46
TABLE 5-2: MODEL INPUT PARAMETERS CONCERNING THE DEPOSIT STABILITY.....	48
TABLE 5-3: POWER AND POWER DENSITY INFLUENCE ON IN-SITU DOME DIAMETER FOR SURFACE HEATING.....	50
TABLE 5-4: DESCRIPTION OF TOP-LEVEL BOUNDARY AND INITIAL CONDITIONS	53
TABLE 6-1: VOLUME AVERAGED DEPTH AND TOTAL WATER YIELD REACHED BY THE IN-SITU SURFACE HEATING DESIGN AFTER ~17.5 DAYS	64
TABLE 6-2: TOTAL WATER YIELD REACHED BY THE IN-SITU ROD HEATING METHOD AFTER ~ 17,5 DAYS	67
TABLE 6-3: TOTAL WATER YIELD REACHED BY THE CRUCIBLE HEATING METHOD AFTER ~ 17,5 DAYS.....	70
TABLE 6-4: TOTAL WATER YIELD [KG] OF THE RESPECTIVE OPTIMIZED WATER EXTRACTION METHODS.....	73
TABLE 6-5: AVERAGE EXTRACTION RATE [g/h] OF THE RESPECTIVE OPTIMIZED WATER EXTRACTION METHODS.....	74
TABLE 6-6: ENERGY EFFICIENCY [g/kWh] OF THE RESPECTIVE OPTIMIZED WATER EXTRACTION METHODS.....	74
TABLE 6-7: COST ESTIMATING RELATIONSHIPS REGARDING SYSTEM MASSES (SOWERS AND DREYER 2019)	76
TABLE 6-8: QUALITATIVE ASSESSMENT OVERVIEW	78

Symbols

c	Concentration	k_{sg}	Coupling of solid and gas conduction
$C_{p,dry}$	Specific heat of dry regolith	k_{sc}	Physical contact conduction
$C_{p,eff}$	Effective specific heat	k_{rad}	Radiation between particles
$C_{p,g}$	Specific heat of gas	L	Latent heat of sublimation (corrected)
$C_{p,i}$	Specific heat of ice	$L_{1 \rightarrow 2}$	Latent heat of sublimation
$C_{p,icy}$	Specific heat of icy regolith	$m_{sub}(t)$	Sublimated ice mass over time
D	Diffusion coefficient	m_{max}	Maximum mesh size
D_K	Knudsen Diffusion	m_{grow}	Maximum element growth rate
$D_{K,eff}$	Effective Knudsen Diffusion	m_n	Number of elements
D_O	Ordinary Diffusion	m_{sub}	Sublimated water yield
$D_{O,eff}$	Effective Ordinary Diffusion	m_{yield}	Total water yield
d_g	Diameter of gas molecule	n	Normal vector to the surface
d_v	Space between particles	p	Pressure
$d_{v,i}$	Corrected space between particles for icy regolith	\bar{p}	Average pressure
\bar{e}_T	Mean squared error	p_{amb}	Ambient temperature
F	Pore filling fraction	p_g	Gas pressure
g_{grow}	Maximum growth rate	p_{pc}	Sublimation pressure
h	Sample height	q	Normed heat flux
k_b	Boltzmann constant	q_0	Surface heat flux
k_{dry}	Thermal conductivity of dry regolith	Q	Heating power
$k_{dry,0}$	Thermal conductivity of dry regolith (without gas)	Q_m	Mass source
k_{eff}	Effective thermal conductivity	R	Universal gas constant
k_g	Thermal conductivity of gas	r_{yield}	Average extraction rate
$k_{g,0}$	Thermal conductivity of gas in standard conditions	$r_1(t)$	Phase change interphase distance (in-situ)
k_i	Thermal conductivity of ice	$r_2(t)$	Phase change interphase distance (crucible)
k_{icy}	Thermal conductivity of icy regolith	S	Sublimation rate
		s_v	Specific surface area per volume
		s_m	Specific surface area per mass

T	Temperature	$\overline{\theta}_2$	Volume averaged desiccated phase indicator
T_{amb}	Ambient temperature	κ	Permeability of regolith
T_i	Initial temperature	λ	mean free path
T_{pc}	Phase change temperature	μ	Vapor dynamic viscosity
$\Delta T_{1 \rightarrow 2}$	Transition interval of phase change	ρ	Density
t	Time	ρ_{dry}	Particle density of dry regolith
t_c	Cycle time	$\rho_{dry,b}$	Bulk density of dry regolith
t_h	Heating time	$\bar{\rho}_{dry,b}$	Averaged bulk density of dry regolith
Δt_{max}	Max. time step	ρ_{eff}	Effective density of the sample
u	Darcy's velocity field of vapor	ρ_g	Density of gas
w_i	Initial ice content	ρ_i	Particle density of ice
z	sample depth	$\rho_{i,b}$	Bulk density of ice
α_m	Phase change mass fraction	$\rho_{icy,b}$	Bulk density of the icy sample
δ_p	Pore size estimation	φ	Effective porosity regolith
ε_c	Surface emissivity crucible	φ_{dry}	Porosity of the dry regolith
ε_r	Surface emissivity regolith	$\vartheta_{g,a}$	Apparent gas permeability
η	Energy efficiency	$\vartheta_{g,e}$	Gas permeability
θ_1	Phase change indicator icy phase	τ	Tortuosity
θ_2	Phase change indicator dry phase		

Abbreviations

BC	Boundary Condition
DLR	German Aerospace Center
DRM	Design Research Methodology
EML1	First <i>Earth-Moon</i> Lagrange point
GEO	Luxembourg Space Agency
LCROSS	Lunar Crater Observation and Sensing Satellite
LEO	Low Earth Orbit
LPE	Professorship of Lunar and Planetary Exploration Technologies
LSA	Luxembourg Space Agency
NASA	National Aeronautics and Space Administration
PRIME-1	Polar Resources Ice Mining Experiment-1
PROSPECT	Package for Resource Observation and in-Situ Prospecting for Exploration, Commercial exploitation, and Transportation
PSR	Permanently Shadowed Region
SMU	Synergetic Material Utilization
SOFIA	Stratospheric Observatory for Infrared Astronomy
TRIDENT	The Regolith and Ice Drill for Exploring New Terrain
TUM	Technical University of Munich
VIPER	Volatile Investigating Polar Exploration Rover

1 Introduction

1.1 Initial Situation and Motivation

“The Moon has unique significance for all space applications for a reason that to my amazement is hardly ever discussed in popular accounts of space policy. The Moon is the closest source of material that lies far up Earth’s gravity well. Anything that can be made from Lunar material at costs comparable to Earth manufacture has an enormous overall cost advantage compared with objects lifted from Earth’s surface. The greatest value of the Moon lies neither in science nor in exploration, but in its material.”

John Marburger, 2006

After the initial wave of lunar exploration from the 1950s to the 1970s, the interest in the topic has significantly regrown in recent years. In his speech at the Goddard Memorial Symposium in 2006, John Marburger, former Director of Science and Technology Policy in the United States, first emphasizes that the key to not only a future in space exploration but also a sustainable future is by developing and utilizing its local resources. (Marburger 2006)

In-Situ Resource Utilization (ISRU) is defined as the collection, processing, storing, and use of materials encountered during human or robotic space exploration that replace materials that would otherwise be brought from. This is not only believed to significantly reduce the cost of planned or anticipated science, exploration, or commercial missions but also enable said missions, which were not possible before (Sowers and Dreyer 2019; Kornuta et al. 2019). Since beyond earth, the closest and most accessible source of resources is the Moon, it has been the focus of ISRU efforts for many decades (Meurisse and Carpenter 2020). In 2019, the National Aeronautics and Space Administration (NASA) announced the “Artemis Program”, proposing that it will achieve a manned moon landing and establish a lunar base by 2025 (Foust 2019; Smith et al. (2020)).

For this, a broad understanding of the lunar resources, which includes withal the identification of such, the assessment of their utilization potential, abundance, and distribution across the lunar surface is essential (Reiss 2018a). Especially water is seen to be one of the most crucial resources for long-duration space exploration missions and human presence on and around the moon. Recent missions like the Lunar Reconnaissance Orbiter (LRO) with the Lunar Crater Observation and Sensing Satellite (LACROSS) have discovered that stable water ice may exist in abundance in Permanently Shaded Craters (PSRs) on the Moon, which could be extracted and used for drinking water, producing breathable oxygen or rocket propellant (Colaprete et al. 2010; Li et al. 2018).

Recent studies investigated different designs of the water ice extraction process, where especially thermal methods are in the focus (Brisset et al. 2020; Wasilewski 2021b; Song et al. 2021; Schieber et al. 2022). The latter relies on the application of heat to sublime the ice within the regolith and outgas the generated water vapor from the regolith before it can be captured by e.g. depositing the vapor in a cold trap.

1.2 Problem Statement and Objective

Even though in-situ water ice extraction and the whole ISRU process chain with it bear a lot of opportunities for future space exploration, its successful technical implementation, as well as application, are still connected to several challenges, which need to be addressed.

Regarding the technical feasibility, both the extreme lunar environment as well as the uncertainty in the type, amount, thermophysical parameters, and lateral or vertical distribution of water and volatiles, especially in lunar PSRs, are decisive. Together with just recent in-situ measurements from Chang'E5 (Lin et al. 2022), single surface data points collected by the Lunar Crater Observation and Sensing Satellite (LCROSS), are to date the only direct evidence of the presence of water ice on the moon (Gladstone et al. 2010; Colaprete et al. 2010) (see also chapter 2.1). This missing ground truth data makes it difficult for scholars to reach even a preliminary design review for ISRU water or volatile mining hardware and operations.

According to Kleinhenz and McAdam (2021), water so far has only been identified as a *resource*, but its potential for ISRU requires identifying and locating a water *reserve*. In this context, *resources* are defined as geological occurrences that have the potential for practical use, but for which viability has not yet been established, while *reserves* are seen as resources that can be proven to exceed the threshold parameters (e.g., location, spatial extent, grade, chemistry) for at least one engineered system that can extract and process it to within a reasonable definition of success (see Figure 1-1). (Kleinhenz and McAdam 2021)

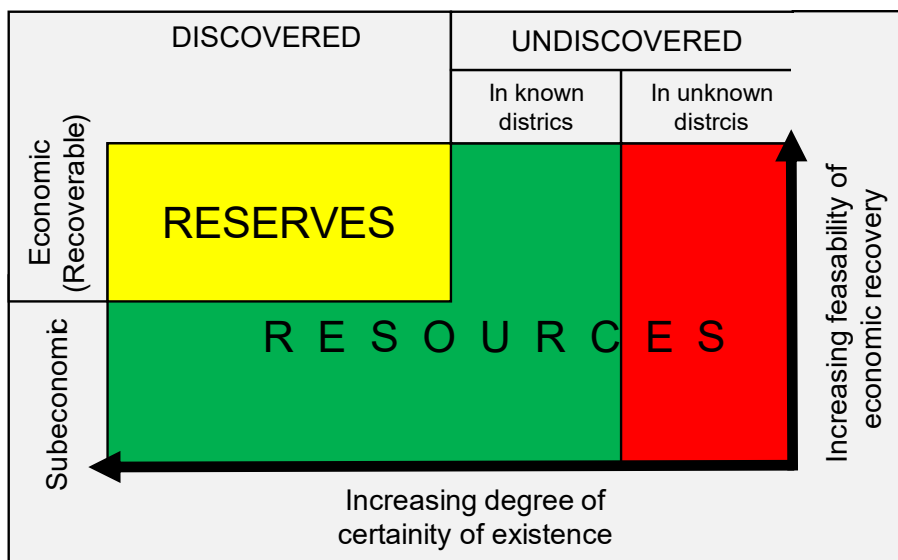


Figure 1-1: Reserves vs. Resources regarding their economic potential

Even though lunar environmental factors are better understood, with its eg. high vacuum, only ~1/6th of Earth’s gravity, very high surface temperature range (down to 20 - 40 K in the PSRs and over 400 K on sunlit areas during the day) (Williams et al. 2019), abrasive dust, or also just difficult-to-access terrain with crater inclinations >30 deg, it still poses major challenges on the overall performance and durability of a system.

In the context of water extraction, while current and future lunar science instruments and missions can provide further critical information, these science-focused efforts may not be sufficient for selecting mining locations, defining requirements for mining hardware designs, and planning mining operations. Thus, with the information available up to date, thermo-fluid simulations of water extraction designs on the Moon are mandatory to determine the most-suited methods for future missions, while efficiency, accessibility, and durability will likely be important design drivers.

Amongst others, these problems are tackled by both the German Aerospace Center' (DLR) recently founded research group on Synergetic Material Utilization (SMU) as well as the Professorship of Lunar and Planetary Exploration Technologies (LPE) at the Technical University of Munich (TUM), which are looking into different thermal methods to extract and capture the water ice form the lunar regolith. This thesis is also part of this effort.

Thus, the central goal of this work includes the modeling and simulation of three different state-of-the-art thermal water extraction methods in the Software *COMSOL Multiphysics* and assessing them regarding a developed performance metric. The latter is consisting of both quantitative as well as qualitative aspects since the fidelity of the designs is likely not enough information to accurately compare them to each other by quantitative measures alone. Thus, the corresponding research question of this thesis is as follows:

What are the most promising methods for thermal water extraction under certain scenarios on the Moon?

For the designs, the water ice content of the regolith, the total power input available to the system, as well as the surface coverage of the heating elements corresponding to the power density are investigated in a parametric study.

1.3 Scope

To be able to utilize locally sourced space resources like water, a sophisticated value chain is required. The ISRU value chain can be enclosed in a simplified five-stage process flowsheet, as seen in Figure 1-2. Yet, this value chain and its building blocks might lead to different value chains depending on the targeted resource, celestial body, and timeframe.



Figure 1-2: Simplified ISRU value chain (ISECG 2021)

While all these steps need to be considered concurrently for a successful implementation of space resource utilization, the focus of this work solely lays on the thermal removal of water ice from regolith and thus extraction. Other building blocks may be slightly touched on in this thesis yet are not being discussed and evaluated in more detail. The same applies to the extraction of other potential in-situ resources.

Furthermore, this thesis solely focuses on thermal extraction methods. Alternative water production approaches, like the ablative arc mining concept proposed by Greig (2021), the rocket mining concept presented by MASTEN (2021) in cooperation with Honeybee Robotics, or hydrogen reduction of lunar regolith (Sargeant et al. 2021) are shortly mentioned in chapter 2.2.1, yet are not being investigated in more detail. The same applies to specific heating methods for thermal extraction, which are briefly presented in chapter 2.2.2, yet the designs presented in this work are solution independent regarding the heating method.

1.4 Research Methodology and Outline

In order to be able to achieve the goals mentioned in the previous section, a suitable research methodology for this work is to be defined. While several different methodologies for conducting research in a thorough and structured manner exist, the Design Research Methodology (DRM) developed by Blessing and Chakrabarti (2009) offers a sequential and holistic approach. Figure 1-3 shows the main stages of the DRM with its related chapters in this work. In the following, the individual phases of the research methodology are briefly explained in correspondence with the structure of this work.

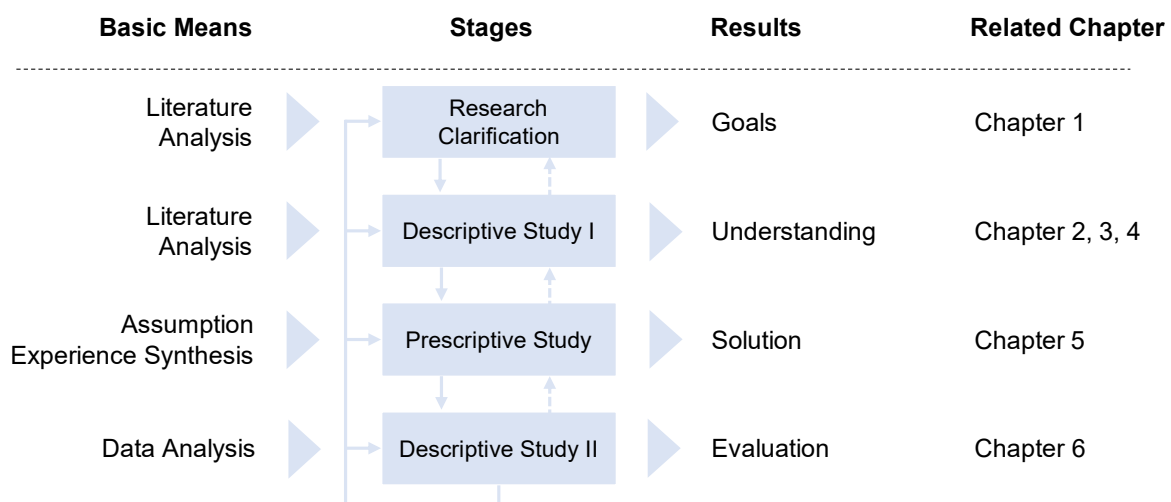


Figure 1-3: Applied research methodology with the related chapters of the work based on Blessing and Chakrabarti (2009: p. 15)

Initially, the **Clarification of the Research Objective** of this work is carried out at the first stage of the DRM. Based on previous research conducted by the Irt at the TUM and the assumption of a further promising research field by the supervisor *Luca Kiewiet*, a basic understanding of the actual situation and the field of action is determined. This is achieved with the additional help of a literature research. Based on that, the objective of this thesis can be derived, which is described in *chapter Introduction 1*.

In the second stage, the **Descriptive Study I**, the required theoretical fundamentals are described to develop a detailed understanding of the topicality, which again is based on a literature analysis. Regarding this work, this stage is referring to the second, third, and fourth chapters. In *chapter 2* the theoretical framework is established, covering both the current state of water on the Moon as well as the State of the Art of existing thermal water extraction approaches apparent in current literature.

The latter covers both experimental works as well as simulation advances. Furthermore, the scientific gap is assessed to outline the relevance of the conducted work. *Chapter 3* further provides context to the objective. For that, a lunar water mining business case is developed, the scenario of water extraction is described, and possible use cases are derived. Finally, high-level system requirements are presented and a framework to perform a multi-criteria analysis covering both qualitative and quantitative factors is introduced. *Chapter 4* covers the mathematical foundation to be able to model and simulate the thermal extraction of lunar water ice, covering both heat and mass transfer mechanisms. This is combined with an extensive literature analysis on thermophysical lunar regolith parameters needed for the modeling and their adequate selection for the scope of this work.

The next step includes the **Prescriptive Study**, which relates to *chapter 5*. Based on the elaborated theoretical foundation laid in the first descriptive study, this step focuses on the development of a concrete solution, which translates into the computational model setup for this work. This includes the implementation of different models of the investigated lunar water extraction methods in the software *COMSOL Multiphysics* and its verification. To be able to properly compare and assess the performance of simulated designs, a parameter study investigating crucial design factors is elaborated and adequate boundaries are set. Also, major simplifications and assumptions made are summarized. In the end, an approach to further optimize the generated results is given.

The **Descriptive Study II**, which is part of the fourth and last step of the DRM, entails the evaluation of the solution developed before, which in the case of this work is related to the analysis and discussion of the generated data in *chapter 6*. First, the performance of each model is described and discussed individually before the methods are compared and assessed by the means of the framework derived in chapter 3. The results also allow a statement to be made about the economic viability of the investigated thermal water extraction methods concerning the presented business case. Also, an additional study is shown further providing supplementary information on the robustness of the models by discussing the uncertainty of other crucial model input parameters and their implications on the results.

Ultimately, the work is summarized and concluded in *chapter 7*, before a brief overview of future lines of work is presented in *chapter 8*.

2 Theoretical Framework

This chapter provides the theoretical fundamentals for this work. First, a short introduction regarding the state of water on the Moon is given in chapter 2.1, before the state of the art in thermal water extraction methods on the Moon is presented in chapter 2.2. This also includes the presentation, assessment, and discussion of existing modeling and simulation approaches and their applicability to this work. In the end, the existing scientific gap in this work is addressed in chapter 2.3.

2.1 State of Water on the Moon

2.1.1 Lunar Water Resource Exploration

As stated in chapter 1.1, water is a critical resource required for long-duration space exploration missions, and in-situ water production is often considered to be key in enabling a sustained human presence on and around the Moon (Kornuta et al. 2019).

The existence of lunar water ice in polar cold traps of the Moon has been postulated for the past 50 years, (Watson et al. 1961; Arnold 1979) and related exploration and research regarding this topic have gone through decades, still being highly relevant today (see Figure 2-1). A combination of the Moon's small inclination of its equator to the ecliptic plane ($\sim 1.5^\circ$) and the large variation in topographic relief near the poles results in large areas that remain in permanent darkness (PSRs) over the 18.6-year precessional cycle of the Moon and thus have a very cold surface temperature of about 35 to 100 K, which are found to be much lower than the ~ 200 K in the surrounding polar regions (McGovern et al. 2013; Mazarico et al. 2011). Generally, the PSRs are located in the impact craters near the lunar poles (Tye et al. 2015).

Due to the extremely tenuous atmosphere of the Moon, which is also called a surface boundary exosphere (NASA 2013), and the thus resulting very low surface pressures of about $3 \cdot 10^{-15}$ bar (Williams 2021), any substance on the lunar surface is directly exposed to a near vacuum. For water ice, this means it will rapidly sublime directly into water vapor and escape into space if subjected to sunlight even for only a short amount of time.

Furthermore, the impact of meteorites left the Moon with volatiles such as water, nitrogen, or methane (McCord et al. 2011). While most of the volatiles decomposed in the sun and escaped into space, water within the PSRs of the lunar polar regions could be permanently preserved, leading to a possible massive accumulation of water ice (Svetsov and Shuvalov 2015).

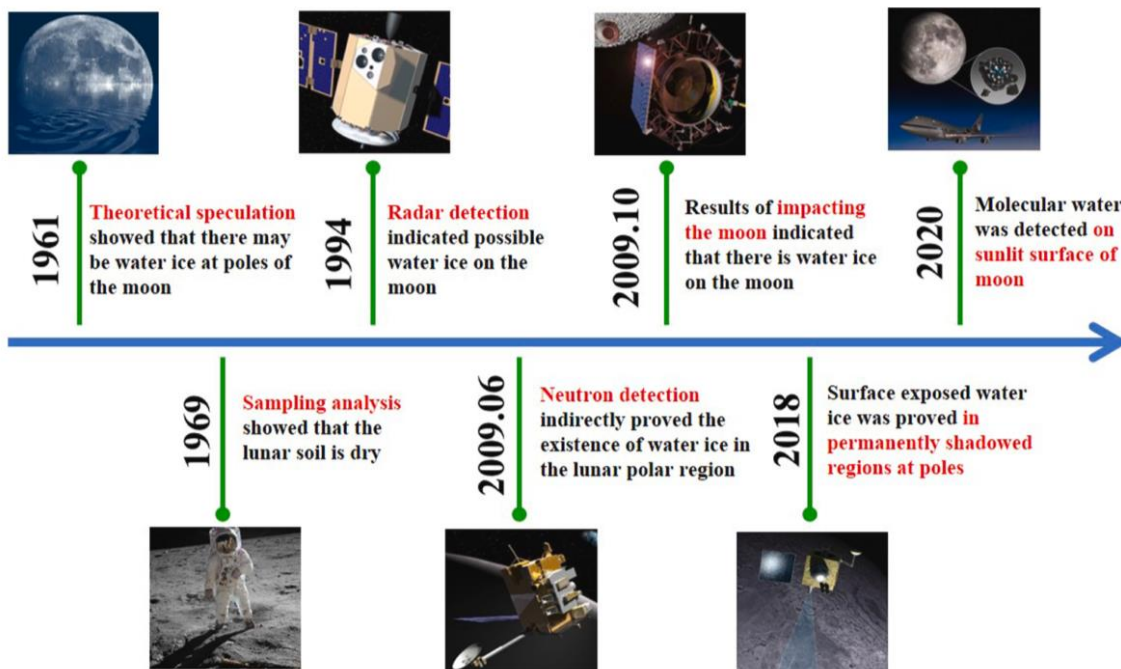


Figure 2-1: History of lunar water resources exploration (Song et al. 2021)

The first real indication of water ice in the lunar poles came from NASA’s Clementine mission (Nozette et al. 1996). Over the years, other researchers have used the data from orbital measurements from equipment aboard Chandrayaan-1, Lunar Reconnaissance Orbiter (LRO), and other spacecraft to detect the quantity, form, and distribution of water ice (Feldman et al. 1998; Elphic et al. 2007; Heldmann et al. 2015).

Sanin et al. (2017) used the Lunar Exploration Neutron Detector (LEND) aboard the LRO spacecraft to detect the presence of hydrogen in the top ~1 m of the lunar regolith. The data collected over the lunar North and South Pole were analyzed to map out the Water Equivalent Hydrogen (WEH) on the lunar poles (Figure 2-2). As the figure shows, the PSRs on the poles were estimated to contain 0%- 0.5% WEH by weight.

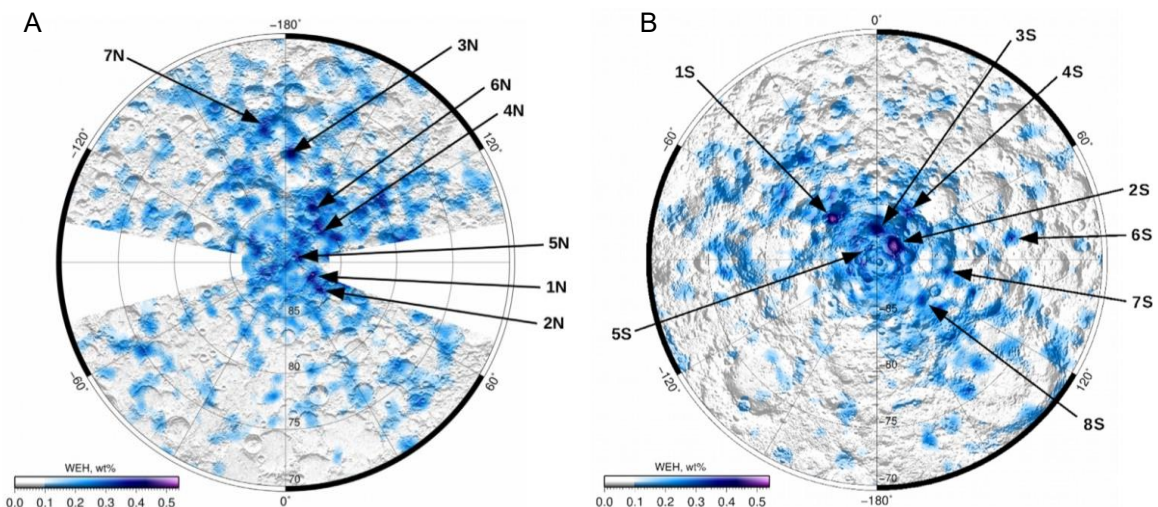


Figure 2-2: Map of Water Equivalent Hydrogen (WEH) abundance in the (A) lunar north- and (B) south

pole (adapted from (Sanin et al. 2017))

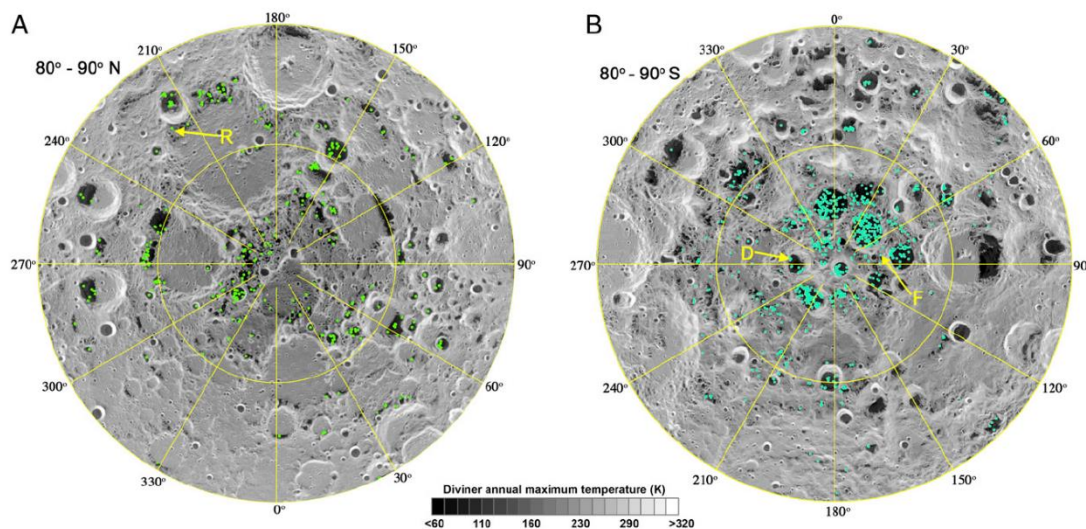


Figure 2-3: Distribution of water-ice-bearing pixels (green and cyan dots) overlain on the Diviner annual maximum temperature for (A) northern- and (B) southern polar regions (Li et al. (2018))

On the other hand, Li et al. (2018) analyzed the reflection spectrum data obtained by the Moon Mineralogy Mapper (M3) of Chandrayaan-1 and identified the near-infrared absorption spectrum characteristics of water ice, thus obtaining direct evidence about the existence of water ice on the surfaces of PSRs in the lunar poles (Figure 2-3). The authors concluded that in the polar regions surface-exposed ice with up to ~30 wt.% water ice content existed, underlining the potential for water ice mining within the PSRs of the Moon.

Together with in-situ measurements conducted from the Chinese Spacecraft (S/C) Chang'E5 (Lin et al. 2022), the only direct evidence of the presence of water ice on the moon so far was acquired during the LCROSS S/C launched with the LRO. After the impact of the Centaur upper stage on the lunar surface in the Cabeus crater on the lunar south pole, detection results showed that the water ice content in the lunar soil was 5.6 ± 2.9 wt.% (Gladstone et al. 2010; Colaprete et al. 2010). A summary of the total water vapor, ice, and ejecta dust can be seen in Table 2-1.

Table 2-1: Summary of the total water vapor, ice, and ejecta dust in the near-infrared instrument field of view of the LACROSS mission (Colaprete et al. 2010)

Time (s)	Water mass (kg)			Water wt. %
	Vapor	Ice	Dust mass (kg)	
0–23	82.4 ± 25	58.5 ± 8.2	3148 ± 787	4.5 ± 1.4
23–30	24.5 ± 8.1	131 ± 8.3	2434 ± 609	6.4 ± 1.7
123–180	52.5 ± 2.6	15.8 ± 2.2	942.5 ± 236	7.2 ± 1.9
Average	53 ± 15	68 ± 10	2175 ± 544	5.6 ± 2.9

Furthermore, water molecules have also been recently found outside the PSRs. According to Honniball et al. (2021), the latter was identified with the help of the NASA/DLR Stratospheric Observatory for Infrared Astronomy (SOFIA) on lunar sunlit regions via its spectral signature at 6 μm (Pieters et al. 2009; Clark 2009). Before that, widespread hydration was inferred to be present on the lunar surface though observations of a characteristic absorption feature at 3 μm , yet the hydration could not be distinguished between molecular water or other hydroxyl compounds using the 3 μm band (McIntosh et al. 2017). In another study regarding the distribution, abundance, and origins of water on the surface of the Moon, Li and Milliken (2017) estimated lunar regolith outside of PSRs to have a water ice mass content of 0,1–1 wt.%.

Even more, Hayne et al. (2021) proposed that big amounts of water ice, in addition to the large PSRs, can also occur in many unmapped micro cold traps on small spatial scales from 1 km to 1 cm. The authors conclude that approximately 10-20 % of the permanent cold trap area for water ice is found to be contained in said micro cold traps. It may be assumed, that the regolith is containing similar water ice mass content like the PSRs of ~5 wt.%.

2.1.2 Form and Distribution of Water Ice

The preceding studies suggest that there exist water ice resources on the Moon, particularly in the polar regions, and a significant reserve of water ice could be expected within the PSRs. Yet, it is currently still largely unknown, in which form the water ice occurs both on the lunar surface and subsurface and how it is distributed both lateral as well as vertically.

Researchers discovered that there could be multiple types of lunar water using various detection methods. Some water is assumed to be pure blocky ice in the PSRs at the poles (Calla et al. 2016; Spudis et al. 2013), whereas it can also occur as an ice-lunar regolith mixture (Mitrofanov et al. 2010). Using secondary ion mass spectrometry to examine Apollo samples obtained in the 1960s and 1970s, some researchers discovered that there was some water ice present in the form of hydrated minerals and that it was distributed across the whole lunar surface (Basilevsky et al. 2012). In a work, which is still in preparation, Cannon (2020) also investigates the potential physical textures of ice and regolith in lunar cold trap environments, as seen in Figure 2-4. To know the occurrence and physical state of water ice is important to determine the optimal way to both extract and sample it.

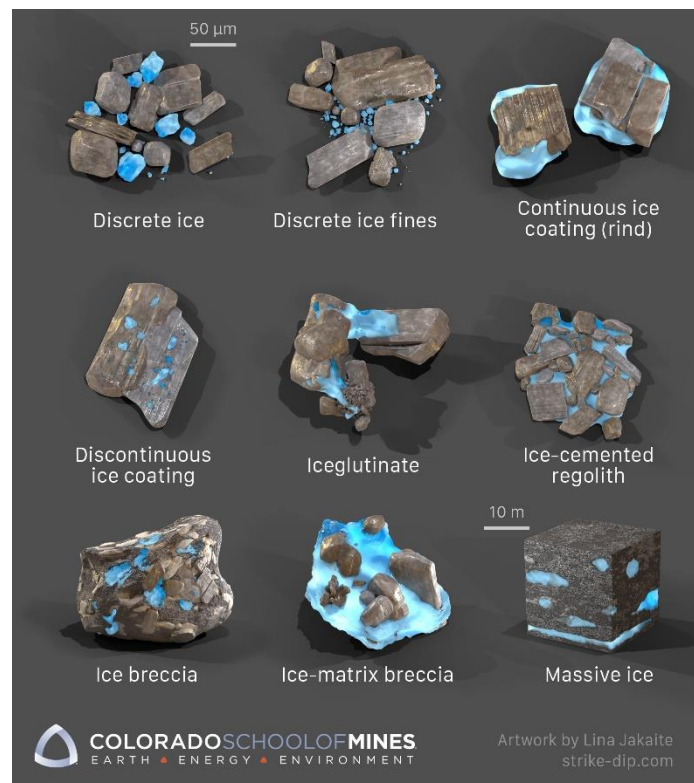


Figure 2-4: Potential physical textures of ice and regolith in lunar cold trap environments (Cannon 2020)

Regarding the vertical distribution of water ice, Gladstone et al. (2010) first suggested that there may be a potentially desiccated layer of regolith of several tens of cm. This claim is also backed by eg. Reiss et al. (2021), who investigated the dynamics of the subsurface migration of water on the moon. The authors conclude that, while some water bound to the lunar soil is being released by the daily temperature cycles on the Moon and lost to space, a portion of it is transported to deeper layers in the regolith, which is mainly driven by temperature gradients and being called water pumping mechanism (Reiss et al. 2021). Cannon and Britt (2020) on the other hand mainly consider impact gardening as a modifying process that drives changes in the water ice distribution by building stochastic impact simulations. The authors concluded, that ice water ice concentrations should eventually become fairly homogeneous and are distributed randomly rather than being clustered like in Earth-like ore bodies (see (Cannon and Britt 2020)).

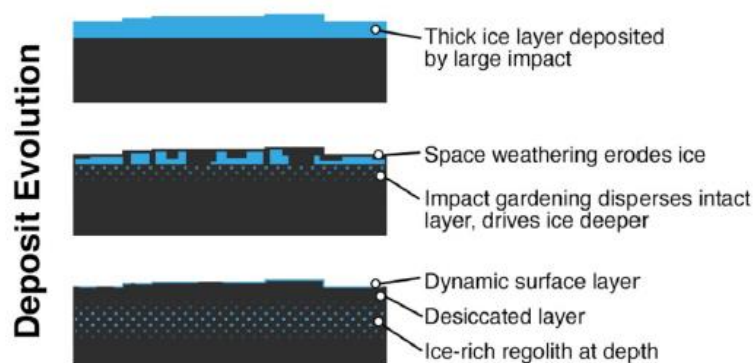


Figure 2-5: Schematic cross-section showing the evolution of polar water ice deposits (Cannon and

Britt 2020)

Considering the different possibilities in water ice occurrence on the surface of the moon, Cannon and Britt (2020) have also focused on identifying extraction locations and developing an “ice favorability index” to predict the water ice distribution on the Moon. Yet, as the various works described previously show, the form, distribution, composition, and quantity of water ice on the Moon remain largely uncertain. This uncertainty has created a great hindrance in establishing a business case for the lunar water ice extraction (see chapter 3.1).

2.1.3 Future Exploration Missions

The only way to reduce this uncertainty is by obtaining more ground-truth data by drilling exploratory boreholes in and outside the craters. While the interest in space resources and exploration technologies, often with a focus on the moon, has highly increased, several prospecting missions have been planned.

Among others, as part of the Artemis program, NASA recently announced sending The Regolith and Ice Drill for Exploring New Terrain (TRIDENT) first in the Polar Resources Ice Mining Experiment-1 (PRIME-1) likely to be launched in 2023 and as well onboard the Volatile Investigating Polar Exploration Rover (VIPER) in late 2024 to the lunar South Pole to drill up to 1m deep, excavate and analyze the in-situ water ice on the Moon (Loff 2019). During its 100-day mission, VIPER is going to be the first-ever resource mapping mission on another celestial body, collecting data on where the Moon’s ice is most likely to be found and easiest to access. For that, the rover will also go into the PSRs, determining the distribution, physical state, and composition of the water ice deposit, also providing inside into the origin of water and other volatiles across the solar system (NASA 2022b).

Also, the European Space Agency (ESA) presented the Package for Resource Observation and in-Situ Prospecting for Exploration, Commercial exploitation, and Transportation (PROSPECT) (ESA 2019), originally planned to fly aboard the Russian lunar lander Luna 27 in 2025 but is now flying with an US lunar lander later this decade. PROSPECT is set to additionally targets the characterization of water isotopes to obtain information on the resource’s origins and emplacement process.

The China National Space Administration (CNAS) with their mission Chang’E6, the Chandrayaan-3 mission from the Indian Space Research Organization (ISRO), and the Japan Aerospace Exploration Agency (JAXA) with the Lunar Polar Exploration (LUPLEX) have announced similar drilling campaigns to be launched within the next five years.

2.2 State of the Art

In this subchapter, the state of the art about existing thermal water extraction methods on the Moon are presented and analyzed. Water collection on the Moon, especially in the PSRs, poses engineering challenges due to the very harsh environment, requiring extraction scenarios that are unique to the lunar surface.

To extract the water via a thermal method, multiple steps are needed. First, the regolith needs to be heated until volatiles are outgassing from the sample. In the context of water ice, this can be applied to either loosely absorbed water molecules, ice particles,

or also water trapped inside minerals, with various degrees of heat needed for each. (see chapter 2.1) Then, the newly formed water vapor has to be contained in a protected environment or a reaction chamber and lastly captured either by the means of depositing it in a cold trap or via other methods.

2.2.1 Existing Thermal Water Extraction Approaches

There are several different approaches to realizing an extraction of lunar water ice from the regolith. Table 2-2 provides an overview of the methods and technologies required in a lunar mission for this purpose. For the applied context, specific methods may be more advantageous than others, which will be qualitatively discussed in the following.

Among others, Kornuta et al. (2019) distinguish between two major differences when it comes to the thermal extraction of water from lunar regolith. On the one hand, there are *In-Situ methods* (Duke et al. 1998; Sowers and Dreyer 2019; Brisset et al. 2020; Schieber et al. 2022), leaving the regolith mostly in its original state and extracting water directly from the regolith on the lunar surface, and on the other hand *excavation methods* (Mueller et al. 2013; Zacny et al. 2012; Just et al. 2020; He et al. 2021), where the regolith is firstly mined before being heated afterward.

In-Situ extraction methods again can be divided, mainly by the form of heating. While one concept uses a heated dome or tent for heating the regolith only above the surface, another method additionally uses drills or metal rods with integrated heaters inserted under the regolith under the dome. This is done to access and heat a larger volume of regolith at greater depths and should consequently allow for more water to be extracted faster, at the cost of increased complexity to the design. In both cases, the dome can either be heated by sunlight or any other electrical source. The heat sublimates ice into water vapor escaping from the surface. The latter is then captured by the dome, which is sealing the heated surface from the outside environment to minimize losses before it is vented through openings into cold traps outside the dome where it refreezes. Once the cold traps are full of frozen vapor, they can simply be replaced and transported to a central processing unit for further treatment. (Sowers and Dreyer 2019) A conceptual illustration of the in-situ thermal mining concept can be seen in Figure 2-6.

According to Sowers and Dreyer (2019), critical functional steps for In-Situ thermal mining are:

1. Sublimation of ice and transport of water vapor through the subsurface.
2. Confinement and transport of the vapor to cold traps.
3. Passive cooling of the cold traps.
4. Power delivery for surface and (optional) subsurface heating.

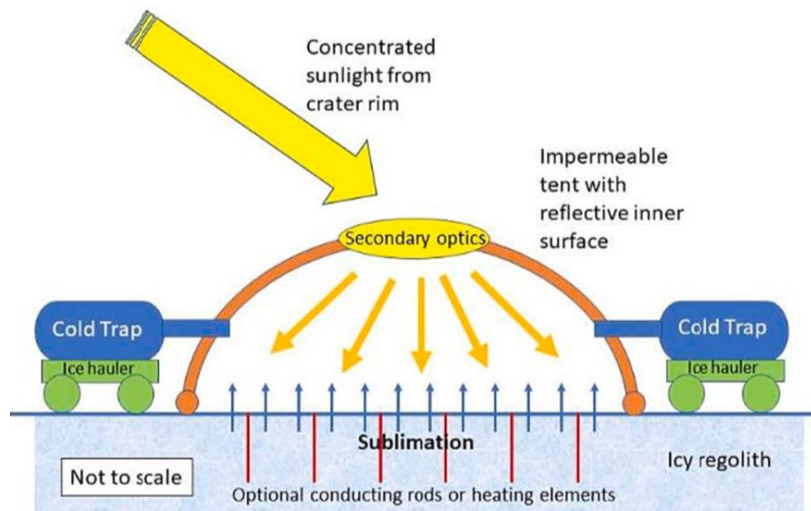


Figure 2-6: In-situ thermal mining concept (Sowers and Dreyer 2019; Kornuta et al. 2019)

Alike to *In-Situ methods*, *Excavation methods* can be further distinguished, since regolith can either be mined per batch or also continuously (Just et al. 2020). The former, which is also called discrete excavation, requires the icy regolith to be fed in a crucible or reaction chamber before being heated. It is characterized by the need to break contact with the soil in between cuts to clear the cutting surface or to dump the excavated material (single large bite). Examples are front loaders, dozers, or backhoes (Skonieczny et al. 2016).

Continuous excavators on the other hand are systems, where multiple cutting surfaces are continually in contact with the soil and multiple cuts are possible. Once one cutting surface or bucket has gathered enough soil, it then clears the contact area while the next cutting surface has already started accumulating soil (multiple small bites). Examples include bucket wheels or augers. (Just et al. 2020) A possible excavation and heating method combination is seen in Figure 2-7.

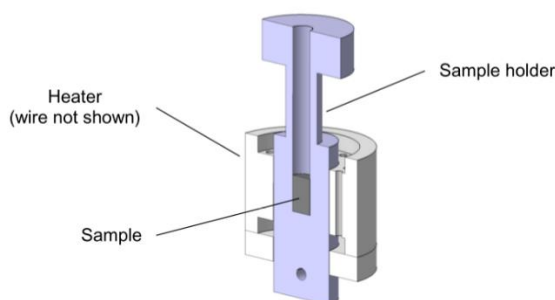


Figure 2-7: Possible combination for crucible heating with a heating chamber setup (left) (Reiss 2018b) and a bucket drum excavator to deliver the regolith (right) (modified from Just et al. (2020))

When looking at the current literature regarding excavation methods, especially *continuous excavators* in the form of different drills and augers are in the focus of scholars (Zacny et al. 2012; Vendiola et al. 2018; Pelech et al. 2019; Kornuta et al. 2019; He et al. 2021), with two major different principles standing out. Both apply heat to water-bearing regolith and flow extracted water vapor to a low-temperature

condenser (cold-trap) for deposition. The primary distinction between the approaches is one uses a coring auger to drill and heat the regolith within the borehole (Figure 2-8) while the other utilizes a deep-fluted closed auger to bring cuttings to the surface for heating within a closed, sealed vessel. In these and similar concepts, the total energy required for extraction is driven by the latent heat of sublimation for water rather than sensible heat exchange with the hardware or regolith, overcoming heat loss or other inefficiencies, or drilling energy (Kornuta et al. 2019). An extensive overview of the several excavation methods, yet not necessarily linked to thermal water extraction, can be found in Just et al. (2020).

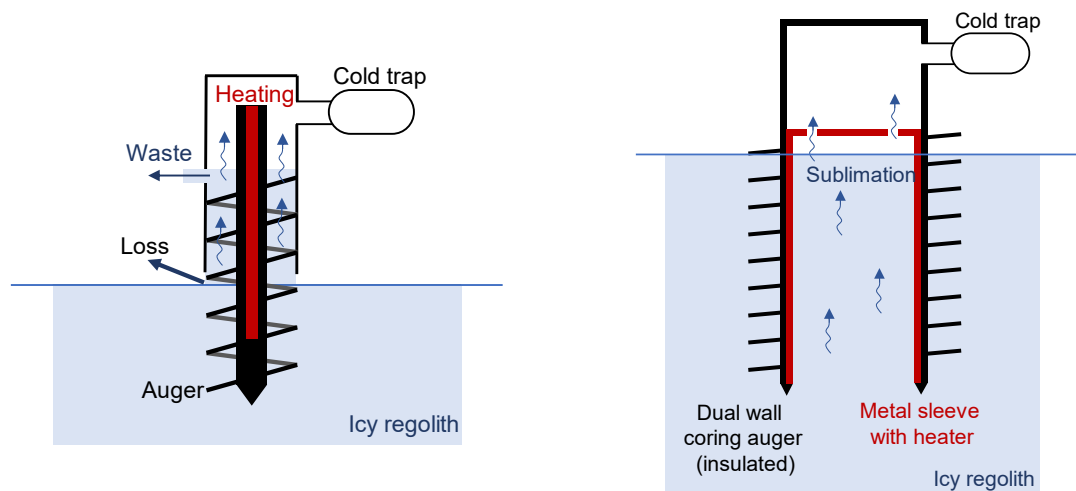


Figure 2-8: Consecutive water extraction systems with heating inside the borehole: heated deep-fluted auger (left) (based on He et al. (2021) and heated dual wall coring auger (right) (based on Zacny et al. (2016)

Compared to *In-Situ methods*, *Excavation methods* require the transport and handling of large volumes of regolith, which drives up the mass and power requirements. According to Just et al. (2020), this leads to two significant issues: (1) the geotechnical properties of the lunar regolith (including chemical composition mineralogical makeup, possible ice, or other volatile content) (Colwell et al. 2007) and (2) the gravity conditions on the Moon (1/6 of Earth's gravity). This is even emphasized by Gertsch (2006) and Pitcher et al. (2016), who stated that especially the amount of water ice within prepared samples of lunar regolith strongly affects the excavatability of the material. The authors came to the result, that the higher the wt.% of water ice in the regolith, the more difficult it is to excavate it.

Yet, on the other side *Excavation methods* are capable of extracting water at a range of depths and locations in various forms. Also, tight control over the volatile temperature and flow is possible and due to the naturally low thermal conductivity of the lunar regolith, heat transfer within the soil can be facilitated. (Zacny et al. 2012; Kornuta et al. 2019)

Table 2-2: Summary of viable thermal water extraction methods on the Moon

Principle	Extraction method		Source
In-Situ	Heating through surface	Heated dome/tent with heated drills	(Sowers and Dreyer 2019; Brisset et al. 2020; Song et al. 2021)
	Heating above the surface	Heated dome/tent	(Sowers and Dreyer 2019; Brisset et al. 2020; Wasilewski 2021b; Schieber et al. 2022)
Excavation	Discrete heating	Icy regolith fed in a sealed crucible and heated	(Reiss 2018b)
	Continuous heating	Icy regolith fed in e.g. auger and heated within the borehole	(Vendiola et al. 2018; He et al. 2021)
	Discrete heating	E.g. closed auger to bring cutting to the surface for heating within a sealed vessel	(Zacny et al. 2012; Zacny et al. 2016)

Alternative water extraction designs

Alternative water ice extraction concepts are e.g. the ablative arc mining concept proposed by Greig (2021) or also the rocket mining concept presented by MASTEN (2021) in cooperation with Honeybee Robotics. The former relies on an electric arc to ablate and ionize surface material, which then can be sorted by mass into material groups and transported to a relevant collector by electromagnetic fields. By using a magnetic field to separate volatiles, this technique can readily apply to any regolith constituent, including water and metal ions, in a single system architecture. This brings multiple advantages compared to typical thermal mining concepts, yet the proposal is still low in technological readiness. (Greig 2021)

The rocket mining concept on the other hand utilizes a rocket engine under a pressurized dome to enable a comparably deep cratering below the lunar surface. During this process, ejecta from multiple rocket firings blasts up into the dome and gets funneled through a vacuum-like system that separates ice particles from the remaining dust and transports it into storage containers. The small, low-mass system, including the rocket fuel, engine, collapsible dome, and storage containers, can be attached to a rover and delivered to the Moon on lunar landers. (MASTEN 2021)

Furthermore, another interesting approach developed by Metzger (2020) called *Aqua Factorem* simplifies the system architecture to extract lunar water to the minimum, by assuming the water ice to be present as ice grains since micrometeoroid bombardment has had already broken down most of the solid material in the upper lunar surface. Additionally, due to the very low temperatures in the PSRs, the ice grains are hard as granite. Yet, while still being mixed with all the other materials, a simple, ultra-low-energy grain-sorting process can extract the ice without phase change (Metzger 2020). All of the above-described alternative water extraction methods were proposed at NASA's "Break the Ice Lunar Challenge" (NASA 2022a; Vetcha et al. 2022).

2.2.2 Heating Methods for Thermal Water Extraction

For the actual extraction of lunar volatiles like water ice, the heating method of choice often is electrical heating. While the focus of this work is not to assess the different heating options, only a short overview of the latter is given. While electrical heating, be it via conduction or radiation, can be applied to any sample, other methods such as microwave heating, laser heating, or solar heating have been addressed in the past, but for scientific instruments in the scope of planetary exploration, having found only limited applications.

Microwave heating generally is a much faster and more energy-efficient process (Taylor and Meek 2005), but it is more challenging to achieve a controlled heating of the regolith. There are also controversial opinions regarding what causes the regolith to couple with microwave radiation: ilmenite content, nanophase iron (Taylor and Meek 2005), and particle shape (Barmatz et al. 2013) are possible explanations. Because of the difficulties in controlling the heat, microwave heating is more applicable where only high temperatures need to be achieved in one single step, for instance for 3D printing, which includes sintering and melting of the regolith (Pereira et al. 2020). Nevertheless, research is still being conducted looking into the potential of microwave heating for lunar volatile extraction (Kulkarni and Abhang 2021).

Another method is solar heating, with the advantage that no power supply is required. Additionally, an increased system complexity might have to be considered, because solar light needs to be focused with lenses or mirrors, which are difficult to maintain dust-free in the lunar environment (Sowers and Dreyer 2019).

Laser heating also only applies to the top surface of a sample and hence requires mixing if a bulk sample shall be heated. Gustafson et al. (2010) have applied laser heating as a precursor for solar heating on regolith for the demonstration of the ISRU process of carbothermal reduction. Other heating possibilities like eg. convection using steam or a different gas, or also recuperative heat were not investigated.

2.2.3 Existing Simulation Approaches

In recent years, several studies investigating the thermal properties of icy planetary materials concerning heat and mass transfer have been published. Since such analyses highlight difficulties and knowledge gaps in exploration and extraction, this is especially intriguing for upcoming thermal mining operations, yet the work conducted on this topic is still very limited.

Thermal models describing the basic thermophysical properties of lunar soil are around since Apollo brought back the first regolith samples. Amongst others, especially Schreiner et al. (2016) and Hayne et al. (2017) provide adequate overviews of the topicality. Reiss (2018a) and Biswas et al. (2020) both developed a model to predict volatile evolution in the context of sampling lunar rovers. Especially Reiss (2018a) provided a sophisticated thermal conductivity model, including interdependencies of gas and solid conductivity, and displayed a comprehensive mass transfer model including sorption processes. Closely related to this model is also Smolka (2021). Similar studies have been conducted by Hudson et al. (2009) and Siegler et al. (2012) for martian regolith. Yet, at cryogenic temperatures ($< \sim 80$ K) and especially at PSR temperatures, which can get as cold as 20-40 K (Martinez and Siegler 2021), conventional assumptions on thermophysical properties of regolith for the description

of thermal transport break down and additionally, the heat transport process through the mixture of crystalline and amorphous components is not well understood (Biele et al. 2022). Among others, this was addressed by Woods-Robinson et al. (2019), who estimated the thermal conductivity for either crystalline or amorphous endmember lunar materials valid for temperatures down to ~ 15 K.

Based on that, some scholars have started working on different modeling approaches for the thermal extraction of water ice. Early simulation studies covering mainly the heat transfer process in icy deposits are presented by e.g. Fanale et al. (1990), Gori and Corasaniti (2004), or Hecht (2006). More recent studies are e.g. from Metzger et al. (2020), who examined the evolution of water ice in the context of sampling lunar rovers applying an extraction concept similar to the “corer”, which is a double-walled heated auger first presented by Zacny et al. (2016). The heat transfer model presented by the authors follows a novel approach and is based on the Crank-Nicholson algorithm. Brisset et al. (2020) investigated an in-situ extraction method supplemented by heated rods to facilitate the conduction with a coupled heat and mass transfer and simplified water vapor model. Yet, the authors only made some course approximations for some major thermophysical properties of the lunar regolith. For the corresponding literature, especially the applied value for the thermal conductivity of lunar soil is unrealistically high, which is expected to fundamentally alter the compiled results of the study. The same extraction method was modeled by Song et al. (2021), who also included the collection of water vapor after the withdrawal. Still, the combined heat and mass transfer model is greatly simplified. Another concept for in-situ thermal extraction was examined by Schieber et al. (2022), which differs from previous works as the secondary optics were eliminated and replaced with a highly absorptive ceramic that transfers heat to the icy regolith. Concerning the mathematical approach in calculating the coupled heat and mass transfer mechanisms, this model is comparable to Reiss (2018a) and extended for icy regolith.

However, none of the described models cover the migration of the phase change interface, or sublimation front, sufficiently, resulting in a significant knowledge gap. This problem is first tackled by Wasilewski (2021b), who focused on the behavior of said interface, namely its location, velocity, and acceleration in various scenarios, in a PSR environment during surface thermal mining. Table 2-3 provides an overview of the existing simulation approaches to the goals of this work. Further information on the evaluated criteria can be found in chapter 4.

Table 2-3: Overview of existing simulation approaches concerning the goals of this work.

	(Wasilewski 2021b)	(Reiss 2018a)	(Smolka 2021)	(Sesko 2021)	(Schieber et al. 2022)	(Brisset et al. 2020)	(Song et al. 2021)	(Metzger 2018)	(Metzger et al. 2020)	(Woods-Robinson et al. 2019)	(Hayne et al. 2017)	(Schreiner et al. 2016)
Accuracy of thermophysical soil properties												
Inclusion icy regolith	Yes	Yes	No	No	Yes	Yes	Yes	Yes	Yes	No	No	No
Heat transfer modeling	Yes	Yes	Yes	Yes	Yes	Yes	Yes	Yes	Yes	Yes	Yes	No
Mass transfer modeling	Partly	Yes	Yes	No	Yes	Yes	Partly	No	Yes	No	No	No
Phase change modeling	Yes	No	Partly	No	Yes	Yes	Yes	No	Yes	No	No	No
Sublimation front display	Yes	No	No	No	No	No	No	No	No	No	No	No
Applicability to this work												
												

2.3 Scientific Gap

ISRU is believed to be the decisive factor in making long-term and sustainable space exploration feasible. Especially water is an essential resource, which is not only needed for life support applications but is also a source for S/C propellant (see chapter 1.1). The theoretical framework presented in the last chapter, which examined the state of water on the Moon as well as the State of the Art in thermal water ice extraction designs and methods, revealed several knowledge gaps in literature in consideration of the goals of this work, which are being summarized in the following.

Regarding the state of water on the moon, there is an obvious lack of ground truth data specifying both the lateral and vertical distribution (discrete or continuous), the quantity (concentration), and quality (pure water ice or contaminated), and thus resulting the technical recoverability of the water ice residing beneath the lunar surface. Furthermore, it is not known how the water ice is specifically mixed with the lunar regolith on a molecular basis, which has a huge impact on the thermophysical

properties of the mixture, making it hard to investigate thermal extractability with reasonable fidelity. (see chapter 2.1.1)

Yet, scholars have presented several experimentally and simulation-backed designs for thermal water extraction, which can mainly be distinguished between In-Situ and excavated methods. The missing ground-truth data is also the major limitation in modeling the thermophysical properties of the lunar regolith. Thus, existing simulation approaches often use strongly simplified values as well as make different assumptions regarding those values, making it hard to validate and compare the simulations. Especially for cryogenic temperatures, which are apparent in the PSRs and where a huge amount of lunar water ice is expected, conventional assumptions, which are often based on the returned Apollo samples are not valid. Furthermore, investigating and assessing existing simulation approaches of thermal water extraction showed, that there is no common ground in calculating the dynamically changing material properties during the phase change due to the desired sublimation of ice into vapor as well as mass transfer mechanisms of the generated water vapor through the regolith, consisting of both advection/convection and diffusion. (see chapter 2.2.3)

To be able to make a more precise statement about the state of lunar water ice and its implications on the thermophysical properties of the regolith, more ground-truth data is needed, with VIPER being the next prospecting mission in line on its way to the Moon in late 2024 (NASA 2022b). Independent from the data that is thought to be gained through those missions, the literature research made it clear that there is also a major gap comparing and assessing different thermal extraction methods with each other to determine the best method for certain scenarios regarding e.g. their total water yield or also their energy efficiency. Furthermore, in addition to a quantitative evaluation, factors like complexity, reliability, development costs, design lifetime, or also the water ice accessibility of different methods can be assessed as well (see chapter 3.3).

3 Mission Context

After presenting the theoretical framework according to the state of water on the Moon and possible thermal lunar water extraction designs and simulation approaches found in recent literature, this chapter presents the scenario chosen for this thesis in section 3.2. Yet first, a quick introduction to potential business cases and cost estimates for lunar water mining is given. This provides a reference on the required total water yield per year to make lunar thermal mining economically viable. Thus, the results of the simulations conducted in this work can be compared and optimized according to an overall business objective. From both the initial business cases and the scenario chosen, a top-level requirement list can be derived. Furthermore, since multiple water extraction designs are investigated, a feasible comparison method is presented.

3.1 Lunar Water Mining Business Case

So far, the driving motive of space exploration has been mainly for geopolitics, for simply prestige via successful space activities, or nations striving for military advantage. Only a few sectors like the communications satellite industry have been motivated by economic reasons, yet its proportion is rather small. This is simply due to the reason that it is difficult to be profitable as a purely commercial space venture, which is not government-funded. Two main challenges arise: On one hand, a revenue stream comes from customers who are willing to pay for a product. Said customers ultimately reside on earth, which leaves a space-related company facing the problem of how to deliver value to its customers. On the other hand, space activities, in general, are connected to exorbitant costs due to very hostile environments, vast distances between places of interest as well as the deep gravity well on earth. (Sowers 2021)

Yet, the key to persistent and sustainable development in space is being economically profitable. While the idea of using space resources has been postulated for many years, which lots of start-ups focusing especially on asteroid mining to pursue them for precious metals, its technical progress is still very limited. The scientific discovery of water near the Moon's poles has pushed the trend towards water as the first commercially viable application of space resources, representing a more plausible path to viability. (Kornuta et al. 2019) For instance, the Luxembourg Space Agency (LSA) commissioned a study that predicted potential earnings from space resources of 73–170 B € starting with lunar water in the years 2018–2045 (LSA 2018).

For the idea of “living off the land” to be commercially sustainable, the cost of producing the resources locally must be affordable and eventually less expensive than the cost of obtaining them from Earth. The two major cost elements specifically contributing to the operation of a lunar ISRU-type facility are the initial transportation cost, i.e. the cost of bringing the equipment to the lunar surface as well as the costs related to sustaining the operation of the equipment on the Moon. Since the cost of any infrastructure on the Moon is mainly determined by the transportation cost, which is currently in the order of 1 M\$/kg, even reducing this figure in the future by technical advances, transportation costs will continue to be the dominating cost element. (Seidel et al. 2021)

Several scholars have investigated potential business cases and cost analyses for in-situ propellant production on the Moon (Charania and DePasquale 2007; Jones et al. 2019; Kornuta et al. 2019; Bennett et al. 2020; Sowers 2021), yet with respective very different conclusions. For the evaluation, indirect revenue streams by establishing

permanent settlements and advanced infrastructure on the Moon have been neglected, and only propellant production through electrolysis is considered for the respective case. This results in an in-situ water extraction requirement of approximately 1.5 tons for producing 1 ton LO₂/LH₂ propellant, by taking into account the oxidization happens with a mass ratio of approximately 5.35-1 and water comes in the ratio of 8-1 (Kornuta et al. 2019).

As already mentioned, both the gravity well of Earth as well as vast distances are the main drivers for the transportation cost of space activities, which is underlined by the famous rocket equation. To put it simple, the further you want to travel in space without being able to refuel your S/C, the more propellant you must take with you, also further increasing your fuel consumption due to the higher mass. Thus, in-situ propellant production could drastically cut the costs required for space activities in cislunar space. (Sowers 2016)

Regarding certain customer scenarios, Kornuta et al. (2019) distinguish between a possible customer on the lunar surface (eg. supporting mid- to long-term lunar bases), at the first Earth-Moon Lagrange point (EML1) (eg. gateway to operate a Mars base) or in further cislunar space in Low Earth Orbit (LEO) to Geostationary Orbit (GEO) range.

Initial lunar surface customers will likely be a reusable crew or cargo shuttle cycling between the surface and the lunar gateway, as it is planned with the Artemis program by NASA (Smith et al. 2020). According to Kornuta et al. (2019), on an abstract level, assuming two crewed flights requiring 25 MT of propellant each, and an additional cargo flight expecting to burn about 50 MT of propellant, the resulting demand would amount to 100 MT per year, which would require to extract about 150 MT of water.

A customer scenario for EML1 could be that the lunar gateway is used as a staging area for a Mars mission, which could demand a total propellant demand of 140 MT/year at EML1 translating to a total amount of 280 MT/year propellant at the lunar surface and thus 420 MT/year water to be mined (Cichan et al. 2017).

Refueling operations of upper-stage vehicles in LEO would empower the S/C to a super heavy lift to GEO and even further. While there could be demand for up to three of those maneuvers per year, each requiring up to 70 MT of propellant, the total amount that would be needed in LEO amounts to 210 MT/year. Accounting for the transportation from the lunar surface to LEO, the demand increases to 1260 MT/year on the lunar surface, again translating to an approximated requirement of 1880 MT/year of water to be mined. (Kornuta et al. 2019) Serving all the presented initial customer scenarios simultaneously, a total amount of 450 MT/year propellant is required at various locations (lunar surface, EML1, and LEO), translating to a total amount of 1.640 MT/year propellant that must be produced on the Moon, which equates to 2.450 MT/year of lunar water that must be extracted. A summary of the respective propellant requirements for the different customer scenarios is provided in Table 3-1.

Table 3-1: Propellant and water demand for initial lunar propellant customer scenarios

Customer Scenario	Propellant demand @ customer location	Propellant demand @ lunar surface	Water demand @ lunar surface
NASA Lunar Crew	100 MT/year @ lunar surface	100 MT/year	150 MT/year
Mars Base Camp	140 MT/year @ EML1	280 MT/year	420 MT/year
LEO to GEO Upper Stage Refueling	210 MT/year @ LEO	1.260 MT/year	1.880 MT/year
SUM	450 MT/year	1.640 MT/year	2.450 MT/year

On the question of whether lunar in-situ propellant production is economically reasonable, there is still no common ground in literature. Recent and widely accepted work conducted by Kornuta et al. (2019) and Sowers and Dreyer (2019; 2021) are indicating that once established, the lunar-sourced propellant will dramatically reduce the cost of all beyond LEO space activities and potentially enable other profitable commercial ventures to emerge, with the cost for in-situ produced fuel on the lunar surface being a factor of 70 times cheaper than transporting it from Earth. A comparison of propellant costs from Earth as well as from the Moon is provided in both Table 3-2 as well as Figure 3-1.

On the other hand, according to Charania and DePasquale (2007) the propellant price on the lunar surface, which is locally produced is calculated to be as high as 35.300 \$/kg, providing no noteworthy reduction of the cost compared to propellant from Earth. Another recent study conducted by Jones et al. (2019) even stated a value of 101.000 \$/kg for lunar-produced fuel in cislunar space at EML1, being 100 times higher than the price stated by Kornuta et al. (2019) lunar produced fuel and still over 8 times higher even than propellant from Earth.

The reason for the huge differences in cost calculations lay among others in different mission architecture approaches and assumptions and even business models. While eg. Sowers (2021) used a thermal mining architecture that is intended to be minimal economically viable, was not accounting for the development costs of its space transportation system, and assumed a PPP model that leverages both public and private sources of capital, the study by Charania and DePasquale (2007) assumed a completely private venture, including development costs for transportation as well as relying on excavation for the water extraction. The study by Jones et al. (2019) on the other hand was specifically conducted to determine the cost-effectiveness of lunar propellant for a Mars mission, from the perspective of a complete government-run Mars program. With the rise of “New Space” and the ongoing commercialization of Space Systems, the development, and introduction of new transportation systems (e.g. Starship) are yet considered to further reduce the costs from Earth.

Table 3-2: Propellant cost estimates from both Earth and the Moon (Kornuta et al. 2019)

	From Earth	From Moon
Earth Surface	\$ 1/kg	-
LEO	\$ 4.000/kg	\$ 3.000/kg
GTO	\$ 8.000/kg	\$ 1.500/kg
GEO	\$ 16.000/kg	\$ 1.500/kg
EML1	\$ 12.000/kg	\$ 1.000/kg
Lunar Surface	\$ 36.000/kg	\$ 500/kg

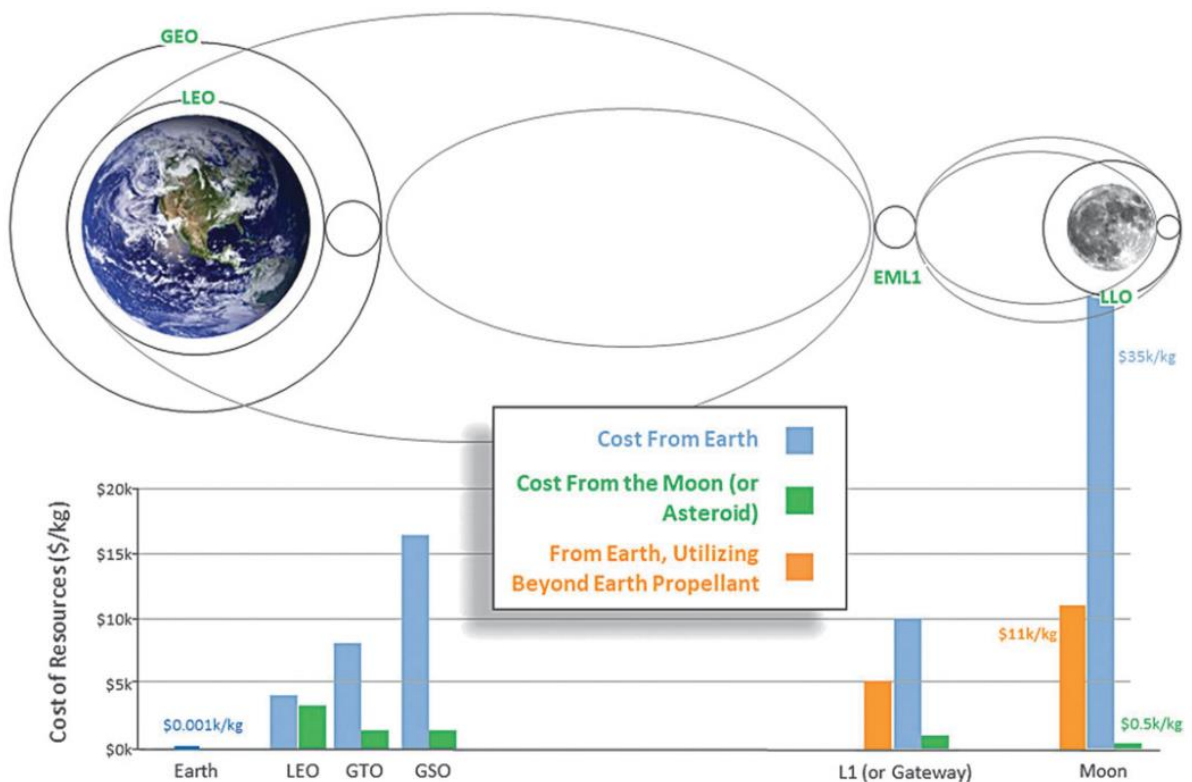


Figure 3-1: Propellant prices in Cislunar Space (Kornuta et al. 2019; Sowers 2021)

3.2 Scenario description and Use cases

Consonant to the thermal extraction methods already apparent in literature and presented in chapter 2.2.1, a total of three different designs will be investigated in more detail within this work, while two of them belong to in-situ methods and the remaining one involves regolith excavation, as can be seen in Figure 3-2.

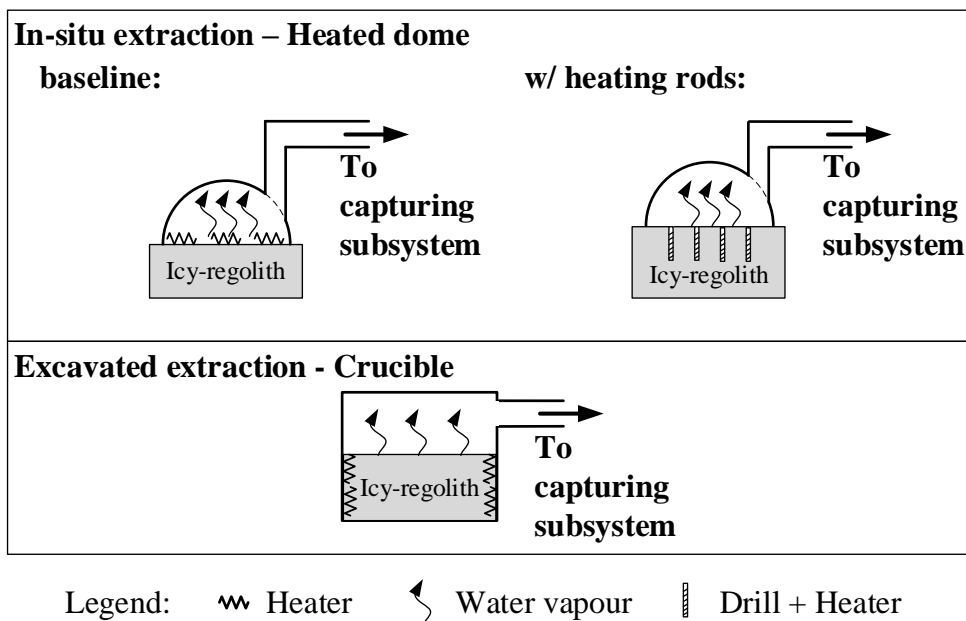


Figure 3-2: Overview of the investigated designs

The latter consists of a cylindric heating chamber with heating being applied to the lateral surface, in which the regolith is fed after being excavated. For the in-situ extraction, there is one version with just a dome to seal off the environment and a homogeneous and continuous surface heater, and another improved and more complex version with heating rods placed deep inside the regolith to facilitate the heat transfer. For each configuration, the total power input for the heating is kept constant (see chapter 5.1). To be able to extract the water ice from the lunar regolith without manipulation of the soil, it must be brought to vapor form, so it can outgas through the pores out of the ground. Due to high vacuum conditions on the lunar surface, this can be feasible via sublimation, thus the phase change from the solid state of water directly into the gas state, without passing through the liquid state (Figure 3-3).

The focus of the simulations only lies on the thermo-fluidic processes. External architecture or infrastructure normally needed to conduct nominal operations, eg. an excavation system, will not be considered, yet their impact will be discussed qualitatively.

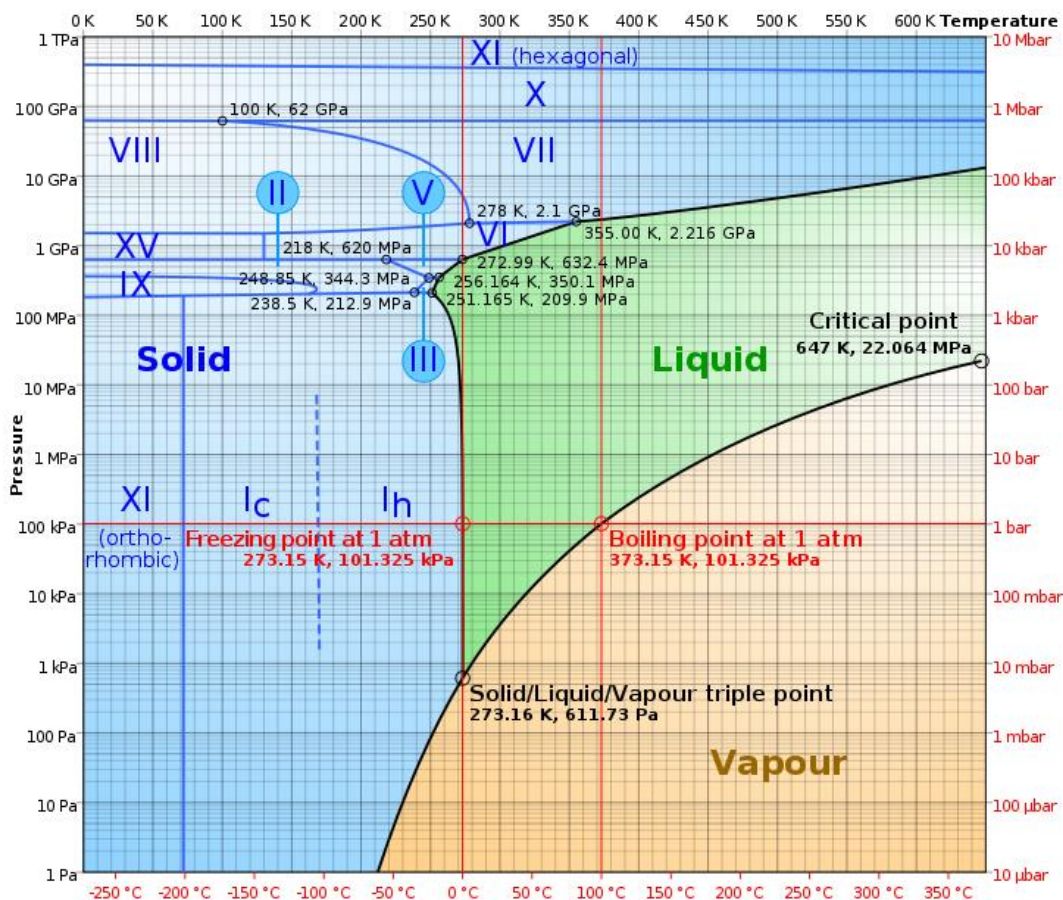


Figure 3-3: Phase diagram for water displaying the temperature and pressure-dependent boundaries between the solid, liquid, and vapor phases (Zhang et al. 2015)

Thus, the designs follow a minimal economically viable approach similar to the one proposed by Sowers (2021). By being self-supported systems, the likelihood of a quick and near-term system deployment is increased, also having a positive impact on overall costs, complexity, and reliability.

Furthermore, since water ice is expected to occur in three different geographical scenarios on the Moon, it can be varied between different use cases for thermal water extraction (see chapter 2.1):

- Use Case 1:** Conduct thermal water extraction within PSRs inside craters at the lunar poles
- Use Case 2:** Conduct thermal water extraction within so-called micro cold traps
- Use Case 3:** Conduct thermal water extraction outside PSRs in partly sunlit areas

For the respective cases, different thermophysical properties of the regolith-ice mixture and ambient conditions are expected. The highest water concentrations and at the same time lowest temperatures are thought to be within the PSRs, with water wt.% around 5 wt.% (Colaprete et al. 2010; Cannon and Britt 2020) (highest concentrations are believed to be up to 30 wt.%) as well as temperatures as cold as 40 K (Li et al. 2018). Inside micro cold traps, temperatures are expected to be a little higher but still cryogenic (in the range of 40-100 K) (Sefton-Nash et al. 2019) and similar water

concentrations of around 5wt. % (Hayne et al. 2021). In partly sunlit areas, temperatures can exceed 110 K, and thus water is only expected to be in molecular form mostly trapped within other minerals (Honniball et al. 2021).

While there are various degrees of heat needed to outgas volatiles from the regolith, depending on if water molecules are only loosely adsorbed, ice particles are present and sublimation is needed, or the water is trapped inside minerals (He et al. 2021), for simplification purposes it is assumed that water ice is only present as ice particles in each use case, neglecting desorption processes or mineral breakdowns to outgas the vapor. Furthermore, the baseline dry regolith is assumed to have the same thermophysical properties in each case. Thus, by investigating the different use cases in this work, only the ambient temperature, as well as the initial water content, will be adjusted, respectively.

3.3 System Requirements and Comparison Methods

To achieve the overall objective of the work set in chapter 1.2 and in consideration of the possible business cases and scenarios presented priorly, the high-level requirements for the systems can be derived, which can be seen in Table 3-3.

Table 3-3: Top-level requirements for the system designs

ID	Requirement
OB	Perform thermal water extraction on the lunar sub-/surface.
B	The system shall be able to extract at least 150 MT of water per year.
F-1	The system shall heat the water ice inside the regolith sufficiently for the ice to sublimate and the water vapor to outgas.
F-2	The system shall be sealed to the environment to mitigate losses.
F-3	The system shall collect the water vapor.
F-4*	The system shall be able to excavate lunar regolith and feed it into a heating chamber.

*only for excavation designs

The overall mission objective **OB** simply states that any design used shall be capable of performing thermal water extraction on the lunar surface. From that, business requirements **B**, and functional requirements **F** can be derived.

For a baseline business case, the first customer scenario presented in chapter 3.1 was chosen, namely, to provide a NASA lunar crew with enough propellant to be able to ascend to EML1 two times a year, with additional supply transportation for a lunar settlement, resulting in a water demand of approximately 150 MT/year. Considering in-situ surface heating, by interpolating possible water extraction yields and mining area requirements for different water contents presented in Kornuta et al. (2019), it can be assumed that for a water content of ~5 wt.% an area of ~6000 m^2 /year would be required for that goal, resulting in a yield of 25 kg/m^2 . This has been taken as the

minimum economically viable case. Other scenarios like water usage or oxygen production for life support systems are not being considered in this work.

The top-level functional requirements directly result from the mission objective. The whole functional process chain of in-situ thermal water extraction contains being able to sublimate the ice and transport the water vapor through the subsurface for it to outgas **F-1**, confining the water vapor to mitigate losses **F-2** and transporting it to some sort of a collection device, like eg. cold traps **F-3**. In the case of using cold traps for depositing the vapor again, dependent on the deposition rate and vapor amount, passive or additional active cooling may be needed (Sowers and Dreyer 2019). For excavation designs, the ability to excavate the regolith before transporting it inside eg. a heating chamber **F-4** is of course required as well. For this work, special emphasis is put on the functional investigation of the sublimation and outgassing process **F-1** as well as setting appropriate boundary conditions for sealing the system **F-2**, which will be covered by the simulations. The other functional requirements necessary for a holistic approach will only be discussed qualitatively.

Since the in-situ and excavated extraction methods are fundamentally different in their technology and system sizes can vary, besides the total water yield generated other comparison methods must be introduced to be able to make a relative comparison. For that, it can be distinguished between quantitative criteria, which can be directly calculated and derived from the simulations conducted in *COMSOL Multiphysics*, as well as qualitative factors needed for a comprehensive evaluation. Relevant qualitative factors enabling a relative comparison are:

- **Average Extraction Rate:** defined as the ratio of the total water yield extracted to the total simulated heating time
- **Energy Efficiency:** defined as the ratio of the total water yield to the total energy input during the total simulated heating time

Other criteria considered for a holistic system comparison on a qualitative basis are:

- **Lifetime:** The system must be able to be functional as long as needed to satisfy the demand set by the mission objective and business case.
- **Complexity:** The system complexity is highly interconnected with other criteria. Greater complexity may imply an increased performance risk due to the interaction of parts may introduce modes of failure. Furthermore, is it associated with higher integration costs.
- **Development Costs:** Costs are a decisive factor for the potential of realizing space systems. Due to still being in the concept generation phase for some of the required technology and given the ambitious nature of the mission, significant development costs are reasonably expected to accomplish a sufficient technology readiness level.
- **Reliability:** Due to being very cost-intensive concerning maintenance, if even possible, space elements should be single fault tolerance (“fail-ops”) for critical mission functions (according to Class B NASA mission as per NPR 8705.4) to minimize the risk associated with the accomplishment of the mission objective.
- **Accessibility:** Water ice accessibility determines how well or even if the system is capable of accessing the resource. This includes lateral and vertical accessibility.

While those factors are not per se qualitative and adequate metrics could be derived (eg. complexity (development time in hours), or costs (€)), the lack of present data prevents a profound quantitative evaluation. This also implies, that the importance of the single aspects can only be discussed subjectively, which includes any possible interconnections as well.

4 Heat and Mass Transfer in Lunar Regolith

Independent from the principle applied, the thermal extraction of water ice from lunar regolith underlies the same basic physics and mathematical behavior, consisting of both heat and mass transfer mechanisms. This chapter covers the fundamentals of said physics and further gives an overview of lunar ambient parameters and thermophysical properties of the regolith discussed in literature. For the heat and mass transfer mechanisms, especially the work conducted by Reiss (2018a), Wasilewski (2021a, 2021b) and Schieber et al. (2022) served as a baseline.

4.1 Heat Transfer

The general heat transfer equation is represented as:

$$(\rho C_p)_{eff} \frac{\partial T}{\partial t} + \rho_g C_{p,g} u \cdot \nabla T + \nabla \cdot q = Q \quad (4-1)$$

with

$$q = -k_{eff} \nabla T \quad (4-2)$$

with the density ρ , the specific heat capacity C_p , the temperature T , the thermal conductivity k , the convective term u , and a heat source term Q . The index $(\cdot)_{eff}$ in this case denotes the effective density, heat capacity, and thermal conductivity of the lunar regolith at every timestep, considering the phase change from ice to water vapor and thus from an icy soil $(\cdot)_{icy}$ to a dry soil $(\cdot)_{dry}$, with $(\cdot)_g$ accounting for the gas properties.

The first term on the left-hand side of equation (4-1) describes the temperature change over time within the regolith of the mixture of solid particles and gas in the voids. The second term stands for the convective heat transfer via the gas phase with Darcy velocity u and the third term describes conductive heat transfer through the mixture.

For near-vacuum conditions, the contributions of the gas term, thus the convective heat transfer, are considered to be minimal (Reiss 2018a). While the $(\rho C_p)_{eff}$ is in the range of 10^6 , the portion of the gas term is substantially smaller in the range of 10^{-1} with an initialization value in the order of 10^{-11} (for $C_{p,g} = 2000 \text{ J/kgK}$) (Schieber et al. 2022).

Subsequently, the convective part did not account for significant thermal transfer and was thus neglected, resulting in:

$$(\rho C_p)_{eff} \frac{\partial T}{\partial t} + \nabla \cdot q = Q \quad (4-3)$$

4.1.1 Phase Change & Regolith Density

Since the effective material properties change over time with the sublimation of ice into water vapor, this also must be accounted for in the calculations. The phase change properties of the ice sublimation within the regolith are calculated with the help of two phase indicator variables θ_1 , which stands for the icy phase, and $\theta_2 = 1 - \theta_1$, which represents the dried regolith. For the initially fully icy sample, θ_1 has a value of 1, as can be seen in Figure 4-1. Thus, the regolith has been divided into two phases with

different bulk properties $(\cdot)_{,b}$. The effective density ρ_{eff} , specific heat capacity $C_{p,eff}$ and thermal conductivity k_{eff} at every time are thus determined as follows:

$$\rho_{eff} = \theta_1 \rho_{icy,b} + \theta_2 \rho_{dry,b} \quad (4-4)$$

$$C_{p,eff} = \frac{1}{\rho_{eff}} (\theta_1 \rho_{icy,b} C_{p,icy} + \theta_2 \rho_{dry,b} C_{p,dry}) + L_{1 \rightarrow 2} \frac{\partial \alpha_m}{\partial t} \quad (4-5)$$

$$k_{eff} = \theta_1 k_{icy} + \theta_2 k_{dry} \quad (4-6)$$

Instead of adding the latent heat $L_{1 \rightarrow 2}$ from phase 1 to phase 2 in the energy balance equation (4-1) exactly when the material reached the sublimation temperature T_{pc} , it is assumed that the transformation occurs in a temperature interval between $T_{pc} - \Delta \frac{T}{2}$ and $T_{pc} + \Delta \frac{T}{2}$, resulting in a normal distribution of the latent heat around the phase change temperature. This is calculated though the change of mass fraction α_m :

$$\alpha_m = \frac{1}{2} \frac{\theta_2 \rho_{dry,b} - \theta_1 \rho_{icy,b}}{\theta_1 \rho_{icy,b} - \theta_2 \rho_{dry,b}} \quad (4-7)$$

The latent heat is furthermore lowered by the initial wt.% of water ice in the regolith w_i :

$$L_{1 \rightarrow 2} = L \cdot w_i \quad (4-8)$$

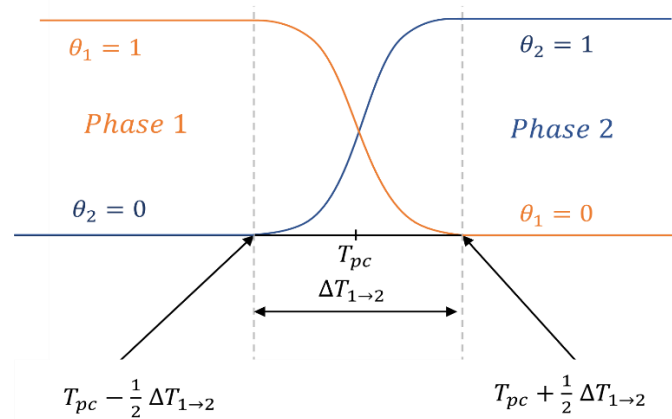


Figure 4-1: Material phase indicators θ_1 and θ_2 , phase change temperature T_{pc} and phase change transition interval $\Delta T_{1 \rightarrow 2}$

According to Hayne et al. (2017), the bulk density of the dry lunar regolith $\rho_{dry,b}$ is dependent on the depth with approximated values of 1100 kg/m^3 on the surface and 1800 kg/m^3 at deeper levels, with a fitted function for the density of dry regolith being (Vasavada et al. 2012; Hayne et al. 2017):

$$\rho_{dry,b} = 1800 - (1800 - 1100) e^{\frac{-z}{0.06}} \quad (4-9)$$

with z being the depth of the sample at any time, for $z = 0$ at the lunar surface.

Prior to that, Heiken et al., pp 483ff. (1991) also derived a depth-dependent porosity term by fitting measurements from the Apollo samples resulting in

$$\rho_{dry,b} = 1920 \frac{100z + 12.2}{100z + 18} \quad (4-10)$$

This formula is also being used in a recent study regarding water ice extraction by Schieber et al. (2022) and was thus chosen for this study.

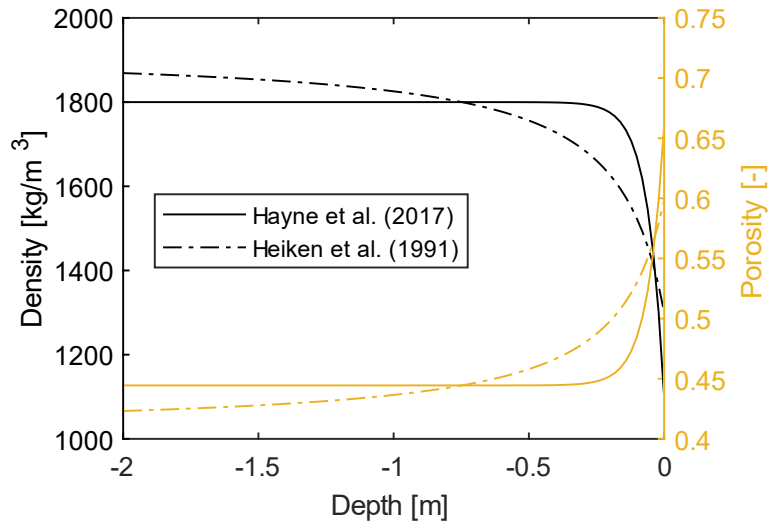


Figure 4-2: Comparison of density and porosity fits of dry lunar regolith concerning the soil depth

The bulk density of icy regolith $\rho_{icy,b}$ is calculated under the assumption that the additional ice in the soil accumulates uniformly within the pores of the regolith, thus increasing the effective porosity of the sample:

$$\rho_{icy,b} = \rho_{dry,b} + \rho_{i,b} \quad (4-11)$$

with $\rho_{i,b}$ being the bulk density of the ice

$$\rho_{i,b} = \bar{\rho}_{dry,b} \cdot w_i \quad (4-12)$$

and $\bar{\rho}_{dry,b} = 1400 \text{ kg/m}^3$ being the average density over the sample depth.

Dry regolith exhibits significant variability and dependency of especially temperature, pressure, and porosity, as seen in works conducted by e.g. Sakatani et al. (2018) and Woods-Robinson et al. (2019). In the following, said parameters will be described in more detail.

4.1.2 Thermal Conductivity Model

Dry Regolith

Over the years, a variety of thermal conductivity models for lunar regolith emerged in literature, whereas only a few apply to very low temperatures like in the PSRs (Parzinger 2014; Woods-Robinson et al. 2019). Heat transfer in planetary porous media mainly occurs through three primary nodes: conduction through solid grain contacts, radiation, and conduction through the gas. The effective thermal conductivity is typically treated as a parallel model, where all three modes may be summed together (Bergman and Incropera 2011). The physical contact conduction considers the area between the particles, though heat is transferred and thus depends mostly on the thermophysical properties of the regolith. For airless planetary bodies (i.e., low gas

pressures), solid conduction is considered to be proportional to the radius of the particles and is the dominant mechanism of heat transfer at cold to moderate temperatures (Ferrari 2018). Radiative heat transfer is considered to be the predominant form of heat transfer for coarse materials at high temperatures because it occurs through the pore spaces between grains (Martinez and Siegler 2021).

Because of the Moon's exosphere, the thermal conductivity of the gas can be negligible. Thus, one of the most common models first described by Watson (1964) simply states the thermal conductivity of a dry lunar soil sample $k_{dry,0}$ to be the sum of a temperature-dependent radiative terms A , as well as a temperature-independent solid conduction term B :

$$k_{dry,0} = A \cdot T^3 + B \quad (4-13)$$

In his theoretical and experimental works, Watson (1964) mainly investigated the thermal conductivity of airless planetary bodies in the temperature range from 150-350 K.

While conductivity values for temperatures below the Apollo 12 measurements of ~150 K were since estimated through extrapolation, previous studies indicate that the solid conduction term may overestimate the effective thermal conductivity by at least one order of magnitude (Woods-Robinson et al. 2019).

Models developed by Woods-Robinson et al. (2019), Sakatani et al. (2018), or also Wood (2020), who developed his so-called MaxTC model, demonstrate that particle size dependency is observable and enables explicit reliance on regolith thermal conductivity on its porosity, pore size, contact size, or particle shape. Thus, the models applied the temperature dependency also to the solid conduction term and additionally stated the parameters to be dependent on the porosity of the regolith. Furthermore, Woods-Robinson et al. (2019) also estimated the thermal conductivity for either crystalline or amorphous endmember lunar materials valid for temperatures down to ~15 K. A recent modeling effort by Hayne et al. (2017) on the other hand, which has been established as a standard model for lunar global modeling has used a thermal conductivity model with an alternate dependence on the solid density. Another current study conducted by Martinez and Siegler (2021) adapted the low-temperature thermal conductivity model developed by Woods-Robinson et al. (2019) and modified the density-dependent terms such that the conductivity profiles agree with the work from Hayne et al. (2017), to make the model applicable in a higher temperature range, working both at warm low altitudes and cooler high latitudes or for external heat application, resulting in:

$$k_{dry,0} = (A_1 \rho_{dry} - A_2) T^3 + (B_1 \rho_{dry} - B_2) k_{am} \quad (4-14)$$

with the temperature-dependent term k_{am} being a fitting function, and $A_1 - B_2$ being parameters modified according to match with average subsurface temperatures from Hayne et al. (2017).

However, to also study the development of thermal conductivity during a water extraction process over a wide range of temperatures and gas/vapor pressures, the gas conductivity k_g should also be accounted for. The driving factor for the gas term is the Knudsen Number Kn . While for normal lunar environmental conditions the pressure and temperature lead to $Kn > 10$, which results in a Knudsen Diffusion governed transport and thus a negligible gas term concerning the total conductivity, external

heating can change these conditions (see chapter 4.2.1). This makes it necessary to calculate the diffusivity dynamically during the extraction process. (Reiss 2018a)

The gas term k_g then should be accounted for:

$$k_{dry} = k_{dry,0} + k_g \quad (4-15)$$

The derivation of the gas term can be found in appendix 8B.1.

In his dissertation, after analyzing nearly 60 thermal conductivity models, Parzinger (2014) created a semi-empirical approach and developed a model that additionally taking not only the gas conductivity k_g into account, but also the coupling of solid and gas conduction k_{sg} , resulting in:

$$k_{dry} = k_{sc} + k_{rad} + k_g + k_{sg} \quad (4-16)$$

with the physical contact conduction k_{sc} , the radiation between the particles k_{rad} , the conduction through the gas in between the particles k_g as well as the coupling of solid and gas conduction k_{sg} . Figure 4-3 displays the importance of the single element for the thermal conductivity value for varying temperature and pressure conditions.

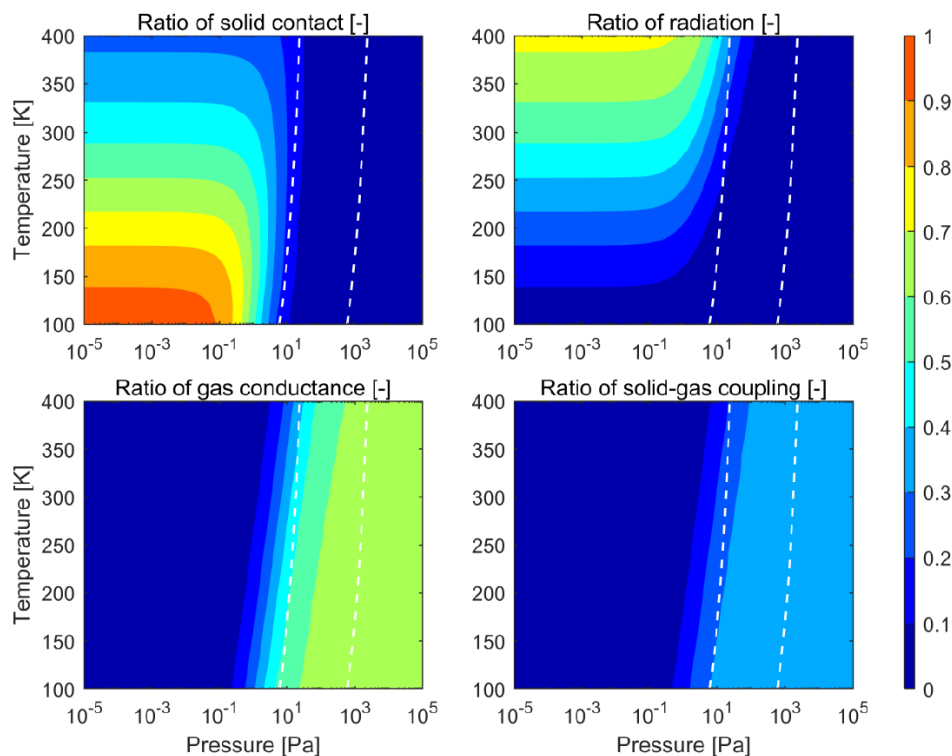


Figure 4-3: Ratio of contact, radiation, gas, and solid-gas coupling for the effective thermal conductivity according to Reiss (2018a). The left dashed line indicates $Kn = 10$, and the right dashed line indicates $Kn = 0.1$.

A detailed calculation of this thermal conductivity model can be found in the appendix. An overview of the most prominent thermal conductivity models for dry lunar regolith together with the model used in this study can be found in Table 4-1 and Figure 4-4.

Table 4-1. Effective thermal conductivity models for dry lunar regolith (grey: model chosen for this study)

Equation [$W/m \cdot K$]	Reference	Comment
$0.716 \cdot 10^{-3} + 0.254 \cdot 10^{-10} \cdot T^3$	(Cremers 1975)	
$AT^3 + B_c k_s$ where $A = 1.3 \cdot 10^{-11} [Wm^{-1}K^{-4}]$ $B_c = (9.9 \cdot 10^{-4} + 9.2 \cdot 10^{-10} \cdot \theta^2)(1 - \theta)$ $k_s = -2.03 \cdot 10^{-1} - 11.47 \cdot T^{-4} + 22.58 \cdot T^{-3}$ $\quad - 14.31 \cdot T^{-2} + 3.42 \cdot T^{-1}$ $\quad + 0.01 \cdot T + 2.80 \cdot 10^{-5} \cdot T^2 + 3.36 \cdot 10^{-8}$ $\quad \cdot T^3 - 1.40 \cdot 10^{-11} \cdot T^4$	(Woods-Robinson et al. 2019)	Provides high accuracy approximation even at extremely low temperatures (Apollo 12 fit)
$AT^3 + B_c k_s$ where $A = 3.31 \cdot 10^{-11}$; $B_c = 6.35 \cdot 10^{-4}$; $k_s = -9.53 \cdot 10^{-4} \cdot T + 2.4$	(Sakatani et al. 2018)	Experimental fit for JSC-1A at a bulk regolith density of $1690 \frac{kg}{m^3}$
$AT^3 + B_c$ where $A = 2.39 \cdot 10^{-11}$; $B_c = 9.15 \cdot 10^{-4}$	(Sakatani et al. 2018)	Experimental fit for JSC-1A at a bulk regolith density of $1870 \frac{kg}{m^3}$
$AT^3 + B_c$ where $A = 1.82 \cdot 10^{-10} \cdot \varphi^{1.84}$ $B_c = 9.40 \cdot 10^{-5} \cdot \varphi^{-2.06}$	(Sakatani et al. 2018)	Power law porosity fit for JSC-1A
$AT^3 + k_c$ where $A = \frac{k_c \cdot 2.7}{(350K)^3}$ $k_c = 3.4 \cdot 10^{-3} - (3.4 \cdot 10^{-3} - 7.4$ $\cdot 10^{-4}) \frac{1800kgm^{-3} - \rho_{dry}}{1800kgm^{-3} - 1300kgm^{-3}}$	(Vasavada et al. 2012; Hayne et al. 2017)	Commonly used global conductivity model for dry lunar regolith
$k_{sc} + k_{rad} + k_g + k_{sg}$ where $k_s = \frac{C_1}{T + 76.85} + C_2$ $k_{sc} = 3.44 \cdot (1 - \theta)^{\frac{4}{3}} \left(\frac{1 - \theta^2}{Y} \right)^{\frac{1}{3}} k_s p_s^{\frac{1}{3}}$ $k_{rad} = \frac{16\sigma n^2}{3E} T^3$ $k_g = \frac{k_{gas,0}}{1 + 2\beta \cdot Kn}$ $k_{sg} = (1 - \theta_{uc}) \frac{2r}{r^2 \pi} \sum_{i=1}^{1000} \left(\frac{h_{g,i}}{k_{gas,i} A_i} + \frac{h_{s,i}}{k_s A_i} \right)^{-1}$	(Parzinger 2014; Reiss 2018a)	Taking gas conductivity as well as the coupling of solid and gas conduction into account. (see appendix 8B.1)
$(B_1 \rho_{dry} - B_2) k_{am} + (A_1 \rho_{dry} - A_2) T^3$ where $B_1 = 5.0821 \cdot 10^{-6}$; $B_2 = 5.1 \cdot 10^{-3}$; $A_1 = 2.0022 \cdot 10^{-13}$; $A_2 = 1.953 \cdot 10^{-10}$ $k_{am} = -0.203297 - 11.472T^{-4} + 22.5793T^{-3} - 14.3084T^{-2}$ $\quad + 3.41742T^{-1} + 0.01101T$ $\quad - 2.8049E^{-5}T^2 + 3.35837E^{-8}T^3$ $\quad - 1.40021E^{-11}T^4$	(Martinez and Siegler 2021)	Merges (Woods-Robinson et al. 2019) with (Hayne et al. 2017) for a broader temperature range

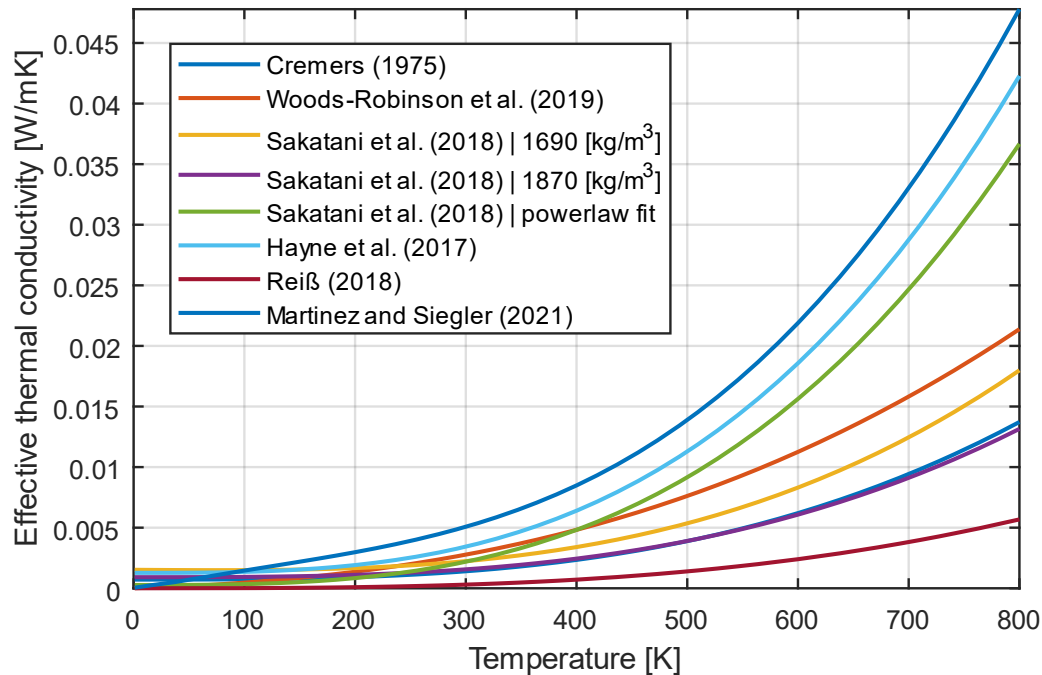


Figure 4-4: Common thermal conductivity models for dry lunar regolith at lunar ambient pressures

Icy Regolith

With two-phase materials like icy regolith, thermal conductivity can be approximated as a mixture of dry and pore-filling materials. The effective thermal conductivity may be higher by orders of magnitude if water ice is contained within the void spaces between particles. This can mainly be attributed to the increased cross-sectional area for conductive heat transfer. (Reiss 2018a)

Siegler et al. (2012) differ from three different types of mixing models: 1) a volumetric model, which assumes that ice content contributes proportionally to the overall thermal conductivity, 2) an “ice-neck” model first introduced by Mellon et al. (1997), or 3) a model simply based on empirical data from terrestrial soils. The latter was further broken down by Woodside and Messmer (1961), who distinguished between harmonic, geometric, and arithmetic models.

Even though those are approximations that can only hold in specific conditions, the volumetric mixing model was favored by eg. Siegler et al. (2012) due to its matching with experimental data of icy martian regolith and thus applicability for planetary icy environments. This approach calculates the effective thermal conductivity of icy regolith k_{icy} as:

$$k_{icy} = k_{dry} + \phi k_i F \quad (4-17)$$

with the thermal conductivity of the dry lunar soil k_r , the thermal conductivity of the ice k_i and the pore-filling fraction of the void between the particles F . The latter can be determined by (Reiss et al. 2021):

$$F = \frac{V_i}{\varphi \cdot V_r} = \frac{\rho_{dry} \left(\frac{1}{1-w_i} - 1 \right)}{\varphi \rho_i} \quad (4-18)$$

and the porosity φ of the icy regolith at any time (Schieber et al. 2022):

$$\varphi = 1 - \left(\frac{\rho_{dry,b}}{\rho_{dry}} + \frac{\rho_{i,b}}{\rho_i} \right) \quad (4-19)$$

with the particle density of the dry regolith $\rho_{dry} = 3240 \text{ kg/m}^3$, thus the density of the particles excluding the voids is from Apollo 15 (Heiken et al. 1991), and the particle density of ice $\rho_i = 916.7 \text{ kgm}^{-3}$ (Fukusako 1990).

The “ice-neck” model described by Mellon et al. (1997) and used by e.g. Hudson et al. (2009) calculates as follows:

$$k_{icy} = (1 - \sqrt{F})k_{dry} + \sqrt{F}k_i \quad (4-20)$$

This heavy dependence of this model on the filling fraction's square root for the thermal conductivity leads to a particularly steep gradient for low filling fractions.

The thermal conductivity of ice is often approximated as:

$$k_i = \frac{488.19}{T} + 0.4685 \quad (4-21)$$

According to Bonales et al. (2017), this equation holds on extremely low temperatures with a maximum between 2 and 9 K.

Yet, the mixing models presented are only estimates, they cannot sufficiently display the effect of inter-granular ice on radiation, gas conductivity as well as solid-gas interaction. Those contributions strongly depend on the way ice is formed on the particle surface, the amount of ice, and the change of ice layers over time. (Reiss 2018a)

4.1.3 Heat Capacity

For the overall specific heat capacity of the icy regolith $C_{p,icy}$, the same volumetric mixing model has been applied (Wasilewski 2021b):

$$C_{p,icy} = \frac{F\varphi C_{p,i}\rho_i + C_{p,dry}\rho_{icy}}{\rho_{eff}} \quad (4-22)$$

with the specific heat capacity $C_{p,i}$ of the ice and $C_{p,dry}$ of the dry regolith.

Overall, the heat capacity is both porosity and temperature dependent. For the dry lunar regolith $C_{p,dry}$, a model from Schreiner et al. (2016) is considered to provide a good approximation for temperature ranges between 90 K and 350 K. Other common specific heat capacity fits for the regolith are e.g. found in Hemingway et al. (1973), Ledlow et al. (1992), and Hayne et al. (2017). Another model by Woods-Robinson et al. (2019) fitted Apollo 12 measurements for high accuracy at very low temperatures of about ~15 K. The latter was also used in a recent study from Wasilewski (2021b) and provided valuable insights for heat transfer in PSR conditions and was thus used for this study as well. An overview of the different models for the specific heat capacity of lunar regolith including the model used in this work can be found in

Table 4-2.

The heat capacity of ice $C_{p,i}$ is temperature dependent as well (Flubacher et al. 1960). Commonly used approximations are eg. from Klinger (1981), Ellsworth and Schubert (1983), Fukusako (1990), and Shulman (2004). The latter provides a recent approximation valuable to non-stationary thermal processes at very low temperatures and was thus chosen for this study and can be calculated as follows:

$$C_{p,i} = 7.73e^{-3}(1 - e^{1.26 \cdot 10^{-3}T^2})(1 + e^{-3\sqrt{T}} \cdot 8.47 \cdot 10^{-3}T^6 + 2.08 \cdot 10^{-7}T^4e^{-4.97 \cdot 10^{-2}T}) \quad (4-23)$$

Table 4-2: Overview of common specific heat approximations for dry lunar regolith (grey: model chosen for this study)

Equation [J/kg · K]	Reference	Comments
$-1.12 \cdot 10^{-1}T + 9.62 \cdot 10^{-2}T^2 - 1.26 \cdot 10^{-3}T^3$ $+ 7.69 \cdot 10^{-4}T^4 - 2.37 \cdot 10^{-8}T^5 + 2.84 \cdot 10^{-11}T^6$ <i>for 10 K < T < 200 K</i>	(Woods-Robinson et al. 2019)	Provides good approximations at very low temperatures
$-5.84 \cdot 10^4 + 3.64 \cdot 10^3T - 2.03T^2 - 4.14$ $\cdot 10^{-3}T^3 + 3.87 \cdot 10^{-6}T^4$ <i>for 200K < T < 400K</i>		
$-23.17 + 2.13T + 1.50 \cdot 10^{-2}T^2 - 7.37 \cdot 10^{-5}T^3$ $+ 9.66 \cdot 10^{-8}T^4$ <i>for T < 350 K</i> $953 + 0.25T - 2.65 \cdot 10^7T^{-2}$ <i>for 350 K < T < 1500 K</i>	(Schieber et al. 2022; Schreiner et al. 2016)	Combines Hemingway et al. (1973) and Stebbins et al. (1984)
$3.61 + 2.74T + 2.36 \cdot 10^{-3}T^2 - 1.23 \cdot 10^{-5}T^3$ $+ 8.91 \cdot 10^{-9}T^4$	(Ledlow et al. 1992; Hayne et al. 2017)	Common global model

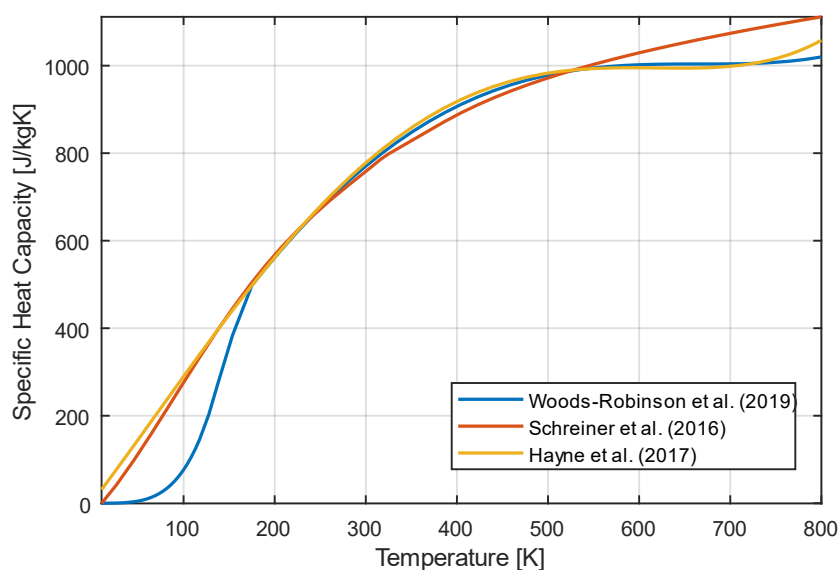


Figure 4-5: Overview of common specific heat approximations for dry lunar regolith

4.2 Mass Transfer

According to e.g. Webb (1996), Reinecke and Sleep (2002), Ho (2006), He et al. (2013), and Schieber et al. (2020), gas transport in a porous medium can be divided into a diffusive, further distinguished between ordinary and Knudsen diffusion, and an advective flow. At low pressures, the transport through porous media is analogous to gas flow within microchannels, where Knudsen and ordinary diffusion are relevant. At higher pressures within the void spaces, advective transport is dominating (Schieber et al. 2020).

To account for both every transport mechanism and cover the transition regime, the general form of the Advection-Diffusion equation for mass transfer can be used. The diffusive and advective terms for the transport, which will be further presented in more detail in the following, can be simply added together to determine the overall gas flow for a single species of gas (Webb 1996; Reiss 2018a):

$$\frac{\partial c}{\partial t} + \nabla \cdot (-D\nabla c - uc) = Q_m \quad (4-24)$$

with the concentration c , the diffusion coefficient D , the conservative convection coefficient u , and the mass source term Q_m . For a single species flow, the concentration c can be replaced with the density of the fluid, which is in our case the water vapor density ρ_g (Kast and Hohenthanner 2000; Bravo 2007). For ideal gas behavior, the latter can also be expressed according to the ideal gas law as $\rho_g = \bar{p}/(RT)$. In equation (4-24) the second term on the left-hand side describes diffusion and the third term is advection.

For microchannels and porous media, flow regimes are categorized by the dimensionless Knudsen number Kn , which is representing the relative likelihood of molecular collisions with other gas molecules or with a solid surface and is used as a metric for defining continuum flow (Reiss 2018a):

$$Kn = \frac{\lambda}{d_v} \quad (4-25)$$

with the mean free path λ and the diameter of the void spaces between the particles d_v . The former can be calculated as

$$\lambda = \frac{k_B T}{\sqrt{2} p \pi d_g^2} \quad (4-26)$$

with the Boltzmann constant k_B , the temperature T , the pressure p , and the effective diameter of a gas molecule d_g .

The Knudsen number is used to differentiate between ordinary and Knudsen diffusion. While there is no exact definition of the boundary between these two mechanisms it is commonly said that for $Kn \ll 0.1$, where the void spaces are much larger than the mean free path and the flow is dominated by intermolecular collisions, ordinary diffusion is the dominating diffusion process. Accordingly, for $Kn \gg 1..10$ Knudsen diffusion and thus wall-molecular collisions dominate. At $Kn \sim 1$, there is a complex

interplay between the relative effects of intermolecular collisions and wall-molecular collisions. (Reiss 2018a; Schieber et al. 2020)

To define the boundaries more clearly, in total, the flows can be divided into four different regimes: **(1) continuum** ($Kn < 0.01$), **(2) slip** ($0.01 < Kn < 0.1$), **(3) transition** ($0.1 < Kn < 10$), and **(4) Knudsen** ($Kn > 10$) (Socio and Marino 2006; Bravo 2007; Schieber et al. 2020). Figure 4-6 illustrates the relevance to various applications as a function of the water vapor pressure p_g given at 400 K.

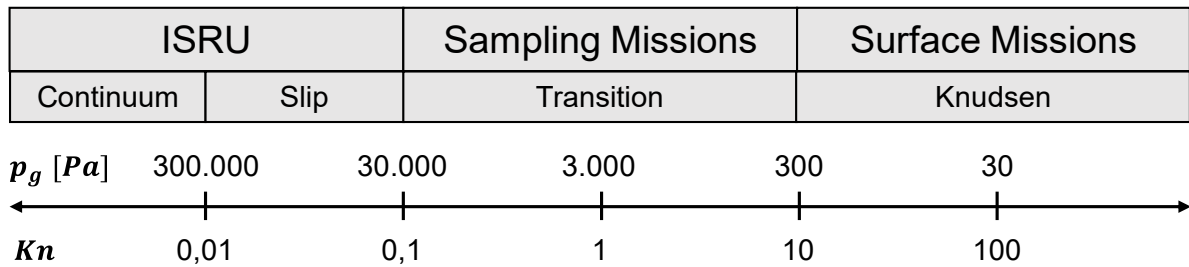


Figure 4-6: Application relevance according to the corresponding Knudsen number for water vapor pressures p_g at 400 K (Schieber et al. 2020)

4.2.1 Diffusion

At normal lunar conditions, the environment pressure and temperature lead to a Knudsen number above 10 and, thus, to a Knudsen diffusion-governed transport. If through external heating the pressure and temperature would change, however, transport mechanisms in the transition, slip, or continuum region could occur. This makes it necessary to calculate the diffusivity dynamically during the water extraction process. (Reiss 2018a)

Both ordinary and Knudsen diffusion can be described by Fick's first law

$$J_D = -D\nabla c \quad (4-27)$$

with the diffusion coefficient D and the concentration gradient ∇c . Ordinary diffusion can be calculated using the mean thermal velocity \bar{v} with the universal gas constant R and the molecular weight M , which leads to (Evans et al. 1961; Jackson 2012):

$$D_O = \frac{\lambda}{3} \bar{v} \quad (4-28)$$

with the mean free path λ , and Knudsen diffusion:

$$D_K = \frac{d_v}{3} \bar{v} \quad (4-29)$$

with the mean void size d_v .

The mean thermal velocity \bar{v} can be defined as:

$$\bar{v} = \sqrt{\frac{8RT}{\pi M}} \quad (4-30)$$

Yet, since equations (4-28) and (4-29) are only valid for parallel cylindrical voids leading to an unobstructed path for the diffusion, the effective diffusivity has to be calculated by taking the porosity regolith φ and tortuosity τ into account.

This results in the effective diffusion coefficients for ordinary and Knudsen diffusion as

$$D_{O,eff} = \frac{\varphi}{\tau} \cdot D_O \quad (4-31)$$

and

$$D_{K,eff} = \frac{\varphi}{\tau} \cdot D_K \quad (4-32)$$

To combine the two diffusive mechanisms, the effective diffusion coefficients can be linked according to the "resistance in series" approach (Clifford and Hillel 1986):

$$\frac{1}{D_{eff}} = \frac{1}{D_{O,eff}} + \frac{1}{D_{K,eff}} \quad (4-33)$$

The porosity φ of the lunar regolith can be calculated with equation (4-19). The tortuosity τ expresses the deviation from a straight microchannel to a tortuous channel that develops in the porous medium formed by particle packing. While there are various values and models for the tortuosity of porous media like the Millington model (Millington 1959) or Bruggeman model (Tjaden et al. 2016), the methods for predicting τ were based on the properties of the medium as outlined by Ghanbarian et al. (2013):

$$\tau = 1 - p_\tau \ln \varphi \quad (4-34)$$

with p_τ being the shape factor of the particles. Based on the lunar regolith simulant JSC-1A, p_τ was reported as 0.49 for perfect spheres and up to 3.2 for very plate particles (Comiti and Renaud 1989). Thus, p_τ was conservatively estimated to be 0.60 to account for the expected increase in tortuosity when compared to perfect spheres (Schieber et al. 2020). Figure 4-7 shows the shape as well as particle sizes of JSC-1A.

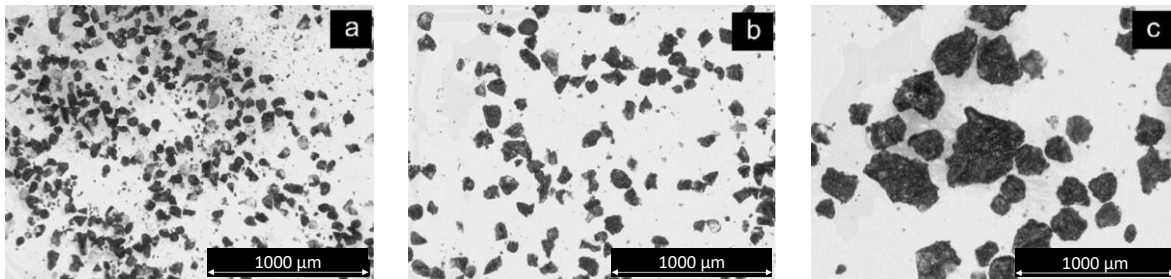


Figure 4-7: Microscopic images of the lunar simulant JSC-1A, including (a) fines < 90 μm , (b) particles in the size range of 90 μm –150 μm , and (c) particles that are >150 μm (Schieber et al. 2020)

In the case of icy regolith, porosity, tortuosity, and void size are significantly affected (Hudson et al. 2007). As the voids are effectively reduced, the regime for molecular transport shifts towards Knudsen diffusion. This can be accounted for by correcting the void size and thus the flow diameter, assuming a proportional reduction related to the reduction in volume that corresponds to the addition of ice to the dry regolith (Schieber et al. 2022):

$$d_{v,i} = \sqrt{\frac{\varphi}{\varphi_{dry}}} d_v \quad (4-35)$$

Nevertheless, because we don't have further knowledge regarding the exact state of water ice within the regolith (see chapter 2.1.2), the ice can take a variety of different shapes, making it difficult to quantify the exact implications for the transport of water through icy regolith.

4.2.2 Advection

Another part of the mass transfer is the advective flux of the volatiles through the porous medium. This transport can be described by Darcy's Law, represented as:

$$J_c = c \cdot u = -c \frac{\vartheta_{g,a}}{\mu} \nabla p \quad (4-36)$$

with the concentration c and the Darcy velocity u . The latter can be calculated with the apparent gas permeability $\vartheta_{g,a}$, the dynamic viscosity μ , and the pressure gradient ∇p . (Reinecke and Sleep 2002)

In this form gravity effects are assumed to be negligible compared to the applied pressure gradient. To account for the gas saturation, which is the fraction of the void volume occupied by the gas, and slip effects inside of the porous regolith, which increases the apparent permeability, its value has to be adjusted with the help of the Klingenberg parameter b (Reinecke and Sleep 2002):

$$\vartheta_{g,a} = \vartheta_{g,e} \left(1 + \frac{b}{\bar{p}}\right) \quad (4-37)$$

with the average pressure \bar{p} .

Regarding the gas permeability of the lunar soil, LaMarche et al. (2011) conducted a series of experiments on the permeability of JSC-1A and derived an approximation dependent on the porosity and pore-filling fraction of the ice:

$$\vartheta_{g,e} = 2 \cdot 10^{-14} \cdot e^{12.469 \cdot \varphi \cdot (1-F)} \quad (4-38)$$

This is also in accord with values determined from firing tests with the Surveyor 5 Vernier engine on the lunar soil, which estimated permeability values in the range of $1 \times 10^{-12} \text{ m}^2$ to $7 \times 10^{-12} \text{ m}^2$ (Christensen et al. 1967), or other measurements with lunar simulants conducted by (Toutanji et al. 2012), who revealed values from $3 \times 10^{-13} \text{ m}^2$ to $2 \times 10^{-12} \text{ m}^2$ for JSC-1A and $9 \times 10^{-14} \text{ m}^2$ to $1 \times 10^{-12} \text{ m}^2$ for NU-LHT.

While the dynamic gas viscosity μ is normally dependent on the flow regime and can be distinguished between flow in the viscous regime for $Kn < 1$ and flow in the free-molecular regime for $Kn > 1$ (Reiss 2018a), it was assumed to be $\mu = 0.017 \cdot 10^{-3} \text{ Pa} \cdot \text{s}$ according to Wasilewski (2021a).

4.2.3 Sublimation Model

For the water vapor to be able to outgas out of the regolith, it first either has to sublimate, be deported, or be set free from being inside other minerals. Yet, since ground truth data verifying the exact state of the water ice within the regolith is still missing, confident statements about whether or how it is bound on a molecular basis to the particles cannot be made. (see chapter 2.1.2) Thus, in the context of this work,

the water ice was treated as discrete (compare Figure 2-4), and any possible sorption processes were neglected. Thus, the vapor generation was solely based on sublimation. Furthermore, since in this work rather high water ice wt.% are investigated, the impact of desorption compared to sublimation is expected to be minimal (Schieber et al. 2022).

As a result, the water vapor production rate within the regolith sample was calculated only due to the phase change of the ice, and thus due to the change of concentration of the ice. Thus, the mass continuity equation represents the change in the bulk density of the ice $\rho_{i,b}$ within the regolith over time:

$$\frac{\partial \rho_{i,b}}{\partial t} = Q_m \quad (4-39)$$

According to Andreas (2007) and Haynes et al. (1992), the sublimation rate S of can be defined as:

$$S = p_{pc} \sqrt{\frac{M}{2\pi RT}} \quad (4-40)$$

with p_{pc} being the sublimation pressure, also called saturation or equilibrium pressure, the molar mass of water M , the universal gas constant R , and the temperature T . During the sublimation of the ice into vapor, the remaining regolith was assumed not to settle or compact.

There are various approaches to calculating the saturation pressure at lower temperatures (Marti and Mauersberger 1993; Fray and Schmitt 2009; Buck 1981; Murphy and Koop 2005; Feistel and Wagner 2007; Schorghofer and Taylor 2007). Especially the model by Murphy and Koop (2005) shows good agreement at lunar cold trap environments with temperatures under 100 K and is used in recent works by eg. Schieber et al. (2022) for calculating the sublimation rate. An overview of the most prominent models for the sublimation pressure can be found in Table 4-3

Adequately, the deposition rate D of the vapor back to ice can be calculated as (Haynes et al. 1992):

$$D = -p_g \sqrt{\frac{M}{2\pi RT_g}} \quad (4-41)$$

with p_g and T_g being the pressure of the water vapor. By assuming local thermal equilibrium, T_g can be equated with T .

By combining the sublimation rate with the deposition rate, the overall phase change rate can be derived (Schieber et al. 2022):

$$Q_m = s_v (p_{pc} - p_g) \sqrt{\frac{M}{2\pi RT}} \quad (4-42)$$

with $s_v = s_m \cdot \rho_{i,b}$ being the surface area volume of ice within each cell, and s_m being the specific surface area per mass, which was assumed to be $0.5 \text{ m}^2/\text{g}$ (Heiken et al. 1991).

Table 4-3: Common models for the sublimation pressure of water

Equation [Pa]	Temperature Range	Reference
$p_{pc} = \exp \left(9.550426 - \frac{5723.265}{T} + 3.53068 \ln(T) - 0.00728332 \cdot T \right)$	110 K < T < 273.15 K	(Murphy and Koop 2005)
$p_{pc} = p_t \cdot \exp \left(-Q/R \left(\frac{1}{T} - \frac{1}{T_t} \right) \right)$	N/A	(Schorghofer and Taylor 2007)
$p_{pc} = 611.15 \cdot \exp \left(\frac{22.542(T - 273.15)}{273.48 + (T - 273.15)} \right)$	193.15 K < T < 273.15 K	(Buck 1981)
$p_{pc} = 10^{\frac{-2663.5}{T} + 12.537}$	N/A	(Fray and Schmitt 2009)

5 Computational Setup

This chapter provides an overview of the implementation of the presented mechanisms to the simulation models in the software *COMSOL Multiphysics*. In total, three different models are built and investigated, (1) baseline in-situ surface heating, (2) improved in-situ rod heating, and (3) heating via a heating chamber after prior excavation of the regolith (see chapter 3.2). In the following, the respective models are further addressed by their numbers **(1)**, **(2)**, and **(3)**.

The implementation includes the geometry description as well its discretization together with the according boundary conditions and initial conditions for each model. Furthermore, additional assumptions and simplifications regarding the models are presented. Afterward, further preliminary studies regarding the mesh size and the numerical solver setup including the time step size are presented.

5.1 Implementation of the Models

5.1.1 Design variables

Following the use cases (chapter 3.2) and the system requirements (chapter 3.3), the COMSOL simulations are carried out for varying input parameters: the water ice content of the regolith w_i , total heating power that is available Q , and the surface heat flux q .

The latter is calculated with the unit *sol*, which is accounted for with $1 \text{ sol} = 1367 \text{ W} \cdot \text{m}^{-2}$ according to a solar constant. Even though the heating function in the models is implemented to be solution neutral, a possible option as a power source for thermal water extraction is solar heating (Sowers and Dreyer 2019). Yet, thermal mining optics have not been developed so far, thus actual heat fluxes may be higher if the sunlight can be concentrated or lower to due apparent losses like flux mitigation through the dust. The lower and upper boundaries of the power density were determined via preliminary studies in *COMSOL Multiphysics*. For the in-situ surface heating, it was found that at least $q_{min} = 0.5 \text{ sol}$ are needed to reach sublimation of the water ice in at least 2 cm of the soil. On the other hand, a flux higher than $q_{max} = 2 \text{ sol}$ elevated the regolith temperature in sintering conditions. This would not only reduce the energy efficiency of the system greatly but also would hinder water vapor from diffusing through the soil by fusing the regolith pores, preventing in-situ extraction. Furthermore, this would significantly increase modeling complexity since a double-phase change system would be needed.

The heating power Q was selected in accordance with sources commonly available for lunar rovers like the Lunar Rover Vehicle (LRV) deployed during the Apollo missions, which was equipped with a total power availability of $\sim 1 \text{ kW}$ (Lund 2018). The total heating power was thus chosen to be in the same order of magnitude ranging from 500 W to 2500 W. The initial water ice content was set according to the findings in the literature study in chapter 2.1, ranging from 1 wt.% up to 15 wt.%, with 5 wt.% measured by LCROSS being chosen as the baseline scenario. Yet, while Li et al. (2018) estimate water ice contents of up to 30 wt.%, the upper boundary for the study was set to keep the pore-filling fraction of the ice below 0.9 for the chosen porosity due to the volumetric mixing model applied. For pore filling fraction greater than that, either

due to a higher regolith bulk density or more water ice, the mixing should be more geometric (Siegler et al. 2012).

A summary of the model input variables for the parameter study can be found in Table 5-1. The values in bold represent the respective baseline scenario. Since the total heating power Q is a design constraint, following the range of power densities applicable to the certain case, the size of the extraction system is dependent on the latter for the in-situ surface heating (1) (see Table 5-3). This results in a total of $3^3 = 27$ simulations conducted for the surface heating method. For both the in-situ rod heating (2) and the excavated design (3), for simplicity reasons a fixed system size was chosen in that way so that the resulting power fluxes roughly match the ones for (1). This reduced the number of simulations for the parameter study to $3^2 = 9$ runs for both (2) and (3). Further information regarding the geometry and sizes of the respective models is provided in the following.

Table 5-1: Overview of the model variables for the parameter study with values in bold accounting for the baseline scenario

	Water Ice Content w_i [%]	Heating Power Q [W]	Power Density q [sol]
In-Situ Surface Heating	1; 5 ; 15	500; 1500 ; 2500	0.5; 1 ; 2
In-Situ Rod Heating	1, 5 , 15	500; 1500 ; 2500	-
Crucible Heating	1, 5 , 15	500; 1500 ; 2500	-

5.1.2 Assumptions

For the main parameter study investigating the performance of the respective water extraction methods, the heat and mass transfer mechanisms linked through the phase change modeling had to be decoupled.

A preliminary study considering the pressure driven mass transfer equations presented in chapter 4.2 was conducted to investigate vapor concentration and pressure gradients in the regolith domain for the in-situ methods, indicating the outgassing potential as well as the risk of redeposition of the vapor within the soil. This study entailed three dependent variables, namely the temperature T , the pressure p , as well as the concentration of the ice c_i within the regolith. The modeling of the dome sealing the surface and a subsequent vapor pressure build-up inside of it during the vapor extraction phase has been neglected. For a constant surface pressure of $3 \cdot 10^{-10}$ Pa, pressure gradients were always positive from the sublimation interphase to the regolith surface, so no redeposition of vapor was expected to happen in the desiccated domain. Yet, when initially sublimating, a fraction of the vapor can also diffuse shortly towards the inside of the domain (if the ice is not fully saturating the porous regolith), where it is expected to redeposit rather quickly again, resulting in an ever-growing “icy plate” along the phase change interphase. The average percentage of the vapor still being redeposited below the phase change interphase after the simulated timeframe over different initial water contents up to 15 wt.% was $\sim 10\%$. This value was taken and

applied to assume the possible vapor losses during the extraction process for the design variable study (see chapter 5.1.5).

The main study investigating the influence of the design variables on possible yield, extraction rate, or energy efficiency was conducted putting special emphasis on the correct representation of the thermophysical properties of the regolith and their dynamic change due to the phase change of the ice into water vapor. While the pressure domain is still being considered for the simulation, resulting in two dependent variables, the temperature T , and the pressure p , the source term for the vapor generation was set to a minimal value to stabilize the convergence of the simulation and setting the pressure gradient was set to be nearly constant. Yet, especially both the effective thermal conductivity k_{eff} and the phase change temperature T_{pc} are expected to vary significantly with the changes in pressure (see Figure 3-3 and Figure 4-3, respectively). This can be improved and implemented in future work (see chapter 8).

Following these assumptions, the sublimation temperature T_{pc} and the transition interval of the phase change process $\Delta T_{1 \rightarrow 2}$ were set to constant values for the main study. In accordance with Wasilewski (2021b), for the sublimation temperature, the triple-point temperature of the water was chosen to be an adequate approximation, as it is claimed that the porous space and impurities make water ice increasingly more stable in a vacuum (Kossacki and Leliwa-Kopystynski 2014). These effects have also been investigated and are well established in research on freeze-drying, a drying method in the food industry having many parallels to thermal mining that has been employed in numerous terrestrial industries over the past few decades, where they lower performance (El-Maghlany et al. 2019; Vorhauer-Huget et al. 2020). When the proper amount of heat is applied to a particular volume, the phase change temperature is the isotherm that shows that most of that volume has transitioned from an icy phase to a desiccated phase. In contrast to conventional equations derived from phase change diagrams, this method is pressure-independent and allows for phase transition if the phase change temperatures are reached (Wasilewski 2021b).

As described in chapter 4.1.1, the phase change transition interval $\Delta T_{1 \rightarrow 2}$ indicates the range where the phase change starts and ends, by applying the latent heat in a normal distribution around the phase change temperature ($\Delta T_{1 \rightarrow 2} = 50 \text{ K}$ means that the phase change starts at $T_{pc} - \frac{\Delta T_{1 \rightarrow 2}}{2}$ and is fully completed at $T_{pc} + \frac{\Delta T_{1 \rightarrow 2}}{2}$). While in pure materials, often an isothermal phase change is occurring, in impure materials a continuous properties phase change allows for a more natural transition by accounting for conversion layers (Nazzi Ehms et al. 2019). According to experiments on the sublimation of frozen regolith, the gradual increase in the slopes of temperature and pressure over time may indicate long transition intervals (Kossacki and Leliwa-Kopystynski 2014). The upper layer of the lunar soil was assumed to be in equilibrium with lunar ambient temperatures in PSRs. The parameters chosen for the main design study are presented in Table 5-2.

Table 5-2: Model input parameters concerning the deposit stability

Parameter	Value	Reference
Ambient/initial temperature	$T_{amb} = 40 \text{ K}$	(Williams et al. 2019)
Phase change temperature	$T_{pc} = 273 \text{ K}$	(Wasilewski 2021b)
Phase change transition interval	$\Delta T_{1 \rightarrow 2} = 100 \text{ K}$	(Wasilewski 2021b)

5.1.3 Geometry Description and Boundary Conditions

The geometries of the respective thermal extraction methods were simplified as much as possible to save modeling effort and computational time without impacting the results. Thus, for each design, only the regolith domain was modeled. Other parts of the system like the walls and insulation of the heating chamber or the heated rods have been acknowledged via the boundary conditions.

While (1) and (3) could be implemented as a 2D-axisymmetric model, saving a lot of computational effort and time, (2) had to be modeled in 3D. An overview of the geometry implemented in COMSOL for each design including their top-level boundary conditions can be seen in Figure 5-1. To still reduce the model size of the 3D-model as much as possible, the axisymmetric symmetry of the geometry (2a) in Figure 5-1 could be used to cut the geometry in a circle segment, being only one-sixth of the original model size (2b).

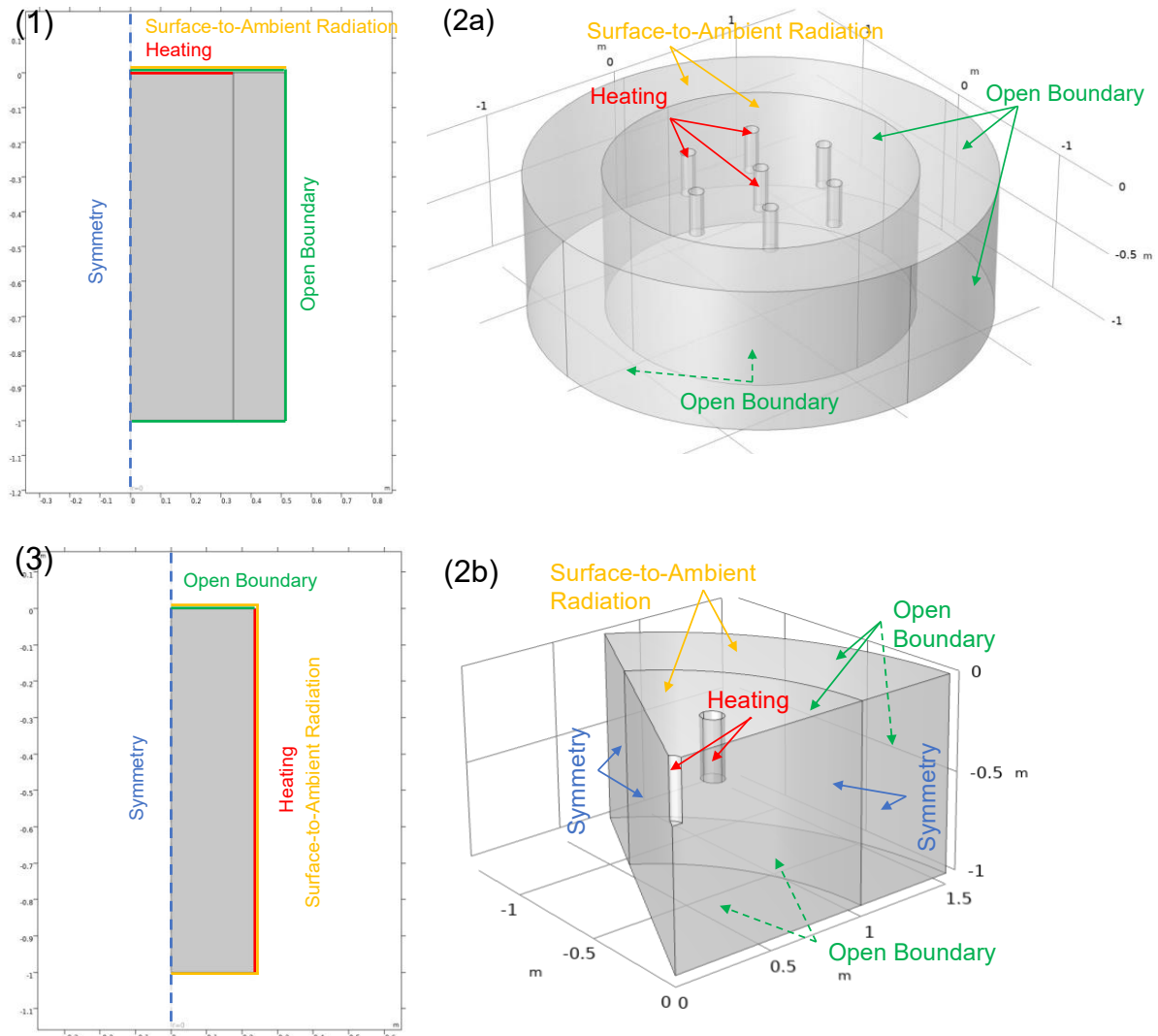


Figure 5-1: Geometry of the investigated designs with their respective top-level boundary conditions: (1) in-situ surface heating, (2) in-situ rod heating (a) whole geometry b) simulated section), (3) heating inside a heating chamber after excavation

As described earlier, the focus of this work is to determine the total water yield as a baseline generated for each design given both a time and power constraint. While the simulation time only has an impact on the solver setup in the software, the available power input Q gravely affects the ability of the system to sublimate the ice within the regolith successfully. Since different designs with varying geometries and distinct heating surfaces are investigated, to enable a consistent and reliable comparison of the said designs regarding their performance, the power flux q had to be set identical for each configuration.

For the applied heat flux q , the unit was called *sol* and has a value of $1 \text{ sol} = 1366 \text{ W/m}^2$, thus it is dependent on the heated surface, which. Subsequently, for the baseline in-situ surface heating (1), varying the total power Q with a constant flux q greatly impacts the heated surface and thus the system size. The sample radius in this case refers to the heated surface and thus to the dome size, while the outer regolith ring was applied to account for adequate boundaries of an open system. Table

5-3 provides an overview of the resulting system diameter regarding the investigated total power inputs Q and fluxes q .

Table 5-3: Power and power density influence on in-situ dome diameter for surface heating

Power [W]	Power Density [W/m ²]	Surface Area [m ²]	Diameter [m]
500	683	0,73	0,97
500	1366	0,37	0,68
500	2732	0,18	0,48
1500	683	2,20	1,67
1500	1366	1,10	1,18
1500	2732	0,55	0,84
2500	683	3,66	2,16
2500	1366	1,83	1,53
2500	2732	0,92	1,08

For rod heating (2), a constant dome radius of 1 m was chosen. By applying the heat flux via the surface of the rods, the effective surface area was dependent on the rod size and number, which do not impact the system size directly. The latter were chosen based on the work conducted by Song et al. (2021). In total, a constellation of 7 rods distributed equally within the cylindric sample (one rod in the middle, and the remaining circularly with an angle of 60° at half of the sample radius D), with a height of 0.3 m, and a radius of 0.05 m was investigated. (see Figure 5-2) other rod configurations are not further explored in the course of this work, yet first results on the implications of different rod quantities and distributions can be found in Song et al. (2021).

Since sublimation was only expected to happen in the very top layers for the in-situ design in the maximum range of 10-15 cm due to the poor thermal conductivity of the lunar regolith (Wasilewski 2021b; Schieber et al. 2022), a sample depth of 1 m was chosen for both in-situ methods (1) and (2), to still be able to resolve the phase change accurately without restricting the design space.

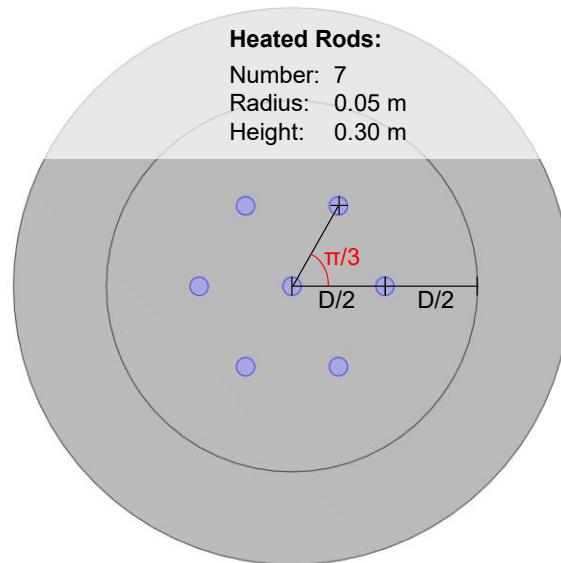


Figure 5-2: Rod constellation of the investigated rod-heating design (2)

In accordance with (Reiss 2018b), the most common shape for sampling ovens is a cylindric form. Thus, the heating chamber of the excavated method **(3)** was chosen to be cylindric for this study, as well. When heating is applied to the lateral surface, the performance and efficiency of the cylindric shape are expected to be the best compared to other shapes eg. such as a cube. Since the heating chamber design in this work furthermore is gravely simplified, without investigating different heating integration possibilities or insulation methods, other shapes were not deemed to add more insights and were thus not considered in this work. Besides investigating different heating methods for crucibles and the resulting heat distribution within the chamber, an overview of possible insulation designs for a heating chamber can be found in Hager and Binns (2021).

The exact dimensions of the geometry were chosen according to a predefined volume. Considering current regolith excavation technologies (Just et al. 2020) combined with preliminary simulation and experimental results regarding sublimation interphase depths within lunar regolith (Wasilewski 2021a, 2021b), Kiewiet et al. (2022) determined a reasonable volume of a heating chamber to hold up to 250 kg of regolith. Again, due to the low general thermal conductivity of the lunar regolith, the diameter of the cylinder was chosen to be as little as possible to minimize the distance between the heated surfaces, while at the same time considering a reasonable structural oven design and assuring that with the minimal heat flux q sublimation temperature is still reached. This resulted in a fixed height of as well 1 m and a radius of an average of 0.23 m. Similar to (1), the latter has a dependence on the initial ice content of the regolith. Assuming a volumetric mixing model and the additional ice accumulating within the pores, more ice equals a higher effective density of the material (less volume required to incorporate the same mass of regolith. Yet, its implications on the final radius are minimal, ranging from 22.23 cm for an initial ice content of $w_i = 15 \text{ wt. } \%$ to 23.72 cm for an ice content of $w_i = 1 \text{ wt. } \%$.

Regarding the thermophysical properties of the lunar regolith, it has to be noted that it was assumed that the excavation and transportation inside a heating chamber of the latter do not affect its density or porosity compared to the in-situ designs. Also, initial

pressures within the regolith domain were assumed to have no effect inside the heating chamber.

Boundary conditions

As already mentioned, in addition to the geometry of the respective systems, Figure 5-1 also displays their boundary conditions (BCs). In general, each system from (1) to (3) has the same BCs applied to different surfaces, yet with partly varying numerical values. The boundary conditions for the heat transfer together with the initialization conditions valid over the whole domain are provided in Table 5-4. While the surface heat flux is a variable of interest and was thus varied during the parameters study (see chapter 5.1), the other values are fixed. The equilibrium temperature in the PSRs is considered to be around 40 K (Williams et al. 2019), thus a background radiation temperature of $T_{amb} = 40\text{ K}$ was chosen, which was also assumed to be in equilibrium with the investigated top-layer regolith temperature at steady state. The radiation to outer space due to the lack of atmosphere was neglected. This assumption was also made for the lunar ambient pressure. With $p_{amb} = 3 \cdot 10^{-10}\text{ Pa}$, the apparent exosphere provides near vacuum conditions.

The *Surface-to-Ambient* condition covers the heat losses over the regolith surface or the crucible insulation, respectively. The surface emissivity value for the lunar regolith ε_r was chosen according to McCloy et al. (2011), who experimentally investigated emissivity fits for different lunar simulants. For this study, the fitted equation of JSC-1AF dependent on the surface temperature was chosen, which is in the range of approximately 0.72 at 300 K up to 0.95 at 600 K. Other constant values for regolith emissivity can be found e.g. in Salisbury et al. (1997) or Wasilewski (2021a), ranging similar from 0.7 to 0.93. In general, due to neglecting the modeling of the dome (see section 5.1.2, the loss to the environment is rather conservative for in-situ extraction since the temperature would dynamically increase under the dome during the outgassing and capturing of vapor (assuming the dome is insulated and enough vapor to outgas).

On the other hand, for the crucible, it was assumed that the heater could be installed inside the chamber walls. Thus, the insulation could be greatly simplified and different insulation methods like e.g. solid insulation, porous insulation, or Multi-Layer Insulation (Hager and Binns 2021) were not further investigated. As a result, the effective emissivity of the crucible ε_c walls estimated to be 0.1 (Kiewiet et al. 2022). The *Open Boundary* condition accounts for open heat transfer via the respective boundaries, so the design space is not limited.

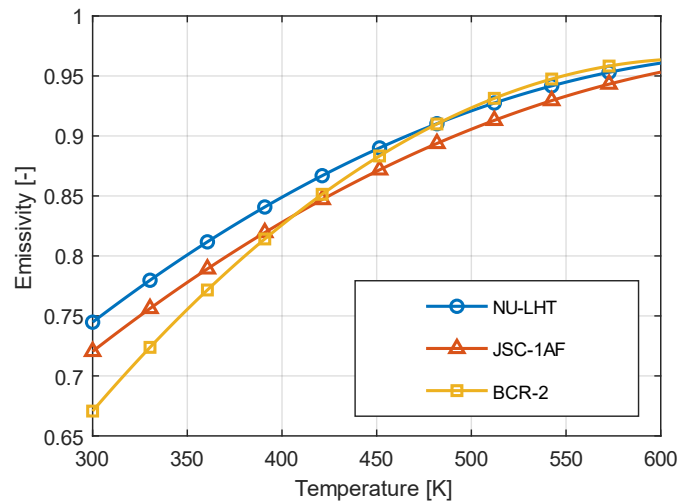


Figure 5-3: Comparison of surface emissivity fits for different lunar regolith simulants (based on McCloy et al. (2011))

Table 5-4: Description of top-level boundary and initial conditions

Description	Boundary condition	Values
Heating	$-n \cdot q = q_0$	$q = 683; 1366; 2732; [W/m^2]$
Surface-to-Ambient-Radiation	$-n \cdot q = \varepsilon_{(c)} \sigma (T_{amb}^4 - T^4)$	Regolith surface emissivity (1) & (2) [a] $\varepsilon_r = -1.5 \cdot 10^{-6} T^2 + 2.216 \cdot 10^{-3} T + 0.024$ Insulated crucible surface emissivity (3) $\varepsilon_c = 0.1$
Open Boundary	$T = T_{amb}, for n \cdot u < 0$ $-n \cdot q = 0, for n \cdot u \geq 0$	$T_{amb} = 40 K [b]$
Symmetry	N/A	
Initialization Condition	$T = T_{amb}$ $p = p_{amb}$	$T_{amb} = 40 K$ $p_{amb} = 3 \cdot 10^{-10} Pa [c]$

[a] (McCloy et al. 2011)
 [b] (Williams et al. 2019)
 [c] (Heiken et al. 1991)

5.1.4 Mesh and Solver Setup

To verify the simulation results concerning their spatial and temporal discretization, several preliminary studies were performed. First, a mesh refinement study was conducted to determine an adequately refined mesh generating reliable results, while still taking computational effort into account. Additionally, step sizes and the relative tolerance were adjusted accordingly. Furthermore, other solver settings like the solver method and termination had to be adjusted to guarantee a stable convergence.

Mesh Refinement

The mesh serves two purposes: First, it is used to approximate the geometry, and second, the approximate solution to the problem is solved at discrete points in space defined by this mesh. To gain confidence in the accuracy of the model, it must be

resolved on progressively finer meshes and results must be compared. In practice, there is a limit to how much mesh refinement can be done before the computational resources are exceeded. Thus, an optimum between computational performance and solution accuracy must be determined.

Due to the change in geometry and heated surfaces, and thus the change of areas of special interest, the mesh had to be adapted for each design (1) - (3) individually. To parametrize the mesh, multiple COMSOL native mesh parameters can be varied, depending on what mesh generators are chosen, and if the mesh is free/unstructured or structured. In the case of the former, especially the maximum mesh size m_{max} of a single element and the maximum element growth rate m_{grow} are potent parameters to investigate the mesh density and subsequently the number of elements. When choosing a structured mesh, besides mesh size m_{max} , also the number of elements m_n and the element ration m_r are important to specify the distribution of mesh elements along an edge or sweep direction. For both in-situ methods (1) and (2), free triangular/tetrahedral mesh elements were chosen, whereas due to the uniform lateral heated boundary for the heating chamber (3), a structured quadrilateral mesh could be applied. To be consistent in terms of mesh refinement over all designs regarding a mesh density indicator, the overall number of elements was selected.

To measure the impact of the parameters described priorly and thus the mesh density regarding the solution accuracy of the average temperature, an initial mesh first had to be implemented for each method which served as a reference. The initial mesh was built as coarse as possible, yet to still ensure convergence of residual error to $10^{-4} K$. Starting from that, the mesh density was iteratively refined by a factor of approx. 1.5 for the 2D models and by a factor of ~ 3.6 for the 3D mesh, and solutions compared to the respective last study. This was repeated until the mean squared error \bar{e}_T was less than 10^{-3} to confirm mesh independence. The latter can be calculated as

$$\bar{e}_T = \frac{1}{N_t N_p} \sum_{i=1}^{N_t} \sum_{j=1}^{N_p} \left(\frac{T_{n+1}^j(t_i) - T_n^j(t_j)}{T_n^j(t_i)} \right)^2 \quad (5-1)$$

with the total number of evaluated timesteps N_t , the total number of compared data points N_p , the i^{th} timestep t_i , the j^{th} data point of the respective variable $(\cdot)_j$, and the iterative refinement step $(\cdot)_n$.

Setting up the mesh for design (1), originally a uniform structured quadrilateral mesh was chosen. Yet, while starting to investigate its convergence, it soon became apparent that the phase change requires a very high spatial resolution. Subsequently, a much denser mesh distribution was chosen at the heated surface boundary under the dome to be able to solve for high gradients and free triangular elements were used to. The results are shown in Figure 5-4 and Figure 5-5. In total, 6 simulations were needed to reach a nearly independent mesh with a mean square error $\bar{e}_T = 4.1 \cdot 10^{-3}$. The final mesh consists of 4761 elements with a global maximum element size $m_{max} = 0.1m$ and growth factor of $m_{growth} = 1.1$, as well as $m_{max} = 0.005m$ and $m_{growth} = 1.2$ at the heated boundary.

It may be noted that the presented total number of elements was only valid for the baseline scenario with a total power input of $Q = 1.5 kW$ and a power flux of $q = 1 sol$ because of the diameter dependency of those variables (see chapter 5.1.3). Yet, since

the mesh generation and sizing parameters were manually hardcoded, the single element size and growth rate could be held stable during the parameter study.

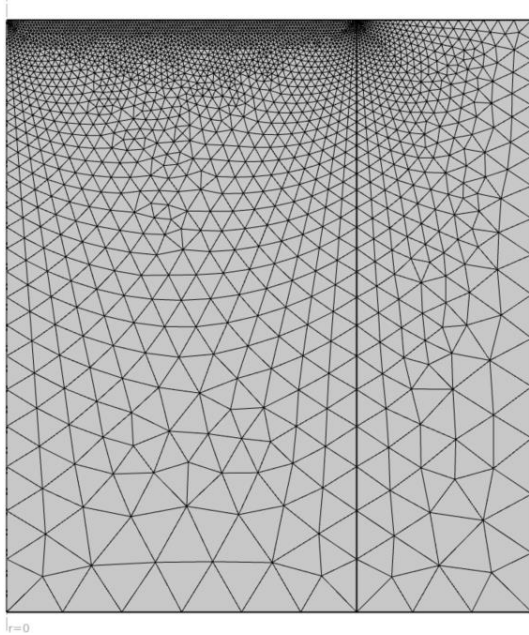


Figure 5-4: Visualization of the mesh used for the baseline in-situ surface heating

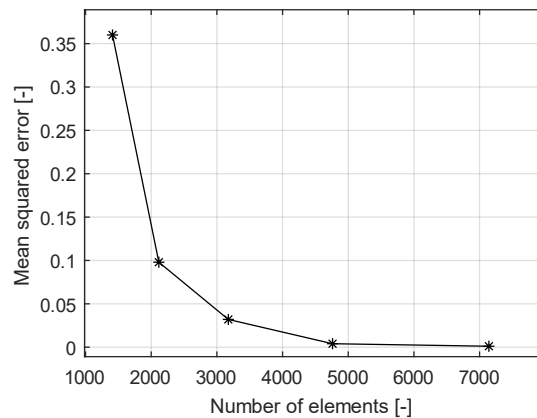


Figure 5-5: Solution accuracy progression of the average temperature during the mesh refinement study for the baseline in-situ surface heating

Due to the insertion of the rods into the regolith for the heating (2), the geometry could not be simplified to an axisymmetric model. Even though the model could still be partly reduced, this still had substantial implication on the computational cost. In comparison to the 2D-model of the surface heating growth (1), for the same mesh size, the computation time increased by a factor of ~ 16 . Thus, for this model, a slightly bigger mean square error of $\sim 1 \cdot 10^{-1}$ was deemed to be acceptable, since a further improvement of the mesh would have not been reasonable in terms of computational cost. The final mesh displayed in Figure 5-6 consists of a total of 153.316 elements and has a mean square error $\bar{e}_T = 3.5 \cdot 10^{-2}$ to the prior refinement iteration after 5 simulations. The mesh was solely built by tetrahedral elements to adequately resolve the more complex geometry. The maximum element size of the heated boundary is $m_{max} = 0.02 \text{ m}$ with a maximum growth rate $g_{grow} = 1.1$. The same rate was applied to the regolith domain under the dome, thus the inner geometry circle, yet $m_{max} = 0.1 \text{ m}$. For the outer domain, no big gradients were observed, so the maximum element size was set to $m_{max} = 0.2 \text{ m}$, and $g_{grow} = 1.5$.

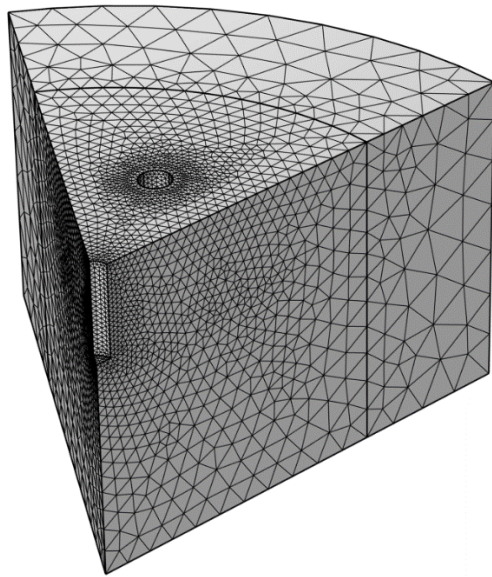


Figure 5-6: Visualization of the mesh used for the in-situ rod heating

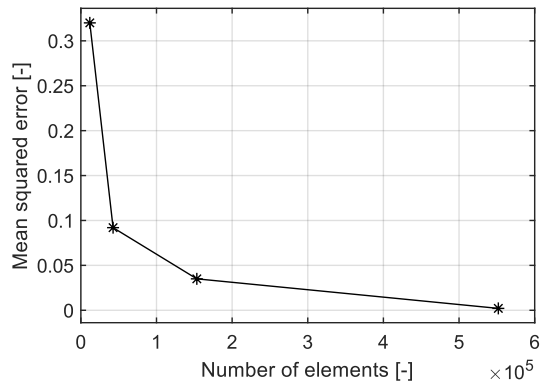


Figure 5-7: Solution accuracy progression of the average temperature during the mesh refinement study for the in-situ rod heating

In contrast to models (1) and (2), due to very simple geometry and constant heating being applied over the whole lateral surface, the heated chamber model (3) could be parameterized via a structured quadrilateral mesh. The final mesh can be seen in Figure 5-8, consisting of 1.980 quads and 2.077 vertices. Since the first studies showed, that phase change can happen over the whole domain, the average mesh element size had to be smaller. The latter was determined via a distribution node, specifying the number of elements m_n over an edge as well as an element ratio m_r between the first and last element of the distribution. While for the lateral edges a fixed number of elements $m_n = 50$ was set, supported by a boundary layer, for the upper and lower boundaries the element quantity was set to $m_n = 30$ and the ratio to $m_n = 10$ for the final mesh. The latter was determined after iterating the refinement steps 5 times, resulting in a mean squared error of $\bar{e}_T = 3.8 \cdot 10^{-3}$.

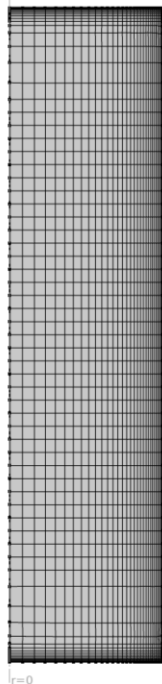


Figure 5-8: Visualization of the mesh used for the heating inside a crucible

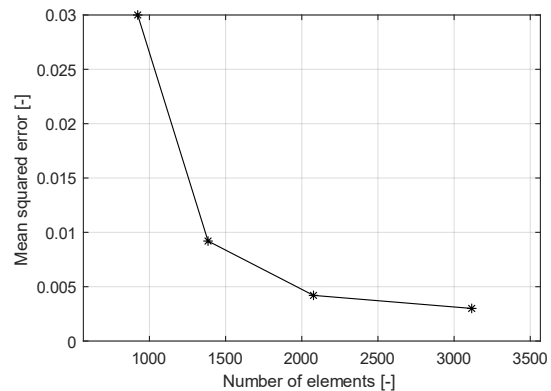


Figure 5-9: Solution accuracy progression during the mesh refinement study for the heating inside a crucible

Besides the mesh resolution, also the mesh element quality is an important aspect to consider when validating a model. While low mesh resolution, about the variations in the solution and the geometry, can lead to inaccurate results, a low mesh element quality, which measures the regularity of the mesh elements' shapes, can lead to inverted mesh elements and high condition numbers for the Jacobians, which in turn can cause convergence issues. (COMSOL Documentation 2021)

Mesh quality measures in COMSOL include *Skewness*, *Maximum angle*, *Volume versus circumradius*, *Volume vs length*, *Condition number*, *Growth rate*, or *Custom expressions*. For all quality measures, a quality of 1 is the best possible and it indicates an optimal element in the chosen quality measure. At the other end of the interval, 0 represents a degenerated element.

While there are no absolute numbers to present for what the quality should be, as the physics and solvers used will have different requirements on the quality needed, Gothäll (2022) is suggesting that in general, elements with a quality below 0.1 are considered poor quality for many applications. Figure 5-10 displays exemplary skewness for each extraction method (1) – (3).

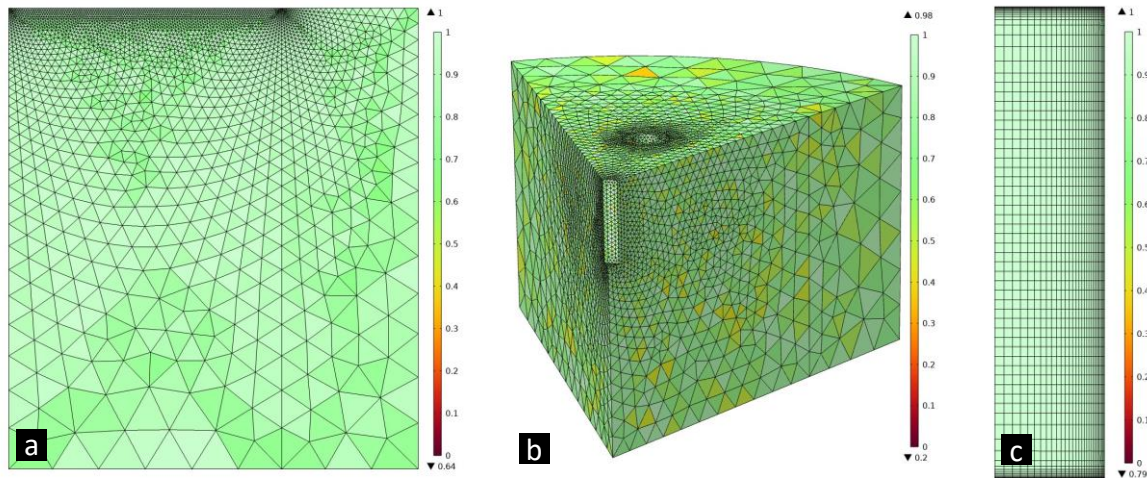


Figure 5-10: Quality of the Skewness of the mesh elements for the respective extraction models: a) in-situ surface heating, b) in-situ rod heating, c) crucible heating

Step Size Study

The framework of the time-dependent simulation was set to be ~ 14 days, representing a lunar sun cycle (see chapter 3.3). Yet, preliminary simulation results indicated possible interesting behavior still after that duration, thus a total period of $1.5 \cdot 10^6 s$ was investigated ($\sim 17,36$ days), which also might be possible to reach with solar energy on the poles due to peaks of eternal light.

Like in the mesh study, to verify the stability of the solver, the implications of varying timestep sizes must be examined. Most time-dependent problems in *COMSOL Multiphysics* are by default solved with an adaptive time-stepping scheme. This means, that, the solver always chooses the next timestep based on the convergence and the residual of the computation of the previous timestep and the timestep size will be automatically adjusted to the desired relative tolerance. Lowering the relative tolerance to smaller numbers will result in smaller timesteps, which increases solution accuracy, and solving time. Yet, if the wanted output time does not match with the time chosen by the solver, which often is the case, the output then can be determined through interpolation. For that, limiting the maximum timestep size is a typical strategy since this interpolation could potentially obscure some impacts of the dynamic system from the output. (Smolka 2021)

Thus, again the mean squared error according to equation (5—2) was calculated for the average sample temperature. Initially, a maximum step size of $\Delta t_{max} = 2 \cdot 10^4 s$ was chosen. Yet, this did not resolve initial high temperature gradients sufficiently. By further adjusting the overall maximum step size to $\Delta t_{max} = 1 \cdot 10^4 s$, it could be observed that the requirement of a temporal resolution was very dynamic during the study. Thus, for the first $1 \cdot 10^5 s$ the maximum timestep was reduced to $\Delta t_{max} = 5 \cdot 10^3 s$ ensure numerical stability, especially during high sublimation phases, and simultaneously reduce computational time during periods near steady-state that did not require fine temporal resolution. After $1 \cdot 10^5 s$, the step size could even be further increased to $\Delta t_{max} = 2 \cdot 10^4 s$ without reducing the solution accuracy.

5.1.5 Performance Metric

To be able to quantify the generated results, a performance metric must be set. For each extraction method individually, the total water yield generated is a valid evaluation criterion. Yet, due to the major differences between the models invoked by design constraints like in the system size, relative evaluation values are needed as well. Hence, three main quantitative evaluation criteria are selected to measure the performance of the designs: the total water yield m_{yield} [kg], the average extraction rate r_{yield} [kg/h], and the energy efficiency η [kg/kW · h].

The total sublimated water yield over time was determined to characterize the performance of the extraction method. This was achieved by integration the phase change indicator of the second phase θ_2 (see chapter over the respective volume of the sample and multiplying it by the initial bulk density of the ice within the regolith $\rho_{i,b}$:

$$m_{sub}(t) = \int_V \theta_2 dV \cdot \rho_{i,b} \quad (5-2)$$

$m_{sub}(t)$ was at the same time assumed to be rapidly condensed and captured outside of the sample.

Since the main parameter study does not account for mass transfer on a molecular level, water losses during the extraction process due to e.g. redeposition of the vapor or leaks in the closed system like at the edges of the heated dome on the regolith surface for the in-situ methods had to be assumed. The loss factor of the latter is suspected by other scholars to be up to 10 % (Sowers and Dreyer 2019), while the percentage of redeposition of the vapor within the soil is highly dependent on applied heating methods and overall extraction time (Song et al. 2021; Schieber et al. 2022). In a preliminary simplified study investigating the outgassing and redeposition of water vapor for in-situ surface heating, an average loss value of ~10% was determined. In further accordance with Kornuta et al. (2019) and Kiewiet et al. (2022), a total loss value of 20 % was applied to the extracted water mass $m_{yield}(t)$ compared to $m_{sub}(t)$ for the in-situ methods (1) and (2). For the excavated method (3), initial results showed the extraction rate to be quite high, and with an additional completely closed system this loss value was not applied. Further losses are expected during the water vapor capture and refreezing. The modeling of an eg. cold-capture sub-subsystem yet has also to be examined in future as possible rates of vapor cold capture are still unknown (Schieber et al. 2022).

The average sublimation rate and subsequently extraction rate was determined by time derivate of $m_{sub}(t)$ and $m_{yield}(t)$, respectively, resulting in $r_{sub} = \frac{\partial m_{sub}(t)}{\partial t}$ and $r_{yield} = \frac{\partial m_{yield}(t)}{\partial t}$.

The depth of sublimation, meaning the phase change interphase distance from the heated surface, can be calculated as:

$$r_1(t) = \overline{\theta_2} \cdot h \quad (5-3)$$

for the in-situ surface heating, with $\overline{\theta_2}$ being the volume averaged desiccated phase indicator and h being the sample height, and

$$r_2(t) = \theta_2 \cdot r_{sample} \quad (5-4)$$

for the excavated system, with r_{sample} being the sample radius. For the in-situ rod heating, the interphase distance was not considered.

Besides the sublimation interphase depth, also its velocity or acceleration can be investigated to look at how fast the sublimation progresses in certain cells or at certain points in time. This can be simply done through evaluation of the derivatives of equations (5—3) and (5—4), respectively: velocity $v = \frac{\partial r_{1,2}}{\partial t}$ and acceleration $a = \frac{\partial^2 r_{1,2}}{\partial t^2}$.

During the process of the thermal water ice extraction, also the energy efficiency η can be investigated, which is defined as the ratio of the total water yield m_{yield} [kg] to the total energy power input P [W] over the simulated time t_{sim} [h]:

$$\eta = \frac{m_{yield}}{P \cdot t_{sim}} \quad (5—5)$$

5.2 Design Optimization

Prior simulation approaches of thermal water extraction on the Moon concluded the low thermal conductivity of the lunar regolith to be the main factor for sublimation lag build-up, hindering further extraction after an initial upper soil layer is dried out (for surface heating) (Wasilewski 2021b). Without additional methods to mitigate this problem, the extraction rate will approach negligible amounts after reaching a thermal equilibrium between the power input and the energy lost over the surface.

In the case of the in-situ methods (1) and (2), it is therefore essential to determine an optimal heating time of the soil to increase extraction efficiency. After this time is reached and the mined area is desiccated, the whole extraction system can be moved with the help of a rover to a fresh location to mine a new “batch”. The optimum heating time is calculated in consideration of the time and energy required for the relocation.

The same principle applies to heating the regolith inside a crucible after excavating it first (3). Depending on the power available to heat the soil inside the chamber, as well as the overall geometry of the chamber, extraction rates were expected to decrease after the initial first production phase. Also, it is possible for the batch inside the crucible to completely desiccate. In contrast to the in-situ methods, the dried regolith has then to be dumped and refilled with another icy batch to be able to continue the water mining process. Thus, in addition to the time and energy needed to relocate, also the time and energy needed for the regolith excavation process and the filling and dumping of the crucible needs to be considered.

A tool optimizing the heating time for both in-situ surface heating (1) and crucible heating (3) was initially developed by Franco Marchese (Kiewiet et al. 2022). By gradually adapting the optimization algorithm to the changes requirements of the specific simulations, the results of the latter (total water yield, average extraction rate, average energy efficiency) could thus be fed into the algorithm and used to calculate optimal cycle times for each simulation (heating time before relocation (for (1) and (2)), or dumping and refilling (in case of (3))).

A flowchart of the design optimization process can be seen in Figure 5-11. A more detailed description of the functionality can be found in Kiewiet et al. (2022).

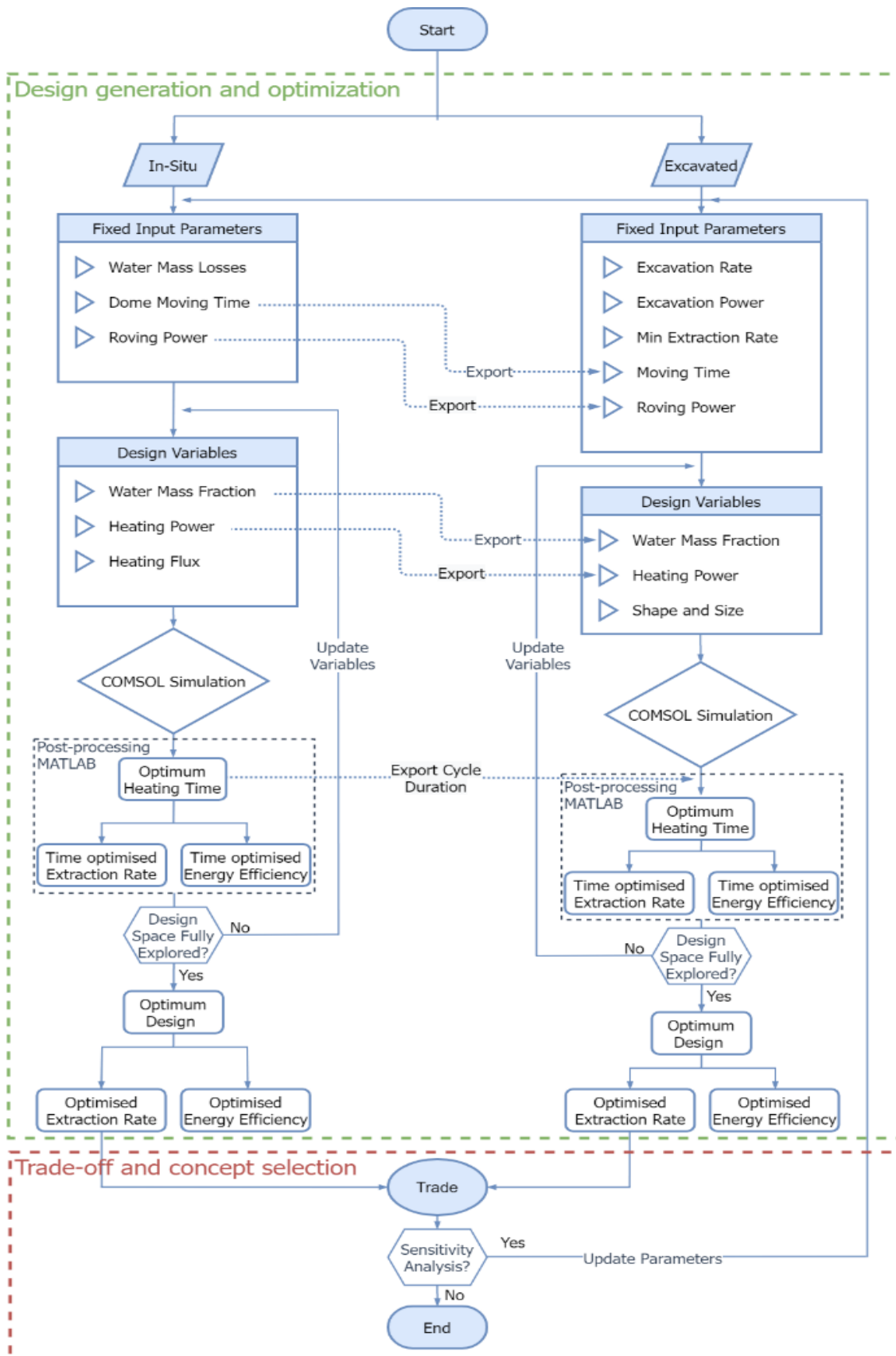


Figure 5-11: Flowchart of the Design Optimization Process (Kiewiet et al. 2022)

6 Results and Discussion

This chapter provides the results of the parameter study introduced in chapter 5.1. The results presented also will be interpreted and discussed. Furthermore, the respective extraction methods (1) - (3) will be compared to each other regarding their performance concerning both the quantitative results as well as qualitative factors introduced in chapter 3.3. In the end, a recommendation on the application of the presented methods will be provided before the work is critically reflected and the limitations of the models and simulations are presented. Additionally, given the high uncertainty in thermophysical lunar regolith properties due to missing ground truth data, an investigation of other crucial input parameters like the thermal conductivity or the phase change temperature is conducted. This also includes the analysis of the different use cases.

6.1 Design Parameter Study

The main parameter study investigates the results of variations in the initial water content w_i , the total power input Q and the power density q (see chapter 5.1) on the total water yield extracted and the extraction rate progression in the given time of ~17,5 days for each respective method (1) – (3). Furthermore, the heat distribution within the regolith will be presented and its implications discussed.

6.1.1 In-Situ Surface Heating

An exemplary temperature distribution and phase change indication for the baseline configuration within the icy regolith domain after the simulated timeframe of $1.5 \cdot 10^6$ s can be seen in Figure 6-1 and Figure 6-2, respectively. For $w_i = 5$ wt. %, $Q = 1500$ W and $q = 1$ sol, a maximal temperature of ~ 407 K is reached at the heated surface. While this temperature range is approached rather quickly during the simulation on the regolith surface, it does not surpass this value. This is due to the surface losses of energy to the ambient, which approaches equilibrium with the heat flux put into the regolith. It also becomes apparent that the highest temperature gradients are present within the top 5 cm of the soil, indicating poor thermal conductivity. This will be investigated further in the following. The highest temperature during the parameter study for this design was observed to be ~ 472 K for a power density of $q = 2$ sol and water content of $w_i = 1$ wt. %.

C_i=0.05, Q_{heat}=1500, sol=1366 Time=1.5E6 s Surface: Temperature (K)

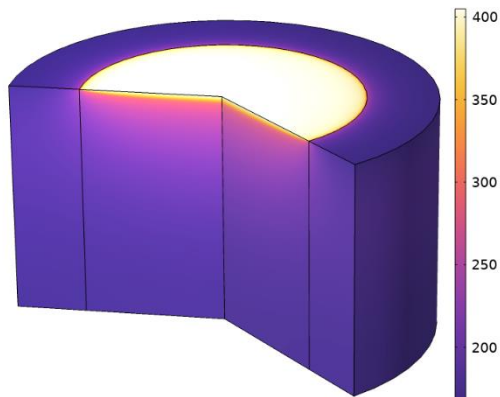


Figure 6-1: Exemplary temperature distribution after ~17,5 days for in-situ surface heating for the baseline configuration

C_i=0.05, Q_{heat}=1500, sol=1366 Time=1.5E6 s Surface: Phase

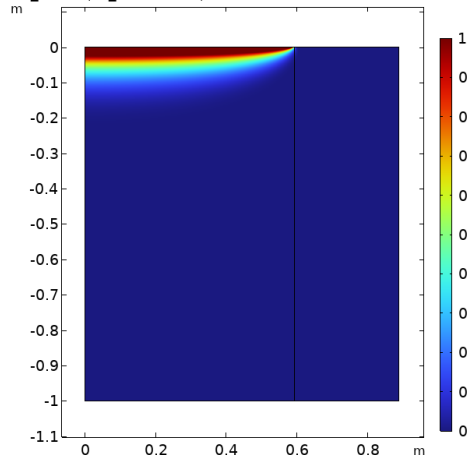


Figure 6-2: Desiccated volume after ~17,5 days for in-situ surface heating for the baseline configuration (1: fully desiccated; 0: fully icy)

Table 6-1 displays the volume averaged sublimation front depth and total water yield reached by (1). It becomes apparent, that for a fixed water content w_i , a higher power input Q and power density q directly imply a deeper reach of the sublimation front. Yet, investigating the implications of w_i on the overall depth, results are indifferent with the highest reach being present for 1 wt.% water content (up to 10,5 cm), and an initial situation of 15 wt.% (up to 7,33 cm) outperforming 5 wt.% (up to 7,70 cm) after the simulated time of $1.5 \cdot 10^6 \text{ s} \approx 17,5 \text{ days}$. This can be explained with the increasing latent heat for higher water wt.% and the change of thermophysical properties of the regolith (higher specific heat and thermal conductivity for icy regolith). This will be discussed further in the following. Yet, the same applies to the total water yield generated, yet the differences in the system size play a more decisive role, resulting in a smaller q leads to a bigger total yield. (The correlation between the power input and the power density with the system size can be seen in Table 5-3.)

Figure 6-3 displays the results of the total water yield progression generated by the in-situ surface heating method after ~17,5 days for 1 wt.%, 5 wt.%, and 15 wt.% respectively. The different colors and line styles of the graphs shown represent the parameter sweeps over both the power input Q and power density q .

Table 6-1: Volume averaged depth and total water yield reached by the in-situ surface heating design after ~17.5 days

Water content [wt. %]	Power [W]	Power Density [W/m ²]					
		683	1366	2732	683	1366	2732
		Average depth [cm]			Total water yield [kg]		
1	500	3,26	5,21	7,81	0,27	0,21	0,16
	1500	4,06	6,54	9,57	1,00	0,80	0,59
	2500	4,43	7,18	10,5	1,81	1,47	1,08
5	500	2,99	3,91	5,36	1,23	0,80	0,55
	1500	3,69	4,69	6,12	4,53	2,88	1,90
	2500	4,06	5,12	6,70	8,33	5,24	3,43
15	500	4,37	5,75	7,18	5,37	3,54	2,21
	1500	5,02	6,04	7,18	18,52	11,13	6,62
	2500	5,43	6,29	7,33	33,42	19,35	11,26

Comparing the respective plots of Figure 6-3, it can be seen that for constant Q and q , the highest water yield can be achieved for the highest wt.% of water ice initially being inside the regolith.

Furthermore, for a constant power density q , the total power available directly corresponds to the water yield, being the highest for 2500 W and the lowest for 500 W, also independent of the initial water content w_i , as expected. Investigating the impact of the power density q , it becomes apparent that the lowest flux always generates the biggest water yield and outperforms the higher heat flux systems. This can be explained due to the dependency of the dome size and thus the regolith volume on the power density q . An overview of that correlation can be found in Table 5-3. Thus, with a bigger system size, there is simply more water ice available to extract. Yet, it takes much longer for the lower heat fluxes to reach sublimation temperature within the regolith and initiate the water extraction process. This effect gets more dominant with higher water percentages and can be observed best in Figure 6-3c. This is further illustrated in Figure 6-4, which displays the extraction rate dependency of the initial water content and the power density. This indicates that the area mined and thus the system size is more influential on the extraction than the power put into the regolith, as long as there is at least $q_{min} = 0.5 \text{ sol}$ available. While for 1 wt.% initial water ice content, the graphs representing the different total power inputs in unique colors are separated, they start to cross over another for higher wt.% of water ice, further underlining the importance of the system size.

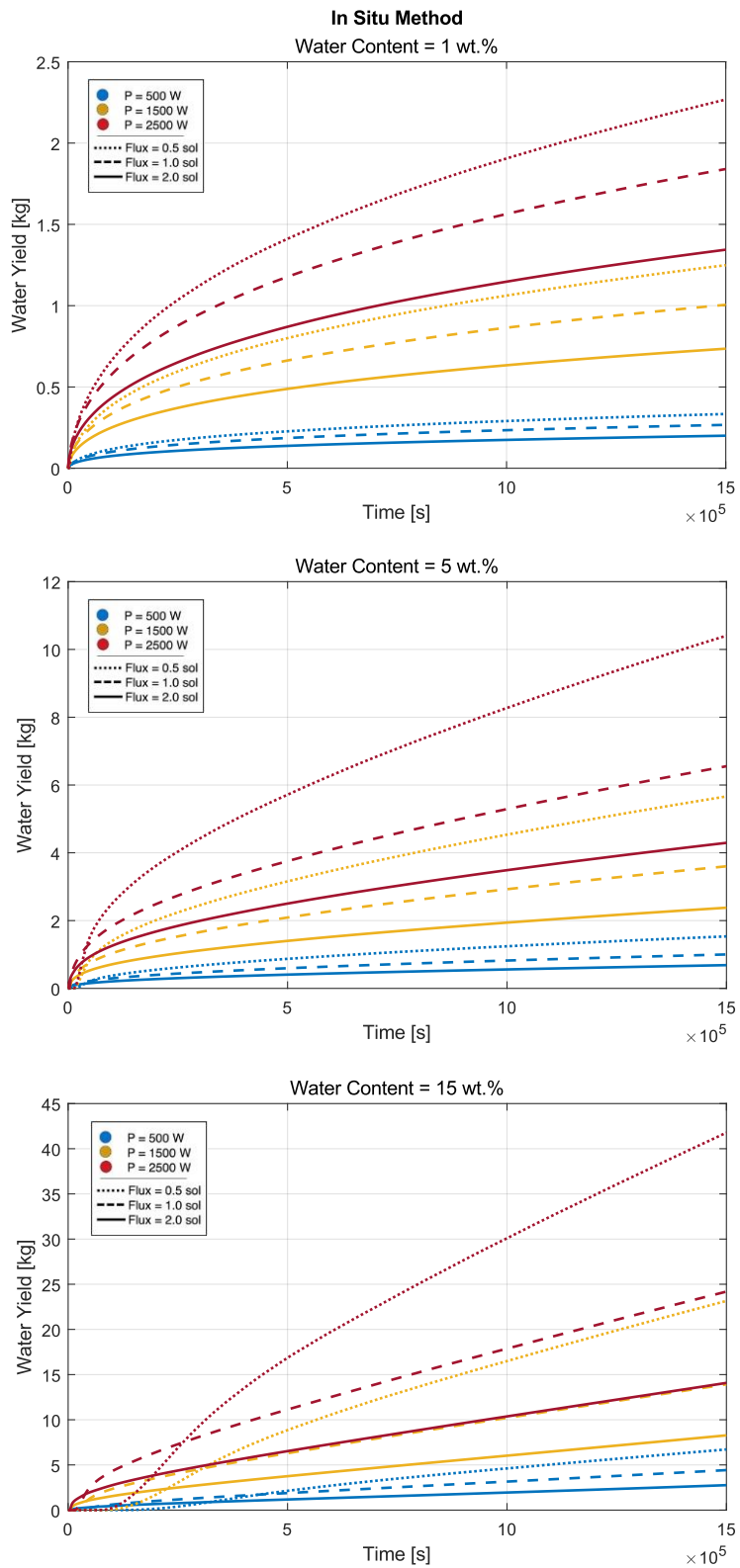


Figure 6-3: Total time-dependent water yield for in-situ surface heating with varying water contents

The delay in the initialization of the sublimation process can be explained by the change of thermophysical properties of the regolith with the variation of the water ice content w_i . This not only has major implications on crucial parameters like the thermal conductivity or the specific heat capacity of the icy regolith but also on the latent heat necessary to sublimate the ice. Thus, more water ice content within the regolith subsequently implies higher energy to be needed for the phase change. This behavior is even intensified by the reduced thermal conductivity of the uppermost dried regolith, which reaches higher temperatures for higher power densities and increases the radiative surface energy losses by a factor $\propto T^4$ (see Table 5-4). Additionally, also the surface emissivity value for regolith scales with the temperature, resulting in higher losses for higher temperatures, which is also presented in Figure 5-3.

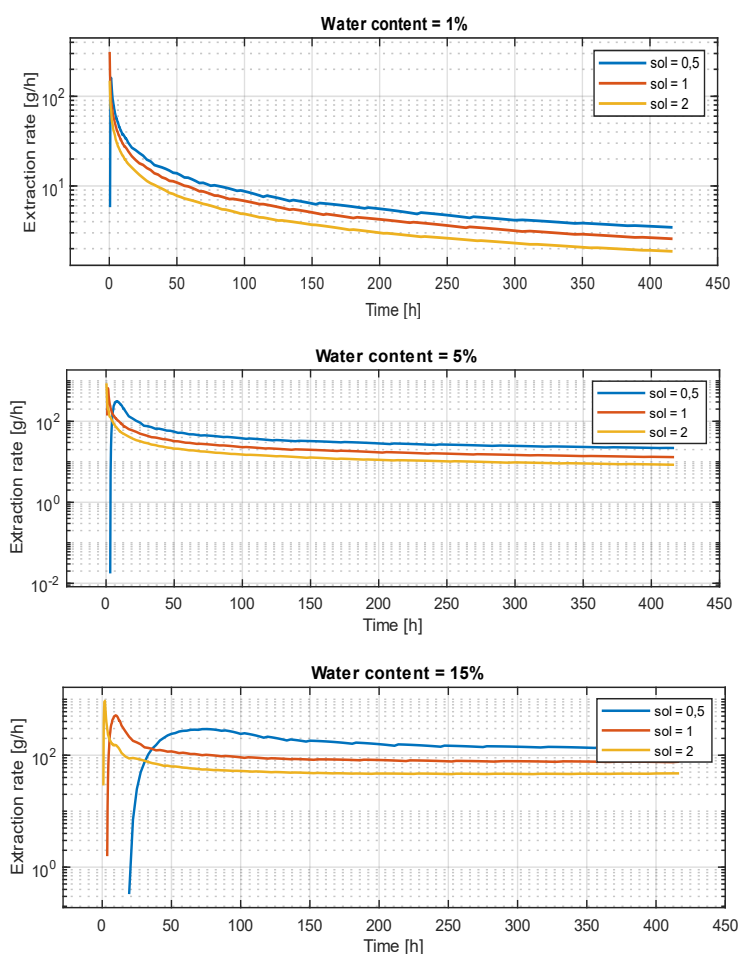


Figure 6-4: Water ice content and power density influence on the extraction rate for in-situ surface heating for a Power input of 1500 W

Investigating the extraction rate of the surface heating method, it can be seen that it is decreasing drastically for each configuration after an initial high rate, for some configurations even reaching negligible values, with exception of high total power inputs but low fluxes (see Figure 6-4). This phenomenon was also already addressed by Wasilewski (2021b). The lag in the phase change rate is mainly due to the very poor thermal properties of the desiccated lunar regolith, which builds up at the top during the extraction process and acts as a thermal insulator, impeding heat transfer to deeper layers of the soil. Since this is one major limitation of the surface heating method, a

possibility to mitigate this problem and optimize the design is by relocating the heating system and vapor-capturing tent to a new location after the initial production phase is over (see chapter 5.2). The results of the latter and its implication on the water yield are presented and discussed in chapter 6.2.1.

Yet, there are also other possibilities to alleviate the observed sublimation lag for surface heating to increase the generated yield. Wasilewski (2021b) further suggests either compacting the dry layer or inducing a thermal conductivity-enhancing gas into the pores of the soil to improve its thermal properties, or excavating the desiccated regolith layer either mechanically or pneumatically. The removal of that thin and dry layer would not drastically raise energy requirements, since hot desiccated regolith is much easier to excavate than icy solid regolith yet would increase system complexity (Atkinson et al. 2019).

6.1.2 In-Situ Rod Heating

The results displaying the total water yield extracted for the iterated in-situ method with heated and soil-implanted rods can be seen in Table 6-2 and are further plotted over the investigated timeframe in Figure 6-5. It must be noted, that for these methods there are no changes in the system size compared to the baseline geometry of the sole in-situ surface heating (1), and both the dome diameter as well as rod size, quantity, and distribution pattern have been fixed. Thus, the power density levels q were directly implied by the total surface area of the heated rods, resulting in $q_{Q=0.5 \text{ kW}} = 699 \text{ W/m}^2$, $q_{Q=1.5 \text{ kW}} = 2099 \text{ W/m}^2$, and $q_{Q=2.5 \text{ kW}} = 3498 \text{ W/m}^2$. The most striking aspect is the rather constant extraction rate for each variation of the initial water content w_i and the total power input Q . Because of that, the total water yield generated is also constantly rising and a decline in the sublimation rate is only barely seen.

Table 6-2: Total water yield reached by the in-situ rod heating method after ~ 17,5 days

Water content [wt. %]	1			5			15		
Power [W]	500	1500	2500	500	1500	2500	500	1500	2500
Total water yield [kg]	6,59	15,63	22,41	8,86	48,64	76,76	0,13	72,34	134,89

As expected for this method, due to the fixed system size, independent of the initial water content w_i , the biggest power input Q respectively generates the highest water yields during the simulated time of ~ 17,5 days, and vice versa. Yet, the range of the total yield generated is the biggest for $w_i = 15 \text{ wt. \%}$, while the generated yields for $w_i = 1 \text{ wt. \%}$ only differ comparably little. As already described, the changes in thermophysical properties of the lunar regolith are considerable, whether ice is incorporated, or the soil is desiccated. Not only does the energy required for the phase change increase with a rising water ice content, but also does the specific heat capacity of the ice-regolith mixture. This can be especially observed for $Q = 500 \text{ W}$ and $w_i = 15 \text{ wt. \%}$, for which the sublimation temperature is only barely reached. This also indicates that a higher power density is needed to reach sublimation for an increasing water content compared to (1). Even though no initial sublimated lag can be identified, the time threshold to reach sublimation is longer.

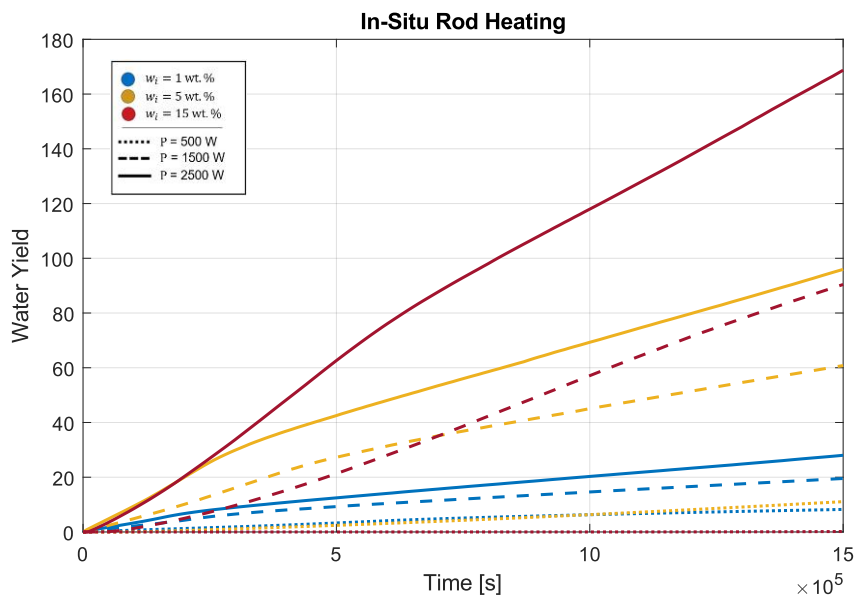


Figure 6-5: Total time-dependent water yield for in-situ rod heating

Investigating the temperature distribution throughout the whole sample (see Figure 6-6), it is noticeable that the surface temperature of the soil is much cooler than in the subsurface, hence reducing radiation losses to the environment. Furthermore, since the rods are incorporated into the soil the sublimation front progresses in all three dimensions in a sphere-like shape. Thus, the surface area of the sublimation front increases by the factor $\propto x^2$ and the volume of the regolith, which needs to be desiccated even by a factor $\propto x^3$, with x being the distance from the heated surface. This must be counteracted by the rod distribution and spacing to facilitate and equal heat transfer within the sample. Figure 6-6 yet also shows, that through the application of the rods the system can overcome the limitations of (1) and distribute the heat in deeper soil levels. independent from the water content, both the specific heat capacity and thermal conductivity of the regolith are a function of the temperature (see chapter 4.1), with both values increasing for higher soil temperatures. As seen in Figure 6-6, the temperatures being apparent in the soil layers around the heated rods reach comparable high numbers, due to the surrounding regolith layers acting as a thermal insulator minimizing energy losses. Given enough time and power to surpass the also increasing heat capacity of the regolith, heat transport in the subsurface is facilitated.

During the study, maximum regolith temperatures of ~ 1300 K near the heated rods were observed, being within sintering ranges. Yet, due to only scratching those values for specific configurations, a second phase change and the subsequent implications on the extracted water yield and energy efficiency were not further investigated in this work. Also, since the number, spacing, radius, and height of the heated rods are a function of the available power, other configurations could be investigated in the future to investigate their impact on the sublimation yield

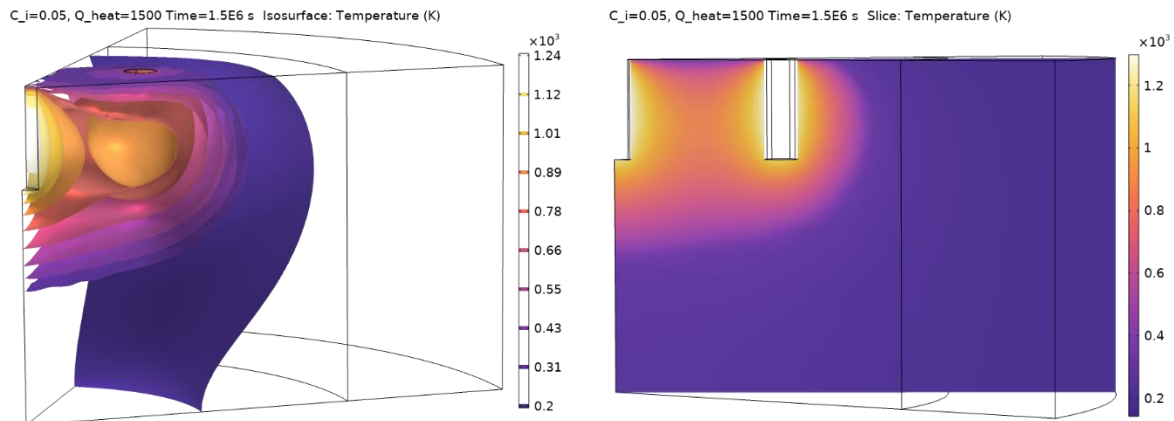


Figure 6-6: Exemplary temperature distribution after ~17,5 days for in-situ surface heating for the baseline configuration (left: 3D contours; right: 2D cross-section through the rod plane)

On the other hand, for the regolith surface layer to even reach sublimation temperature is highly dependent on both the power input and the initial water yield. While a cooler regolith surface temperature mitigates radiation losses to the ambient environment, thermal conditions below the sublimation temperature can prevent the generated water vapor from being able to outgas through the regolith surface. Thus, an additional simulation was conducted, moreover adding the minimum required heat flux for sublimation $q = 0,5 \text{ sol}$ at the top surface to prevent the building of a desiccated “pocket” inside the sample. The results are displayed in Figure 6-7 and show a desiccated volume that is “open” towards the surface, practically permitting a mass flux to be transported out of the regolith.

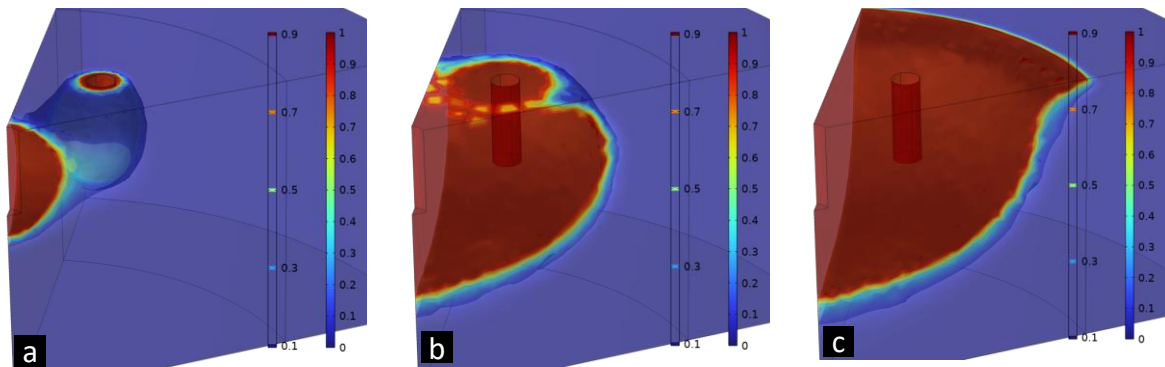


Figure 6-7: Outgassing ability of the water vapor for in-situ rod heating with an initial water content of 5 wt.% (1: fully desiccated; 0: fully icy): a) 500 W power input, b) 1500 W power input, c) 1500 W power input plus additional surface heating

6.1.3 Heating inside a Crucible after Excavation

The last extraction method covers the heating of a regolith sample inside an insulated crucible or heating chamber after it was first excavated. Again, an exemplary temperature distribution within the heating chamber for the baseline scenario can be seen in Figure 6-8. Due to the limited volume of the crucible, an advantageous geometry, and insulated boundaries, the temperature gradient is rather small and high temperatures can also be reached in the crucible center. This can also be seen in

Figure 6-9, showing that over two-thirds of the volume is completely desiccated after the simulated heating time, and the remaining volume is at least partially dried. The asymmetric distribution of both the temperature and subsequently the desiccated volume can be explained by the depth-dependent porosity and density of the regolith, as well as with an open boundary for heat transfer applied on the top surface (see chapters 4.1 and 5.1).

C_j=0.15, Q_{heat}=1500 Time=1.5E6 s Surface: Tei

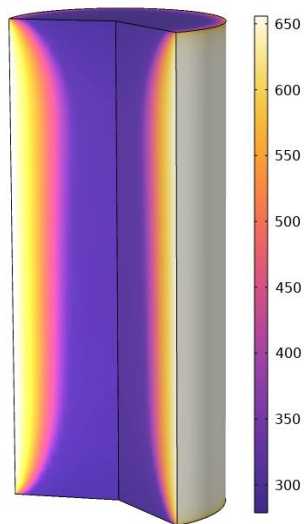


Figure 6-8: Exemplary temperature distribution after ~17,5 days for crucible heating for the baseline configuration

C_j=0.05, Q_{heat}=1500 Time=1.5E6 s Surface: Ph.

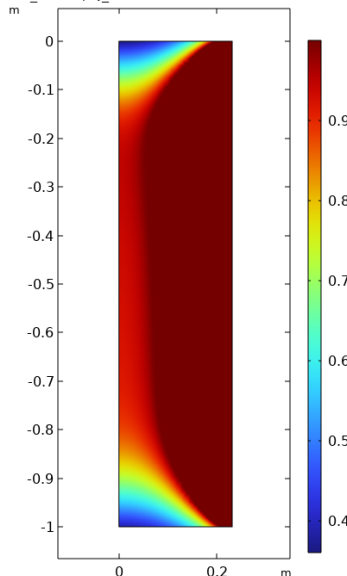


Figure 6-9: Desiccated volume after ~17,5 days for crucible heating for the baseline configuration (1: fully desiccated; 0: fully icy)

The results displaying the total water yield over the simulated time are presented in Figure 6-10, while the absolute values are provided in Table 6-3. It is again to be noted, that the geometry of the crucible was fitted to hold a predefined mass of regolith, and thus having a fixed volume (single dependence on the density of the regolith, which is negligible for the investigated variations of the latter). Similar to (2), the resulting power flux q is thus only a function of the total power input Q . Since only the lateral surface of the cylindrical crucible is heated in this case, the power density results in $q_{Q=0.5 \text{ kW}} = 342 \text{ W/m}^2$, $q_{Q=1.5 \text{ kW}} = 1026 \text{ W/m}^2$, and $q_{Q=2.5 \text{ kW}} = 1710 \text{ W/m}^2$.

Table 6-3: Total water yield reached by the crucible heating method after ~ 17,5 days

Water content [wt. %]	1			5			15		
Power [W]	500	1500	2500	500	1500	2500	500	1500	2500
Total water yield [kg]	2,44	2,47	2,47	11,80	11,90	11,90	32,39	32,58	32,60

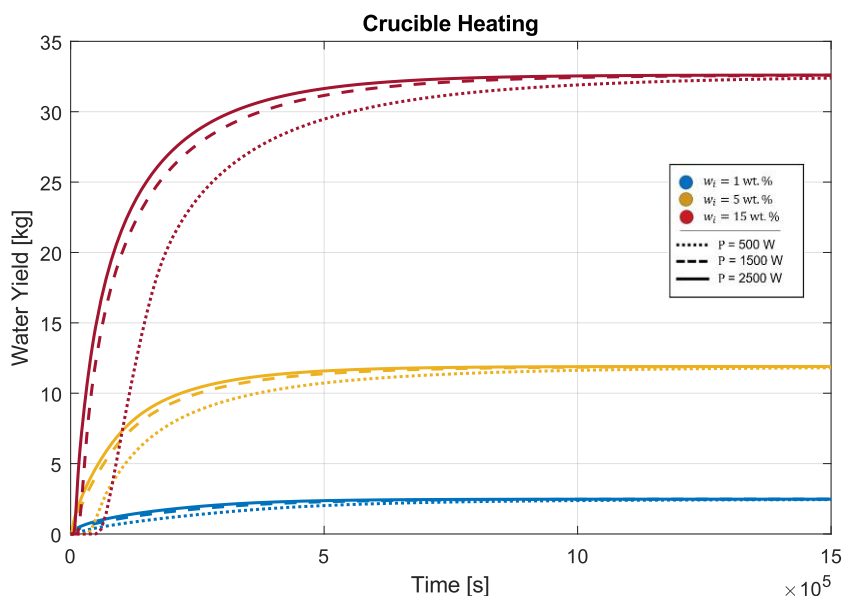


Figure 6-10: Total time-dependent water yield for heating inside a crucible after regolith excavation

Comparable to (1), for constant water content, the higher heating power configurations always display an earlier start of sublimation and a higher extraction rate during the beginning of the simulation. The initial sublimation lag is also increasing together with the water content, resulting in multiple crossovers between different water percentages. Yet, after the initial transient phase in which the crossover takes place, the water yield lines for the respective power levels reach nearly the same asymptote, and extraction rates get aligned.

Being a completely closed and insulated system, losses are expected to be much lower for this method. For the chosen volume, the effective heated surface over the regolith volume is much higher, with heating being applied at the cylindrical crucible mantle around the whole sample. This not only enables the design to heat the very cold regolith much faster initially but the interphase surface after the first sublimation is further reduced by a factor of a factor $\propto x^2$ and the volume of the regolith, which needs to be desiccated even by a factor $\propto x^3$, with x being the distance from the heated surface, being the exact opposite of (2). Furthermore, the completely closed system allows for resublimation and collection of water vapor, after it may have deposited.

6.2 Method Comparison

In this chapter, the investigated water extraction methods (1) – (3) will be compared with both the quantitative results displayed in section 6.1 as well as the qualitative aspects introduced in chapter 3.3.

6.2.1 Quantitative Comparison

Especially for (1) and (3), the results revealed a heavy time dependency on the water extraction rate. For power inputs big enough, the extraction rate is initially very high but also dampens rather quickly. To maximize energy usage, time, and overall efficiency, the optimal heating time, after which it is no longer viable to continue the heating process, is calculated with the help of the optimization tool introduced in chapter 5.2, also considering relocation time and energy requirements for the in-situ

methods, as well as time and energy requirements for excavation, loading, and dumping a regolith batch for the heated chamber method. Within the simulated timeframe of $1,5 \cdot 10^6 \text{ s} \approx 17,5 \text{ days}$, the rod heating method (2) did not display a significant reduction in the extraction rate. Thus, no substantial statements regarding an optimal time could be made and no relocation of the system considered.

Figure 6-11 shows a performance comparison of (1) and (3) regarding the total extracted water mass for a fixed initial water content of $w_i = 15 \text{ wt. \%}$ and total power input $Q = 500 \text{ W}$. For (3), different possible regolith excavation rates are considered in accordance with data provided by Just et al. (2020), with a lower excavation rate being associated with a longer horizontal plot line. In total, the horizontal “zero yield” segments of the plots are due to relocation time for method (1), and due to the regolith extraction, dumping, and refilling time for method (3). It further must be noted, the yield of method (3) is from a fixed regolith volume, whereas for method (1) the dome size and thus the heated regolith surface area is a function of the applied heat flux. For a higher flux, and subsequently a smaller system size, the ideal heating cycle is substantially lower than for the biggest investigated diameter. Hence multiple heating cycles (and system relocations) can be seen for a flux of $q = 1 \text{ sol} \rightarrow \text{dome diameter } 0,68 \text{ m}$ and $q = 2 \text{ sol} \rightarrow \text{dome diameter } 0,48 \text{ m}$ (see Table 5-3), whereas for $q = 0,5 \text{ sol} \rightarrow \text{dome diameter } 0,97 \text{ m}$, the simulated timeframe is less than an optimum heating cycle would require. As explained in section 5.2, for the rod heating (2), not optimal heating time could be calculated, since no substantial decline in the extraction rate and thus sublimation lag could be observed. It is expected that extraction rates will only fall off after the simulated timeframe. Thus, the generated results for (2) were taken as the optimum.

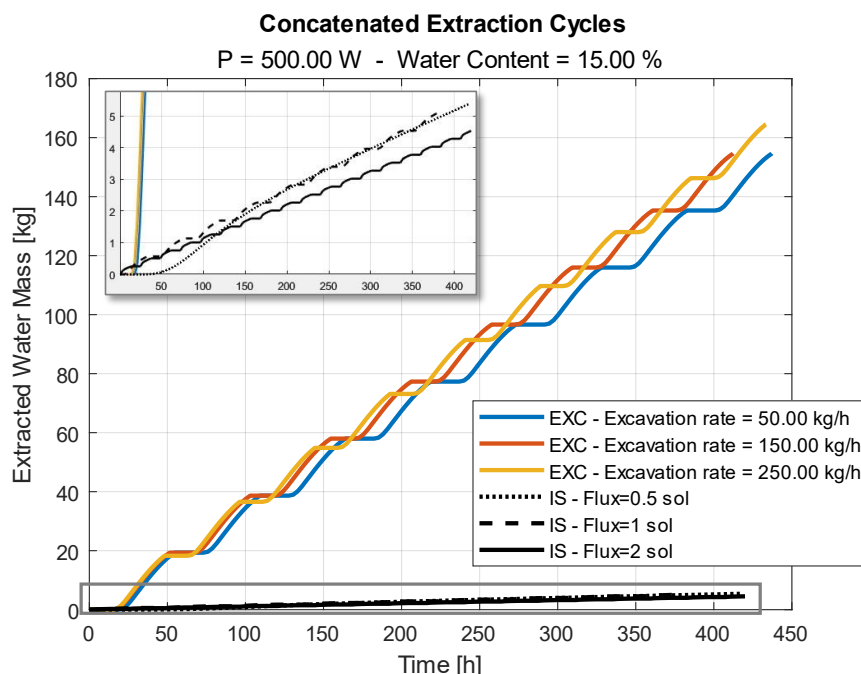


Figure 6-11: Optimized total water yield for in-situ surface heating and crucible heating, considering a system relocation for the former, as well as extraction, emptying, and refilling of a regolith batch for the latter.

While it can be seen, that for the specific water content and power input configuration shown in Figure 6-11 crucible heating outperforms surface heating by nearly a factor of ~15, the fundamental differences in system sizes due to design limitations make it hard to compare methods (1) – (3) only by the total water yield extracted.

Hence, the average water extraction rate and energy efficiency over the whole simulated timeframe of $1,5 \cdot 10^6$ s for each optimized method can be derived, which also considers the energy requirements of the relocation for method (1), and the excavation, dumping, and refilling of the regolith for method (3). The overall results are displayed in Table 6-4, Table 6-5, and Table 6-6, respectively. For the crucible heating, an excavation rate of 150 kg/h was chosen.

Table 6-4: Total water yield [kg] of the respective optimized water extraction methods

Water content [wt. %]	Power [W]	In-Situ Surface Heating (1)			In-Situ Rod Heating (2)	Crucible Heating (3)
		Power Density [W/m ²]				
		683	1366	2732		
1	500	1,18	1,07	0,82	6,58	7,53
	1500	3,78	3,43	2,62	15,61	11,94
	2500	6,41	5,83	4,45	22,39	14,40
5	500	3,35	3,12	2,29	8,86	52,02
	1500	12,65	10,82	7,78	48,69	72,41
	2500	22,68	18,94	13,61	76,58	80,32
15	500	5,37	5,45	4,37	0,13	151,90
	1500	19,93	20,81	15,56	72,41	310,05
	2500	37,71	38,66	28,09	134,84	367,48

Table 6-5: Average extraction rate [g/h] of the respective optimized water extraction methods

Water content [wt. %]	Power [W]	In-Situ Surface Heating (1)			In-Situ Rod Heating (2)	Crucible Heating (3)
		Power Density [W/m ²]				
1	500	683	1366	2732	15,80	18,10
		2,83	2,58	1,96		
		9,08	8,25	6,29		
5	500	15,40	14,00	10,70	53,80	34,60
		8,06	7,49	5,50		
		30,40	26,00	18,70		
15	500	54,50	45,50	32,70	184,00	193,00
		12,90	13,10	10,50		
		47,90	50,00	37,40		
15	2500	90,60	92,90	67,50	324,00	883,00

Table 6-6: Energy efficiency [g/kWh] of the respective optimized water extraction methods

Water content [wt. %]	Power [W]	In-Situ Surface Heating (1)			In-Situ Rod Heating (2)	Crucible Heating (3)
		Power Density [W/m ²]				
1	500	683	1366	2732	31,60	42,30
		8,90	8,86	6,95		
		8,86	6,95	10,20		
5	500	6,95	10,20	10,40	21,50	20,20
		10,20	10,40	8,17		
		10,40	8,17	10,60		
15	500	8,17	10,60	10,70	73,70	118,00
		10,60	10,70	8,46		
		10,70	8,46	21,40		
15	2500	8,46	21,40	25,20	130,00	397,00

The results reveal that generally, both methods (2) and (3) outperform method (1) in both the average extraction rate as well as the energy efficiency, with (3) further surpassing (2). The biggest gap in performance between the methods yet can be seen for energy efficiency, especially at high water contents.

Independent of the investigated extraction method and the initial water content of the lunar soil, the average extraction rate for each design is increasing for a higher total power input. This also applies to the energy efficiency in the case of both in-situ

designs (1) and (2), with exception of low water ice contents for (2). In contrast to that, an increase in power for a constant water content results in a decreasing performance regarding the energy efficiency for (3). This is mainly attributed to a fixed volume for the crucible, which independently from the applied power reliably generates very high proportions of desiccation also due to being thermally insulated. Thus, the increased power input is not needed to generate a higher yield. Yet, choosing a bigger volume for the crucible is expected to shift correlation again. For both in-situ methods, especially for (1), due to the increased surface losses, higher energy input is required to reach sublimation and maintain high regolith temperatures at the surface.

Regarding the business case introduced in chapter 3.3, to provide a NASA lunar crew with enough propellant to be able to ascend to EML1 two times a year, with additional supply transportation for a lunar settlement, a water demand of approximately 150 MT/year is required. Assuming solar independence and an average loss time of operation of 25 % during the year, this translates into a water extraction requirement of ~ 9,5 MT/17,5 days, which was the simulated timespan. As Table 6-4 shows, for the given design constraints, not method can even slightly reach this goal, with the best contender being the crucible heating with a total yield of ~ 367 kg/17,5 days.

Generally, across all designs, it can be said that the water availability inside the regolith has the biggest impact on every performance parameter. The highest improvement potential for the investigated designs is thus by mining regolith with a higher ice content or scaling up the production system. Especially the total power constraint of 2,5 kW restricted the methods in increasing their effective heated surface area, due to the minimum power density requirements of 500 W to reach sublimation (for in-situ surface heating). Thus, given a higher power availability and only taking into account the quantitative data (and neglecting other important aspects like operating and transportation costs or reliability (see chapter 6.2.2)) it is highly recommended to scale the production system (thus an increased icy regolith volume can be mined) by keeping the heat flux rather low, instead of increasing the power density for the same system size. Yet, it has to be considered that the minimum power density to reach sublimation increases with higher water content.

While both in-situ surface heating is comparably easy to scale (by either increasing the tent size or putting up multiple tents), an optimum for both the rod number, sizing, and distribution for in-situ rod heating, and an optimal crucible geometry and volume still must be determined in the future to maximize the methods respective yield, extraction rate, and energy efficiency is given a certain power constraint.

6.2.2 Qualitative Comparison

Besides the quantitative results regarding the performance (total water yield, average extraction rate, and energy efficiency) of the respective thermal extraction system, other factors are equally important to be able to make a holistic assessment of the methods. Among, others, these include the system lifetime, the accessibility of water ice, complexity, development costs, system mass, and reliability (see chapter 3.3).

For one, the **lifetime** of the system is directly linked with its capability to perform water extraction and is thus a very crucial parameter to achieve the mission objective. In contrast to a system having a higher extraction rate yet a shorter lifetime, a system with a lower extraction rate but a long lifetime may be able to acquire nonetheless more resources during its lifetime, given there is no minimum extraction rate requirement.

Even though it is not possible to make a grounded statement regarding the absolute life of the investigated extraction methods, it can be argued that the lifetime of a system is related to its **complexity**. Following that approach, it can be stated that in-situ surface heating (1) is the simplest and thus have the longest lifetime, followed by in-situ rod heating (2) and crucible heating (3) being the most complex extraction method with the smallest lifetime. While for (1), the number of moving parts is extremely limited without having any components directly interfering with the soil, the addition of heated drills in (2) increase the amount of contact with the abrasive regolith. For (3), not only an additional excavation system is needed, but also a mechanism to dump and refill the crucible required, increasing the complexity of the concept of operations. This does not only involve many mechanical elements with relative movement but at the same time, the parts are also exposed to extreme wear, further reducing their lifetime. A possible break-even point regarding the lifetime and the extraction rate of a system can be determined with a simple analysis applying the results from chapter 6.2.1. For example, an optimized method (1) is capable of extracting average $\bar{r}_{yield} = 1,87 \cdot 10^{-2} [kg/h]$ for $w_i = 5 wt. \%$, $Q = 500 W$ and $q = 2 sol.$ For the same configuration, design (3) delivers a water extraction rate of $\bar{r}_{yield} = 1,74 \cdot 10^{-1} [kg/h]$, being around 10 times higher than for method (1) (see Table 6-5). As a result, if the lifetime of (1) was roughly ten times greater than the lifetime of (3), the total water yield at the end of the mission would be identical. Yet, this factor varies per design configuration.

The **development costs** of the respective systems can also be linked to the complexity and are mainly determined by the Technology Readiness Level (TRL). Given that design (3) requires the development of more components, it is reasonable to assume that its costs will be greater, compared to both (1) and (2). This is also backed by Sowers and Dreyer (2019) and Sowers (2021), the authors establish simple mass-based cost estimates to build a relationship for the hardware development, operations, and transportation costs to the Moon. They estimate a system mass of ~29 tons for in-situ surface heating (1), ~33,5 tons for supplemented rod heating (2), and ~40,4 tons for heating after excavation (3). While those absolute values are not representative of this work due to differences in system scaling and technology usage, they still can be used as a baseline for this discussion. Table 6-7 displays the cost-estimating relationships for development, transportation, and operation costs concerning the derived system masses. However, many parts including heaters and sealings would be at least partially interchangeable between the designs. According to NASA (2007), a TRL of 3 equates to "proof-of-concept, based on the TRLs of the proposed designs. This tier is distinguished by analytical and experimental proof-of-concept critical functions, which are taken to be the status for all designs taken into consideration.

Table 6-7: Cost estimating relationships regarding system masses (Sowers and Dreyer 2019)

Parameter	Cost estimating relationship	Basis
Development and build	\$ 50.000/kg	Commercial space hardware
Transportation	\$ 35.000/kg	Vulcan ACES lander
Operations and maintenance	\$ 3.000/kg	Teleoperation with spare part delivery

Even though the **reliability** of the systems is critical to mission success, to be able to make a sophisticated assessment regarding the single-fault tolerance of critical system functions, the concept designs would need to be elaborated on a more detailed level. However, for all the methods single failure points can be determined. While for both (1) and (2), a structural failure of the vapor capturing dome due to e.g. erosion caused by the abrasive lunar dust would result in a severe leakage and thus imply huge losses, a failure of e.g. the excavator would completely hinder (3) to produce water. Since the reliability of a system can also relate to the complexity and the number of used components, many additional failure modes can be identified, since the excavation system must continuously and autonomously interface with the heating chamber as well as with the regolith, whose mechanical response has a high degree of uncertainty. For (1) and (2), the primary risk is the effectiveness of direct heating to sublimate ice at a sufficient rate to be economical, which is also due to the possibility of water vapor deposition in cold and dense regolith regions.

Furthermore, the **accessibility** of the water ice is a crucial aspect as well. As explained in chapter 2.1.2. both the exact form and distribution (lateral as well as horizontal) of lunar water ice is still unknown. In this work, a homogenous distribution over the whole regolith surface volume in accordance with Wasilewski (2021b), Schieber et al. (2022), and Li et al. (2018) was implemented. Should the concentration of the water ice however be in deeper regolith layers, as proposed by e.g. Benna et al. (2019) or Reiss et al. (2021), this would especially impact method (1), due to its very limited ability to transfer heat into depth, as presented in Table 6-1. While inserting heated rods (3) into the regolith helps with the heat distribution, the lateral reach is also still limited to the length of the latter due to the low thermal conductivity of the regolith. This is similar to (3), with its ability to reach depth being dependent on the excavation subsystem. In accordance with current excavation technologies (Just et al. 2020), it is deemed that excavating the regolith yet provides a deeper reach than drilling holes for inserting the rods.

6.2.3 Overview of the Comparison

While both the quantitative and qualitative factors have been compared and discussed respectively, due to their high interconnectivity and lack of further information it is difficult to put a weight on the single aspects and rank them regarding their importance. Yet, an approach to quantitatively linking the generated results with the system lifetime was made, assuming no time constraints for a required water yield.

A comprehensive system evaluation can thus only be made qualitatively and is shown in Table 6-8. The ascribed ratings solely serve to inform the reader about the fundamental factors guiding the evaluation rather than to determine which choice is the overall best. While in terms of complexity, lifetime, and reliability method (1) is deemed to have advantages compared to the other methods, both its extraction rate and energy efficiency are substantially lower than for design (3), which scores last in complexity and lifetime. Thus, the used design must be chosen concerning the individual mission objectives in consideration of all the presented aspects.

Table 6-8: Qualitative assessment overview

	Extraction Rate	Energy Efficiency	Complexity	Lifetime	Reliability	Development Cost	Accessibility
In-situ Surface Heating (1)	(C) Sublimation lag build-up	(C) High surface losses	(A) Mostly static design with no regolith manipulation	(A) Elements susceptible to moderate wear	(B) Tent structure; redeposition	(D) Low TRL	(D) Very shallow reach
In-situ Rod Heating (2)	(B) Possible difficulties in vapor outgassing	(B) Surface losses; drilling	(B) Few moving parts, partial regolith manipulation	(C) Elements susceptible to high-rate wear	(C) Tent structure, redeposition; drilling tool	(D) Low TRL	(B) Length of the rods; difficult outgassing
Crucible Heating (3)	(A) Heating from more sides	(A) Insulated, yet Excavation required	(D) Many moving parts, regolith manipulation, refilling & dumping	(D) Cardinal elements susceptible to high-rate wear	(C) Excavator; autonomous operations	(D) Low TRL	(A) Reach of the excavation system

(A)	Excellent
(B)	Good
(C)	Correctable Deficiency
(D)	Fundamental Deficiency

6.3 Additional Regolith and Ambient Parameter Variations

The already highly discussed uncertainty in thermophysical properties of the lunar regolith due to missing ground truth data is a source of error in the thermal extraction of water ice. Crucial parameters for this problem are considered to be the initial temperature, thermal conductivity, and specific heat capacity of the regolith, the phase change temperature and transition interval as well as the chosen mixing model and the pore filling fraction on the water extraction capability of the different methods. Therefore, an additional study was conducted to better understand the reliability and robustness of the investigated designs. Due to the very high computational cost of simulating the in-situ rod heating (2), only surface heating (1) and crucible heating (3) were considered for this. The model variables explored in the previous chapter will be fixed and set according to the baseline setup (see Table 5-1). An exception is made for examining the different use cases presented in chapter 3.2, for which the initial water content is also adjusted to the respective case.

For the main study, PSR regolith temperatures of 40 K were assumed. Yet, water is also expected to occur outside of the PSRs. Thus, three highly abstracted and simplified use cases were introduced in chapter 3.2, considering possible water ice extraction locations (1) inside PSRs, (2) in micro cold-traps, and (3) outside PSRs, with respective variations in regolith temperature and water wt.% present ((1) $T_{amb} = 40 K$, $w_i = 0.15$ 2) $T_{amb} = 75 K$, $w_i = 0.05$ 3) $T_{amb} = 110 K$, $w_i = 0.01$). As seen in Figure 6-12, while the initial regolith temperature does play a role regarding the possible total yield (higher initial temperature reduces ΔT needed for sublimation) and increases the yield for both in-situ surface heating (1) and crucible heating (3) for constant water content, the variation of the latter has a much higher impact on the yield. This is also expected, since more water can be extracted for a given volume, but also crucial thermophysical properties like the thermal conductivity of the icy regolith get improved for increasing water content.

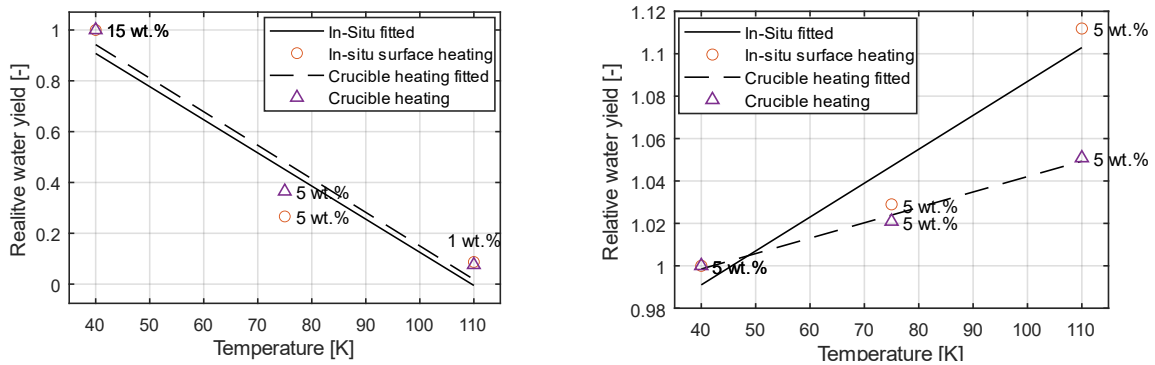


Figure 6-12: Relative water yield for varying initial regolith temperatures with correspondent water contents according to the Use Cases (left) and with constant water contents (right)

Besides the regolith temperature, also the phase change temperature T_{pc} and the phase change transition interval $\Delta T_{1 \rightarrow 2}$ are determining the stability of the water ice within the regolith. As introduced in chapter 5.1.2, both parameters are estimated to have relatively high uncertainty. Compared to conventional equations derived from the phase change diagram, the porous space, and other impurities tend to make water ice increasingly more stable in a vacuum (Kossacki and Leliwa-Kopystynski 2014), yet further research needs to be conducted in this matter. Concerning the phase change temperature, the total water yield is simply expected to be higher for a lower value and vis versa (highly similar extraction behavior like for changing the initial regolith temperature: the ΔT needed to reach sublimation is the same for increasing the initial temperature by 20 K or lower the sublimation temperature by 20 K, neglecting the implications of temperature-dependent regolith properties like the thermal conductivity or surface losses). The transition interval on the other hand indicates the range, in which the latent heat of the sublimation is applied. Lower values for this parameter resulted in a stepped and sharp interphase movement and thus production progression, compared to a smoother progression for higher values, as seen in Figure 6-13. This is because a higher absolute value of the latent heat is released more quickly, resulting in further sublimation lag, since most of the ice is quickly desiccated (see Figure 6-13). Yet, the sublimation process is expected to be smoother due to solving a high non-linear problem (Wasilewski 2021b). For the crucible heating (3), this effect could not be noticed.

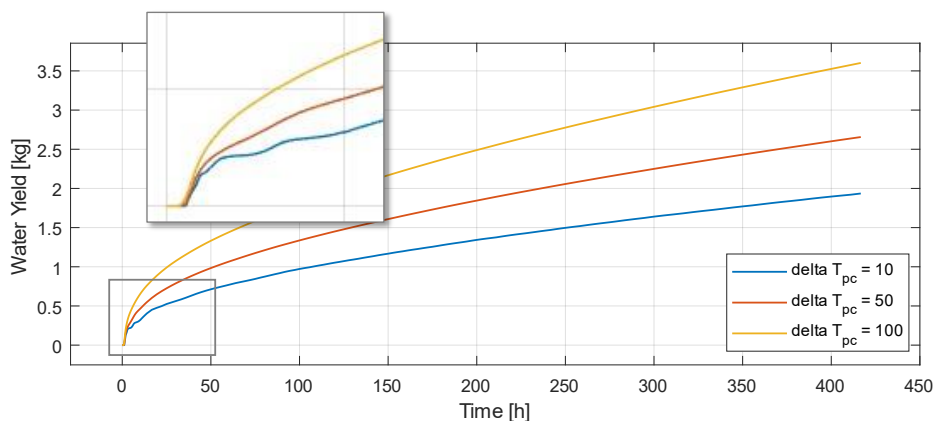


Figure 6-13: Production progression for various phase change transition intervals for in-situ surface heating

Due to the high range of approximations found in the literature regarding the thermal conductivity and heat capacity of regolith, the impact on the possible water yield by varying between the most prominent models is also investigated. For the thermal conductivity, besides the thermal conductivity used in this study introduced by Martinez and Siegler (2021), also the conductivities proposed by Reiss (2018a) and Woods-Robinson et al. (2019) have been considered (for a graphical representation of the investigated conductivities, please refer to Figure 4-4). As seen in Figure 6-14, differences in the applied thermal conductivity had a considerable impact on the production progression and total yield of (1), with a lower average conductivity (Reiss 2018a) resulting in ~ half the water yield than for the conductivity used in this study (Martinez and Siegler 2021), which is as expected. Yet, this behavior could not be seen for the crucible, which is mainly due to the limited sample volume, as light variations in the production progression can be seen for the initial production phase. For in increased crucible volume, the thermal at constant power input, the thermal conductivity is yet expected to have a greater impact.

Concerning the specific heat capacity of the regolith, the model from Woods-Robinson et al. (2019) was complemented by models from Schreiner et al. (2016) and Hayne et al. (2021) Differences in the specific heat models are mainly in very low-temperature ranges < 100 K as well as in high ranges > 600 K (seen Figure 4-5). As seen in Figure 6-15, the impact of the specific heat on the generated yield is thus considerably neglectable for both (1) and (2).

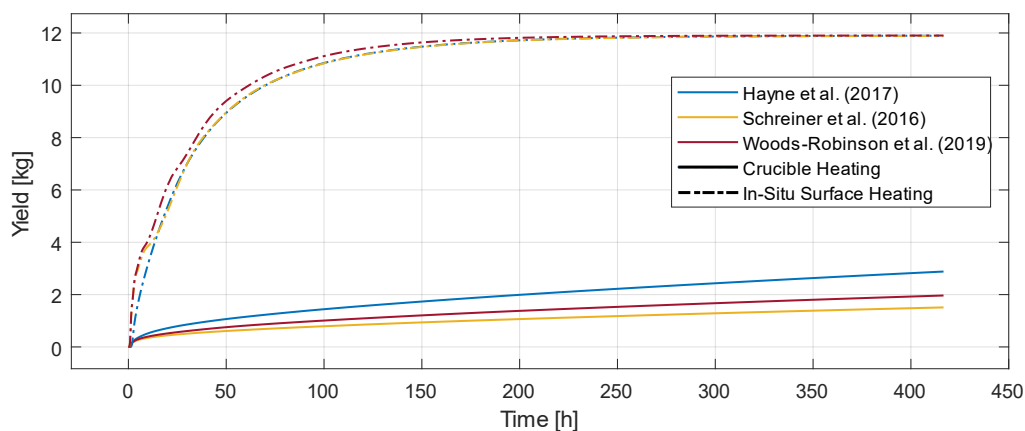


Figure 6-14: Impact of varying thermal conductivities of the regolith on the total water yield (at constant pressure)

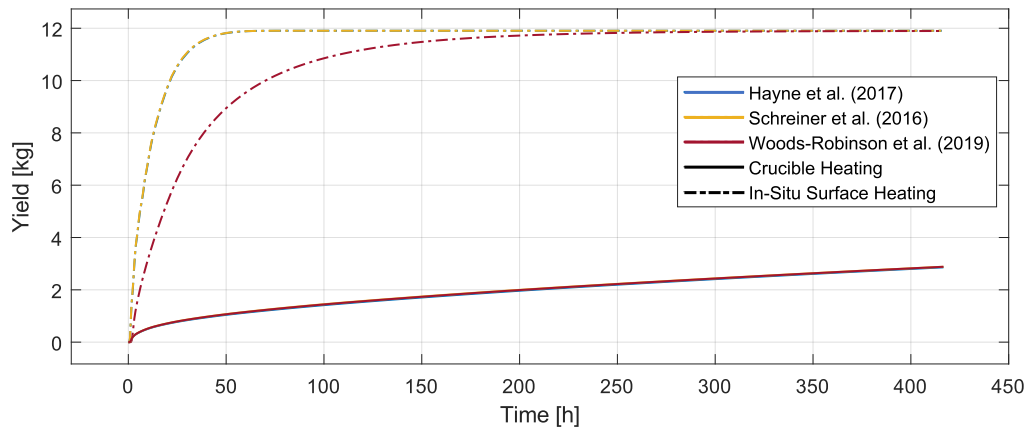


Figure 6-15: Impact of varying specific heat capacities of the regolith on the total water yield

Furthermore, the chosen mixing model is highly influencing the effective thermophysical properties of the icy regolith. As described in chapter 4.1.2, for this study a volumetric mixing model according to Siegler et al. (2012) was chosen with a homogeneous distribution of the ice within the pores of the regolith. This couples the porosity and subsequently the density of the effective mixture with the ice content via the pore-filling fraction. Due to the depth dependency of the porosity (see Figure 4-2), this resulted in a saturation (pores are completely filled with ice) of the regolith for a 15% icy deposit in a depth of $\sim 0,2$ m (surface filling fraction $\sim 0,65$). For a higher ice content, this mixing model would be unphysical due to reaching filling fractions > 1 . For higher regolith surface densities, deeper thermal extraction, or even higher water contents, the mixing model used in this work may not be relevant. The effect of other mixing models on water vapor generation must be assessed in the future.

7 Conclusion

In-Situ Resource Utilization is considered to not only drastically reduce the cost of space missions, but also enable further consistent and sustainable human space exploration. Beyond Earth, the closest and most accessible source of resources is the Moon. Especially water is seen as a crucial resource since it can be used for both life support and rocket fuel production. Yet, for its successful extraction, it is necessary to understand what methods are most suitable to obtain water and what parameters influence the extraction performance.

In this work, three different lunar thermal water extraction methods, namely in-situ surface heating, rod heating, as well as crucible heating after excavation, have been modeled, simulated, and successfully assessed and compared. The selection of the designs was based on an extensive literature review regarding their applicability for thermal extraction on a larger scale. For reference, a simplified business case was developed to be able to make statements about the economic viability of the investigated methods. A holistic heat and mass transfer model was presented, combining and supplementing three of the most prominent approaches of thermal volatile extraction on the Moon (Reiss 2018a; Wasilewski 2021b; Schieber et al. 2022). The relevant mechanisms have been implemented in the software *COMSOL Multiphysics*.

Given a power constraint of max. 2,5 kW, a parameter study was conducted to determine the impact of varying icy deposits from 1 wt.% to 15 wt.% on the average extraction rate and energy efficiency of the system. Since also the power density is a decisive factor concerning the sublimation capability of the system, it was also considered for the in-situ surface heating. The extraction process was simulated over ~17,5 Earth days, which is close to a lunar sun cycle at the PSRs. The generated results were further optimized concerning an optimum heating time with the help of an algorithm developed by Kiewiet et al. (2022), after which heating was no longer worthwhile. For that, time and energy requirements for relocating the dome in case of in-situ methods, as well as excavating, emptying, and refilling requirements for the crucible heating were considered. The evaluation also took into account factors like system lifetime, accessibility to water ice, complexity, reliability, and development costs due to the low fidelity of the evaluated designs.

In general, especially the low thermal conductivity of the regolith was shown as a major bottleneck for thermal extraction. Furthermore, the water content of the soil was determined to have the biggest impact on the yield by greatly influencing the thermophysical properties of the regolith and simply providing more extractable water. An increase in the water content resulted in a higher energy requirement to initially reach sublimation. Due to the high uncertainty in thermophysical properties of the lunar regolith attributed to missing ground truth data, an additional sensitivity analysis was conducted, which further increased the confidence in the results.

The results showed that the crucible design is outperforming both in-situ surface heating and the heated rods method for all performance indicators. For the optimized heating time, the crucible reached an average up to ~ 0,9 kg/h (heated rods: ~ 0,32 kg/h; surface heating: ~ 0,09 kg/h) and was able to extract up to ~ 765 g/kWh (heated rods: ~ 130 g/kWh; surface heating ~25 g/kWh). This can mainly be attributed to the crucible being a completely closed system and having additional thermal insulation. Generally, for in-situ surface heating it was found that applying a lower power density

(and consequently, having a larger surface coverage and system size) led to a higher yield. The in-situ heated rod design had a better accessibility of depth and can be allocated a medium relative performance. Given the strict power constraint, the proposed business case (150 MT/year) could not be met. For that, an adequate up-scaling of the respective systems is needed (~ 26 times higher yield required for the crucible).

Considering further criteria, the in-situ methods are expected to both have advantages e.g. lifetime, complexity, and reliability compared to the crucible design. An overall design assessment must thus follow a holistic approach and be adapted to the individual mission objectives. Thus, this work successfully answered the research question and the scientific gap, by providing a framework to determine the most suitable thermal extraction method in case of certain scenarios and identifying crucial parameters influencing the performance of a system.

8 Outlook

Modeling

While it was found that for in-situ surface heating, the biggest dome size always results in the highest yield, an optimization for both the number, distribution, and size of the heated rods regarding the extraction rate and efficiency still has to be done. The same applies to the geometry and volume of the crucible

Since the main parameter study of this work was mainly focused on heat and phase change modeling to derive the total water extraction yield, future work could further consider a fully coupled heat and mass transfer model, accounting for a dynamically changing pressure domain due to vapor production, diffusion, and advection. This would provide more detailed insights into loss estimations due to e.g. redeposition of the vapor.

Furthermore, by considering the pressure domain and the resulting molar vapor fluxes, the sealing some both in-situ methods can be modeled as well. This would have further implications on possible vapor redeposition in the domain, since a pressure build-up within the dome counteracts the pressure gradient towards to surface, possibly impeding vapor outgassing. Associated with this is also the further modeling of vapor recapturing due to e.g. cold traps, adsorbent beds, or layer traps.

Also, other forms of heating (e.g. microwave heating) could be considered in the future to investigate possible implications. Transient heating (e.g. pulse heating) could also further improve extraction efficiency and prevent possible sintering for high power densities applied to e.g. a crucible.

Experimental Validation

Furthermore, in the next step, the theoretical models presented here can be experimentally validated. Based on the presented results, the SMU group at DLR is investigating both the in-situ surface heating method as well as a more complex and completely closed system similar to the presented crucible design further, conducting large-scale experiments with icy regolith in representative temperature and pressure conditions. While for in-situ surface heating, especially the system simplicity is decisive, crucible heating was chosen according to the current state of ambiguity regarding the lateral distribution of water ice inside the regolith due to its ability to reach deeper layers as well as the high performance in extraction rate and energy efficiency.

A References

- Andreas, E. L. (2007), 'New estimates for the sublimation rate for ice on the Moon', *Icarus*, 186/1: 24–30.
- Arnold, J. R. (1979), 'Ice in the lunar polar regions', *J. Geophys. Res.*, 84/B10: 5659.
- Atkinson, J., Prasad, M., Abbud-Madrid, A. et al. (2019), 'Penetration and relaxation behavior of dry lunar regolith simulants', *Icarus*, 328: 82–92.
- Barmatz, M., Steinfeld, D., and Winterhalter, D. (2013), *Microwave Heating Studies and Instrumentation for Processing Lunar*.
- Basilevsky, A. T., Abdrakhimov, A. M., and Dorofeeva, V. A. (2012), 'Water and other volatiles on the moon: A review', *Sol Syst Res*, 46/2: 89–107.
- Benna, M., Hurley, D. M., Stubbs, T. J. et al. (2019), 'Lunar soil hydration constrained by exospheric water liberated by meteoroid impacts', *Nature geoscience*, 12/May: 333–338.
- Bennett, N. J., Ellender, D., and Dempster, A. G. (2020), 'Commercial viability of lunar In-Situ Resource Utilization (ISRU)', *Planetary and Space Science*, 182: 104842.
- Bergman, T. L., and Incropera, F. P. (2011), *Fundamentals of Heat and Mass Transfer* (7th Edition: John Wiley & Sons).
- Biele, J., Grott, M., Knollenberg, J. et al. (2022), *Knowledge gaps in our understanding of the mechanisms governing heat transport in regolith at low temperatures*.
- Biswas, J., Sheridan, S., Pitcher, C. et al. (2020), 'Searching for potential ice-rich mining sites on the Moon with the Lunar Volatiles Scout', *Planetary and Space Science*, 181/6: 104826.
- Blessing, L. T.M., and Chakrabarti, A. (2009), *DRM, a Design Research Methodology* (London: Springer London).
- Bonales, L. J., Rodriguez, A. C., and Sanz, P. D. (2017), 'Thermal conductivity of ice prepared under different conditions', *International Journal of Food Properties*, 20/sup1: 610–619.
- Bravo, M. C. (2007), 'Effect of transition from slip to free molecular flow on gas transport in porous media', *Journal of Applied Physics*, 102/7: 74905.
- Brisset, J., Miletich, T., and Metzger, P. (2020), 'Thermal extraction of water ice from the lunar surface - A 3D numerical model', *Planetary and Space Science*, 193/1: 105082.
- Buck, A. L. (1981), 'New Equations for Computing Vapor Pressure and Enhancement Factor', *J. Appl. Meteor.*, 20/12: 1527–1532.
- Calla, O. P. N., Mathur, S., and Gadri, K. L. (2016), 'Quantification of Water Ice in the Hermite-A Crater of the Lunar North Pole', *IEEE Geosci. Remote Sensing Lett.*, 13/7: 926–930.
- Cannon, K. M. (2020), 'Lunar Mining & Landing Sites' <<https://kevincannon.rocks/lunarmining/>>, accessed 27 Apr 2022.

- Cannon, K. M., and Britt, D. T. (2020), 'A geologic model for lunar ice deposits at mining scales', *Icarus*, 347/B10: 113778.
- Charania, A. C., and DePasquale, D. (2007), *Economic analysis of lunar in-situ resource utilization (ISRU) propellant services market* <<http://www.sei.aero/archive/IAC-07-A5.1.03.pdf>>.
- Christensen, E. M., Choate, R., Jaffe, L. D. et al. (1967), 'Surveyor v: lunar surface mechanical properties', *Science (New York, N.Y.)*, 158/3801: 637–640.
- Cichan, T., Bailey, S. A., Antonelli, T. et al. (2017), 'Mars Base Camp: An Architecture for Sending Humans to Mars', *New Space*, 5/4: 203–218.
- Clark, R. N. (2009), 'Detection of adsorbed water and hydroxyl on the Moon', *Science (New York, N.Y.)*, 326/5952: 562–564.
- Clifford, S. M., and Hillel, D. (1986), 'Knudsen Diffusion', *Soil Science*, 141/4: 289–297.
- Colaprete, A., Schultz, P., Heldmann, J. et al. (2010), 'Detection of water in the LCROSS ejecta plume', *Science (New York, N.Y.)*, 330/6003: 463–468.
- Colwell, J. E., Batiste, S., Horányi, M. et al. (2007), 'Lunar surface: Dust dynamics and regolith mechanics', *Rev. Geophys.*, 45/2: 7420.
- Comiti, J., and Renaud, M. (1989), 'A new model for determining mean structure parameters of fixed beds from pressure drop measurements: application to beds packed with parallelepipedal particles', *Chemical Engineering Science*, 44/7: 1539–1545.
- COMSOL Documentation (2021), *Mesh Element Quality and Size* <<https://doc.comsol.com/6.1/docserver/>>.
- Cremers, C. J. (1975), 'Thermophysical properties of Apollo 14 fines', *J. Geophys. Res.*, 80/32: 4466–4470.
- Duke, M., Gustafson, R., and Rice, E., 'Mining of Lunar polar ice', in , *36th AIAA Aerospace Sciences Meeting 1998*.
- Ellsworth, K., and Schubert, G. (1983), 'Saturn's icy satellites: Thermal and structural models', *Icarus*, 54/3: 490–510.
- El-Maghlany, W. M., Bedir, A. E.-R., Elhelw, M. et al. (2019), 'Freeze-drying modeling via multi-phase porous media transport model', *International Journal of Thermal Sciences*, 135: 509–522.
- Elphic, R. C., Eke, V. R., Teodoro, L. F. A. et al. (2007), 'Models of the distribution and abundance of hydrogen at the lunar south pole', *Geophys. Res. Lett.*, 34/13: n/a-n/a.
- ESA (2019), 'About PROSPECT' <<https://exploration.esa.int/web/moon/-/59102-about-prospect>>, updated 1 Sep 2019, accessed 2 Jul 2022.
- Evans, R. B., Watson, G. M., and Mason, E. A. (1961), 'Gaseous Diffusion in Porous Media at Uniform Pressure', *The Journal of Chemical Physics*, 35/6: 2076–2083.
- Fanale, F. P., Salvail, J. R., Matson, D. L. et al. (1990), 'The effect of volume phase changes, mass transport, sunlight penetration, and densification on the thermal regime of icy regoliths', *Icarus*, 88/1: 193–204.

- Feistel, R., and Wagner, W. (2007), 'Sublimation pressure and sublimation enthalpy of H₂O ice Ih between 0 and 273.16K', *Geochimica et Cosmochimica Acta*, 71/1: 36–45.
- Feldman, W. C., Maurice, S., Binder, A. B. et al. (1998), 'Fluxes of fast and epithermal neutrons from Lunar Prospector: evidence for water ice at the lunar poles', *Science (New York, N.Y.)*, 281/5382: 1496–1500.
- Ferrari, C. (2018), 'Thermal Properties of Icy Surfaces in the Outer Solar System', *Space Sci Rev*, 214/8: 985.
- Flubacher, P., Leadbetter, A. J., and Morrison, J. A. (1960), 'Heat Capacity of Ice at Low Temperatures', *The Journal of Chemical Physics*, 33/6: 1751–1755.
- Foust, J. (2019), 'Gateway or bust: NASA's plan for a 2024 lunar landing depends on a much-criticized orbital outpost', *IEEE Spectr.*, 56/7: 32–37.
- Fray, N., and Schmitt, B. (2009), 'Sublimation of ices of astrophysical interest: A bibliographic review', *Planetary and Space Science*, 57/14-15: 2053–2080.
- Fukusako, S. (1990), 'Thermophysical properties of ice, snow, and sea ice', *Int J Thermophys*, 11/2: 353–372.
- Gertsch, L. (2006), 'Effect of Water Ice Content on Excavatability of Lunar Regolith', in , *AIP Conference Proceedings (AIP)*, 1093–100.
- Ghanbarian, B., Hunt, A. G., Ewing, R. P. et al. (2013), 'Tortuosity in Porous Media: A Critical Review', *Soil Science Society of America Journal*, 77/5: 1461–1477.
- Gladstone, G. R., Hurley, D. M., Retherford, K. D. et al. (2010), 'LRO-LAMP observations of the LCROSS impact plume', *Science (New York, N.Y.)*, 330/6003: 472–476.
- Gori, F., and Corasaniti, S. (2004), 'Theoretical prediction of the thermal conductivity and temperature variation inside mars soil analogues', *Planetary and Space Science*, 52/1-3: 91–99.
- Gothäll, H. (2022), 'How to Inspect Your Mesh in COMSOL Multiphysics®' <<https://www.comsol.de/blogs/how-to-inspect-your-mesh-in-comsol-multiphysics/>>, updated 6 Jul 2022, accessed 9 Oct 2022.
- Greig, A. D. (2021), 'Ablative Arc Mining for In-Situ Resource Utilization' <https://www.nasa.gov/directorates/spacetech/niac/2021_Phase_I/Ablative_Arc_Mining_for_In-Situ_Resource_Utilization/>, updated 19 Feb 2022, accessed 24 May 2022.
- Griesinger, A., Spindler, K., and Hahne, E. (1999), 'Measurements and theoretical modelling of the effective thermal conductivity of zeolites', *International Journal of Heat and Mass Transfer*, 42/23: 4363–4374.
- Gustafson, R., White, B., Fidler, M. et al. (01042010), 'Demonstrating the Solar Carbothermal Reduction of Lunar Regolith to Produce Oxygen', in , *48th AIAA Aerospace Sciences Meeting Including the New Horizons Forum and Aerospace Exposition (Reston, Virginia: American Institute of Aeronautics and Astronautics)*, 857.
- Hager, P. B., and Binns, D. (2021), *Thermal design challenges for lunar ISRU payloads*.

- Hayne, P. O., Aharonson, O., and Schörghofer, N. (2021), 'Micro cold traps on the Moon', *Nat Astron*, 5/2: 169–175.
- Hayne, P. O., Bandfield, J. L., Siegler, M. A. et al. (2017), 'Global Regolith Thermophysical Properties of the Moon From the Diviner Lunar Radiometer Experiment', *J Geophys Res Planets*, 122/12: 2371–2400.
- Haynes, D. R., Tro, N. J., and George, S. M. (1992), 'Condensation and evaporation of water on ice surfaces', *J. Phys. Chem.*, 96/21: 8502–8509.
- He, L., Wang, C., Zhang, G. et al. (2021), 'A novel auger-based system for extraterrestrial in-situ water resource extraction', *Icarus*, 367/5948: 114552.
- He, W., Zou, J., Wang, B. et al. (2013), 'Gas transport in porous electrodes of solid oxide fuel cells: A review on diffusion and diffusivity measurement', *Journal of Power Sources*, 237/5: 64–73.
- Hecht, M. (2006), 'Transient liquid water near an artificial heat source on Mars', *Mars*, 2: 83–96.
- Heiken, G., Vaniman, D., French, Bevan M. Heiken, Grant et al. (1991), *Lunar sourcebook: A user's guide to the moon* (Houston, Texas: Lunar and Planetary Institute).
- Heldmann, J. L., Colaprete, A., Elphic, R. C. et al. (2015), 'Real-time science operations to support a lunar polar volatiles rover mission', *Advances in Space Research*, 55/10: 2427–2437.
- Hemingway, B. S., Robie, R. A., and Wilson, W. H., *Specific heats of lunar soils, basalt, and breccias from the Apollo 14, 15, and 16 landing sites, between 90 and 350°K* <<https://articles.adsabs.harvard.edu/full/1973LPSC...4.2481H/0002481.000.html>>.
- Ho, C. K. (2006), *Gas transport in porous media* (Theory and applications of transport in porous media, 20, Dordrecht: Springer).
- Honniball, C. I., Lucey, P. G., Li, S. et al. (2021), 'Molecular water detected on the sunlit Moon by SOFIA', *Nat Astron*, 5/2: 121–127.
- Hudson, T. L., Aharonson, O., Schorghofer, N. et al. (2007), 'Water vapor diffusion in Mars subsurface environments', *J. Geophys. Res.*, 112/E5: 405.
- Hudson, T. L., Aharonson, O., and Schorghofer, N. (2009), 'Laboratory experiments and models of diffusive emplacement of ground ice on Mars', *J. Geophys. Res.*, 114/E1: E00A03.
- ISECG (2021), *In_situ resource utilization assessment report*.
- Jackson, K. A. (2012), *Kinetic processes: Crystal growth, diffusion, and phase transitions in materials* (Second, completely revised and enlarged edition, 1st Reprint, Weinheim: Wiley-VCH Verlag GmbH & Co. KGaA).
- Jones, C. A., Klovstad, J., Judd, E. et al., 'Cost Breakeven Analysis of Cis-lunar ISRU for Propellant', in , *AIAA Scitech 2019 Forum 2019*.
- Just, G. H., Smith, K., Joy, K. H. et al. (2020), 'Parametric review of existing regolith excavation techniques for lunar In Situ Resource Utilisation (ISRU) and recommendations for future excavation experiments', *Planetary and Space Science*, 180/4: 104746.

- Kast, W., and Hohenthanner, C.-R. (2000), 'Mass transfer within the gas-phase of porous media', *International Journal of Heat and Mass Transfer*, 43/5: 807–823.
- Kiewiet, L., Hab, N. M., Marchese, F. M. et al. (2022), *Trade-off and optimization for thermal Lunar water extraction system* (Paris).
- Kleinhenz, J. E., and McAdam, A. (2021), *An Overview of the Lunar Water ISRU Measurement Study (LWIMS): Explore Moon to Mars*.
- Klinger, J. (1981), 'Some consequences of a phase transition of water ice on the heat balance of comet nuclei', *Icarus*, 47/3: 320–324.
- Kornuta, D., Abbud-Madrid, A., Atkinson, J. et al. (2019), 'Commercial lunar propellant architecture: A collaborative study of lunar propellant production', *REACH*, 13/12: 100026.
- Kossacki, K. J., and Leliwa-Kopystynski, J. (2014), 'Temperature dependence of the sublimation rate of water ice: Influence of impurities', *Icarus*, 233: 101–105.
- Kulkarni, K. M., and Abhang, R. B. (2021), *Microwave powered extraction of water ice from the permanently shadowed regions on the lunar surface*.
- LaMarche, C. Q., Curtis, J. S., and Metzger, P. T. (2011), 'Permeability of JSC-1A: A lunar soil simulant', *Icarus*, 212/1: 383–389.
- Ledlow, M. J., Zeilik, M., Burns, J. O. et al. (1992), 'Subsurface emissions from Mercury - VLA radio observations at 2 and 6 centimeters', *ApJ*, 384: 640.
- Li, S., Lucey, P. G., Milliken, R. E. et al. (2018), 'Direct evidence of surface exposed water ice in the lunar polar regions', *Proceedings of the National Academy of Sciences of the United States of America*, 115/36: 8907–8912.
- Li, S., and Milliken, R. E. (2017), 'Water on the surface of the Moon as seen by the Moon Mineralogy Mapper: Distribution, abundance, and origins', *Science advances*, 3/9: e1701471.
- Lin, H., Li, S., Xu, R. et al. (2022), 'In situ detection of water on the Moon by the Chang'E-5 lander', *Science advances*, 8/1: eabl9174.
- Loff, S. (2019), 'New VIPER Lunar Rover to Map Water Ice on the Moon' <<https://www.nasa.gov/feature/new-viper-lunar-rover-to-map-water-ice-on-the-moon/>>, updated 16 Nov 2020, accessed 26 Apr 2022.
- LSA (2018), *Opportunities for Space Resources Utilization: Future markets & value chains*, Study Summary <spaceresources.lu>.
- Lund, T. (2018), *Early Exploration of the Moon* (Cham: Springer International Publishing).
- Marburger, J. (2006), *44th Robert H. Goddard Memorial Symposium*, Keynote Address, 2006 (Greenbelt, Maryland).
- Marti, J., and Mauersberger, K. (1993), 'A survey and new measurements of ice vapor pressure at temperatures between 170 and 250K', *Geophys. Res. Lett.*, 20/5: 363–366.
- Martinez, A., and Siegler, M. A. (2021), 'A Global Thermal Conductivity Model for Lunar Regolith at Low Temperatures', *J Geophys Res Planets*, 126/10: 297.

- MASTEN (2021), 'Break the Ice: Masten Designs Rocket Mining System to Extract Lunar Water' <<https://masten.aero/blog/masten-designs-rocket-mining-system/>>, updated 17 Jun 2021, accessed 15 Apr 2022.
- Mazarico, E., Neumann, G. A., Smith, D. E. et al. (2011), 'Illumination conditions of the lunar polar regions using LOLA topography', *Icarus*, 211/2: 1066–1081.
- McCloy, J. S., Sundaram, S. K., Matyas, J. et al. (2011), 'Simultaneous measurement of temperature and emissivity of lunar regolith simulant using dual-channel millimeter-wave radiometry', *The Review of scientific instruments*, 82/5: 54703.
- McCord, T. B., Taylor, L. A., Combe, J.-P. et al. (2011), 'Sources and physical processes responsible for OH/H₂O in the lunar soil as revealed by the Moon Mineralogy Mapper (M₃)', *J. Geophys. Res.*, 116/E2: 1309.
- McGovern, J. A., Bussey, D. B., Greenhagen, B. T. et al. (2013), 'Mapping and characterization of non-polar permanent shadows on the lunar surface', *Icarus*, 223/1: 566–581.
- McIntosh, I. M., Nichols, A. R.L., Tani, K. et al. (2017), 'Accounting for the species-dependence of the 3500 cm⁻¹ H₂O infrared molar absorptivity coefficient: Implications for hydrated volcanic glasses', *American Mineralogist*, 102/8: 1677–1689.
- Mellon, M. T., Jakosky, B. M., and Postawko, S. E. (1997), 'The persistence of equatorial ground ice on Mars', *J. Geophys. Res.*, 102/E8: 19357–19369.
- Metzger, P. (2020), 'Aqua Factorem: Ultra Low-Energy Lunar Water Extraction' <https://www.nasa.gov/directorates/spacetech/niac/2020_Phase_I_Phase_II/Aqua_Factorem/>, updated 7 May 2020, accessed 20 Apr 2022.
- Metzger, P. T. (11152018), 'Modeling the Thermal Extraction of Water Ice from Regolith', in R. B. Malla, R. K. Goldberg, and A. D. Roberts (eds.), *Earth and Space 2018* (Reston, VA: American Society of Civil Engineers), 481–9.
- Metzger, P. T., Zacny, K., and Morrison, P. (2020), 'Thermal Extraction of Volatiles from Lunar and Asteroid Regolith in Axisymmetric Crank–Nicolson Modeling', *J. Aerosp. Eng.*, 33/6: 2481.
- Meurisse, A., and Carpenter, J. (2020), 'Past, present and future rationale for space resource utilisation', *Planetary and Space Science*, 182/E11: 104853.
- Millington, R. J. (1959), 'Gas Diffusion in Porous Media', *Science (New York, N.Y.)*, 130/3367: 100–102.
- Mitrofanov, I. G., Sanin, A. B., Boynton, W. V. et al. (2010), 'Hydrogen mapping of the lunar south pole using the LRO neutron detector experiment LEND', *Science (New York, N.Y.)*, 330/6003: 483–486.
- Mueller, R. P., Cox, R. E., Ebert, T. et al. (2013 - 2013), 'Regolith Advanced Surface Systems Operations Robot (RASSOR)', in , *2013 IEEE Aerospace Conference* (IEEE), 1–12.
- Murphy, D. M., and Koop, T. (2005), 'Review of the vapour pressures of ice and supercooled water for atmospheric applications', *Q. J. R. Meteorol. Soc.*, 131/608: 1539–1565.
- NASA (2007), *Nasa Systems Engineering Handbook* (Washington, DC).

- (2013), 'Is There an Atmosphere on the Moon?' <https://www.nasa.gov/mission_pages/LADEE/news/lunar-atmosphere.html>, updated 12 May 2013, accessed 7 Jul 2022.
- (2022a), 'NASA's Break the Ice Lunar Challenge. Lunar exploration requires vital resources – Including Water.' <<https://breaktheicechallenge.com/>>, accessed 24 Jun 2022.
- (2022b), 'VIPER Mission Overview' <<https://www.nasa.gov/viper/overview>>, updated 9 Sep 2022, accessed 27 Oct 2022.
- Nazzi Ehms, J. H., Césaró Oliveski, R. de, Oliveira Rocha, L. A. et al. (2019), 'Fixed Grid Numerical Models for Solidification and Melting of Phase Change Materials (PCMs)', *Applied Sciences*, 9/20: 4334.
- Nozette, S., Lichtenberg, C. L., Spudis, P. et al. (1996), 'The Clementine bistatic radar experiment', *Science (New York, N.Y.)*, 274/5292: 1495–1498.
- Parzinger, S. (2014), 'Analytische Modellierung der temperatur- und gasdruckabhängigen effektiven Wärmeleitfähigkeit von Pulvern', Dissertation (Munich, Technical University of Munich).
- Pelech, T. M., Roesler, G., and Saydam, S. (2019), 'Technical evaluation of Off-Earth ice mining scenarios through an opportunity cost approach', *Acta Astronautica*, 162/4: 388–404.
- Pereira, A., Makaya, A., and Cowley, A. (2020), *Building on the moon using additive manufacturing: a discussion of robotic approaches*.
- Pieters, C. M., Goswami, J. N., Clark, R. N. et al. (2009), 'Character and spatial distribution of OH/H₂O on the surface of the Moon seen by M3 on Chandrayaan-1', *Science (New York, N.Y.)*, 326/5952: 568–572.
- Pitcher, C., Kömle, N., Leibniz, O. et al. (2016), 'Investigation of the properties of icy lunar polar regolith simulants', *Advances in Space Research*, 57/5: 1197–1208.
- Reinecke, S. A., and Sleep, B. E. (2002), 'Knudsen diffusion, gas permeability, and water content in an unconsolidated porous medium', *Water Resour. Res.*, 38/12: 16-1-16-15.
- Reiss, P. (2018a), 'A combined model of heat and mass transfer for the in situ extraction of volatile water from lunar regolith', *Icarus*, 306/11: 1–15.
- (2018b), 'In-Situ Thermal Extraction of Volatiles from Lunar Regolith', Dissertation (Munich, Technical University of Munich (TUM)).
- Reiss, P., Warren, T., Sefton-Nash, E. et al. (2021), 'Dynamics of Subsurface Migration of Water on the Moon', *J Geophys Res Planets*, 126/5: 169.
- Sakatani, N., Ogawa, K., Arakawa, M. et al. (2018), 'Thermal conductivity of lunar regolith simulant JSC-1A under vacuum', *Icarus*, 309: 13–24.
- Salisbury, J. W., Basu, A., and Fischer, E. M. (1997), 'Thermal Infrared Spectra of Lunar Soils', *Icarus*, 130/1: 125–139.
- Sanin, A. B., Mitrofanov, I. G., Litvak, M. L. et al. (2017), 'Hydrogen distribution in the lunar polar regions', *Icarus*, 283/6963: 20–30.

- Sargeant, H. M., Barber, S. J., Anand, M. et al. (2021), 'Hydrogen reduction of lunar samples in a static system for a water production demonstration on the Moon', *Planetary and Space Science*, 205/5: 105287.
- Schieber, G. L., Jones, B. M., Orlando, T. M. et al. (2020), 'Advection diffusion model for gas transport within a packed bed of JSC-1A regolith simulant', *Acta Astronautica*, 169/20: 32–39.
- (2022), 'Indirect solar receiver development for the thermal extraction of H₂O(v) from lunar regolith: Heat and mass transfer modeling', *Acta Astronautica*, 190/3: 365–376.
- Schorghofer, N., and Taylor, G. J. (2007), 'Subsurface migration of H₂O at lunar cold traps', *J. Geophys. Res.*, 112/E2: 2375.
- Schreiner, S. S., Dominguez, J. A., Sibille, L. et al. (2016), 'Thermophysical property models for lunar regolith', *Advances in Space Research*, 57/5: 1209–1222.
- Sefton-Nash, E., Williams, J.-P., Greenhagen, B. T. et al. (2019), 'Evidence for ultra-cold traps and surface water ice in the lunar south polar crater Amundsen', *Icarus*, 332/20: 1–13.
- Seidel, A., Häming, M., and Monchinieri, E. (2021), *An Economically Viable Lunar ISRU Process for Oxygen and Metal Production and Related Benefits for Terrestrial Applications* (Dubai).
- Sesko, R. (2021), 'Structural-Thermal-Optical-Performance (STOP) analysis of a solar sintering mechanism for small lunar rovers', Semester Thesis (Munich, Technical University of Munich).
- Shulman, L. M. (2004), 'The heat capacity of water ice in interstellar or interplanetary conditions', *A&A*, 416/1: 187–190.
- Siegler, M., Aharonson, O., Carey, E. et al. (2012), 'Measurements of thermal properties of icy Mars regolith analogs', *J. Geophys. Res.*, 117/E3: n/a-n/a.
- Skonieczny, K., Wettergreen, D. S., and Whittaker, W. "R."L. (2016), 'Advantages of continuous excavation in lightweight planetary robotic operations', *The International Journal of Robotics Research*, 35/9: 1121–1139.
- Smith, M., Craig, D., Herrmann, N. et al., 'The Artemis Program: An Overview of NASA's Activities to Return Humans to the Moon', in , *2020 IEEE Aerospace Conference 2020*, 1–10.
- Smolka, A. (2021), 'Investigation of Transient Volatile Migration for the Lunar Volatile Scout', Semester Thesis (Munich, Technical University of Munich).
- Socio, L. M., and Marino, L. (2006), 'Gas flow in a permeable medium', *J. Fluid Mech.*, 557: 119.
- Song, H., Zhang, J., Ni, D. et al. (2021), 'Investigation on in-situ water ice recovery considering energy efficiency at the lunar south pole', *Applied Energy*, 298: 117136.
- Sowers, G. F. (2016), 'A cislunar transportation system fueled by lunar resources', *Space Policy*, 37: 103–109.
- (2021), 'The Business Case for Lunar Ice Mining', *New Space*, 9/2: 77–94.

- Sowers, G. F., and Dreyer, C. B. (2019), 'Ice Mining in Lunar Permanently Shadowed Regions', *New Space*, 7/4: 235–244.
- Spudis, P. D., Bussey, D. B. J., Baloga, S. M. et al. (2013), 'Evidence for water ice on the Moon: Results for anomalous polar craters from the LRO Mini-RF imaging radar', *J Geophys Res Planets*, 118/10: 2016–2029.
- Stebbins, J. F., Carmichael, I. S. E., and Moret, L. K. (1984), 'Heat capacities and entropies of silicate liquids and glasses', *Contr. Mineral. and Petrol.*, 86/2: 131–148.
- Svetsov, V. V., and Shuvalov, V. V. (2015), 'Water delivery to the Moon by asteroidal and cometary impacts', *Planetary and Space Science*, 117: 444–452.
- Swimm, K., Reichenauer, G., Vidi, S. et al. (2009), 'Gas Pressure Dependence of the Heat Transport in Porous Solids with Pores Smaller than 10 μm ', *Int J Thermophys*, 30/4: 1329–1342.
- Taylor, L. A., and Meek, T. T. (2005), 'Microwave Sintering of Lunar Soil: Properties, Theory, and Practice', *J. Aerosp. Eng.*, 18/3: 188–196.
- Tjaden, B., Cooper, S. J., Brett, D. J. L. et al. (2016), 'On the origin and application of the Bruggeman correlation for analysing transport phenomena in electrochemical systems', *Current Opinion in Chemical Engineering*, 12: 44–51.
- Toutanji, H., Goff, C. M., Ethridge, E. et al. (2012), 'Gas permeability and flow characterization of simulated lunar regolith', *Advances in Space Research*, 49/8: 1271–1276.
- Tye, A. R., Fassett, C. I., Head, J. W. et al. (2015), 'The age of lunar south circumpolar craters Haworth, Shoemaker, Faustini, and Shackleton: Implications for regional geology, surface processes, and volatile sequestration', *Icarus*, 255/6003: 70–77.
- Vasavada, A. R., Bandfield, J. L., Greenhagen, B. T. et al. (2012), 'Lunar equatorial surface temperatures and regolith properties from the Diviner Lunar Radiometer Experiment', *J. Geophys. Res.*, 117/E12: n/a-n/a.
- Vendiola, V., Zacny, K., Morrison, P. et al. (11152018), 'Testing of the Planetary Volatiles Extractor (PVEx)', in R. B. Malla, R. K. Goldberg, and A. D. Roberts (eds.), *Earth and Space 2018* (Reston, VA: American Society of Civil Engineers), 467–80.
- Vetcha, N., Roman, M. C., Fiske, M. et al. (10242022), 'Overview of NASA's Break the Ice Lunar Challenge Phase 1', in , *ASCEND 2022* (Reston, Virginia: American Institute of Aeronautics and Astronautics).
- Vorhauer-Huget, N., Mannes, D., Hilmer, M. et al. (2020), 'Freeze-Drying with Structured Sublimation Fronts—Visualization with Neutron Imaging', *Processes*, 8/9: 1091.
- Vosteen, H.-D., and Schellschmidt, R. (2003), 'Influence of temperature on thermal conductivity, thermal capacity and thermal diffusivity for different types of rock', *Physics and Chemistry of the Earth, Parts A/B/C*, 28/9-11: 499–509.
- Wasilewski, T. G. (2021a), 'Experimental Investigations of Water Extraction Process within Permanently Shadowed Regions of the Moon', 2021: 698–712.

- (2021b), 'Lunar thermal mining: Phase change interface movement, production decline and implications for systems engineering', *Planetary and Space Science*, 199: 105199.
- Watson, K. (1964), 'I. The thermal conductivity measurements of selected silicate powders in vacuum from 150°-350° K. II. An interpretation of the Moon's eclipse and lunation cooling as observed through the Earth's atmosphere from 8-14 microns', Dissertation (California Institute of Technology).
- Watson, K., Murray, B., and Brown, H. (1961), 'On the possible presence of ice on the Moon', *J. Geophys. Res.*, 66/5: 1598–1600.
- Webb, S. W. (1996), *Gas-phase diffusion in porous media: Evaluation of an advective-dispersive formulation and the dusty-gas model including comparison to data for binary mixtures*.
- Williams, D. R. (2021), 'Moon Fact Sheet' <<https://nssdc.gsfc.nasa.gov/planetary/factsheet/moonfact.html>>, updated 20 Dec 2021, accessed 7 Jul 2022.
- Williams, J.-P., Greenhagen, B. T., Paige, D. A. et al. (2019), 'Seasonal Polar Temperatures on the Moon', *J Geophys Res Planets*, 124/10: 2505–2521.
- Wood, S. E. (2020), 'A mechanistic model for the thermal conductivity of planetary regolith: 1. The effects of particle shape, composition, cohesion, and compression at depth', *Icarus*, 352: 113964.
- Woodside, W., and Messmer, J. H. (1961), 'Thermal Conductivity of Porous Media. I. Unconsolidated Sands', *Journal of Applied Physics*, 32/9: 1688–1699.
- Woods-Robinson, R., Siegler, M. A., and Paige, D. A. (2019), 'A Model for the Thermophysical Properties of Lunar Regolith at Low Temperatures', *J Geophys Res Planets*, 124/7: 1989–2011.
- Zacny, K., Chu, P., Paulsen, G. et al. (09112012), 'Mobile In-Situ Water Extractor (MISWE) for Mars, Moon, and Asteroids In Situ Resource Utilization', in , *AIAA SPACE 2012 Conference & Exposition* (Reston, Virginia: American Institute of Aeronautics and Astronautics), 345.
- Zacny, K., Indyk, S., and Luczek, K. (2016), *Planetary Volatiles Extractor (PVEx) for In Situ Resource Utilization (ISRU)*.
- Zhang, X., Sun, P., Yan, T. et al. (2015), 'Water's phase diagram: From the notion of thermodynamics to hydrogen-bond cooperativity', *Progress in Solid State Chemistry*, 43/3: 71–81.

B Appendices

B.1 Lunar Regolith Thermal conductivity model according to Parzinger (2014) and Reiß (2018)

In his dissertation, after analyzing nearly 60 thermal conductivity models, Parzinger (2014) created a semi-empirical approach and developed a model that additionally taking not only the gas conductivity k_g into account, but also the coupling of solid and gas conduction k_{sg} , resulting in:

$$k_{dry} = k_{sc} + k_{rad} + k_g + k_{sg} \quad (\text{B—1})$$

with the physical contact conduction k_{sc} , the radiation between the particles k_{rad} , the conduction through the gas in between the particles k_g as well as the coupling of solid and gas conduction k_{sg} .

Physical contact conduction considers the area between the particles, though with heat is transferred and thus depends mostly on the mechanical properties of the regolith (Parzinger 2014):

$$k_{sc} = 3.44 \cdot (1 - \varphi)^{\frac{4}{3}} \left(\frac{1 - \vartheta^2}{Y} \right)^{\frac{1}{3}} k_s p_s^{\frac{1}{3}} \quad (\text{B—2})$$

with the Poisson ratio ϑ , Young's modulus Y , the thermal conductivity of the solid material k_s , and the pressure or load on the particle p_s .

The load can be calculated by integrating the weight of the soil above:

$$p_s = g \cdot \int_0^z \rho_s dz \quad (\text{B—3})$$

with the density ρ_s and the gravitational acceleration g .

The conductivity of the solid material can for example be evaluated using the general equation for the thermal conductivity of rocks (Vosteen and Schellschmidt 2003; Reiss 2018a):

$$k_s = \frac{C_1}{350^\circ\text{C} + T} + C_2 \quad (\text{B—4})$$

For this formula, the temperature is to be inserted in °C. C_1 and C_2 are fitting parameters depending on the rock type. Common values for those parameters include $C_1 = 750$ and $C_2 = 0.75$ for metamorphic rocks, $C_1 = 807$ and $C_2 = 0.64$ for acid rocks, $C_1 = 474$ and $C_2 = 1.18$ for basic rocks, $C_1 = 1293$ and $C_2 = 0.73$ for ultrabasic rocks, and $C_1 = 1073$ and $C_2 = 0.13$ for limestone. A fit for the Apollo 16 sample 68501 results in $C_1 = 0.50$ and $C_2 = 0.38$. (Reiss 2018a). These values lead to thermal conductivities in the range of $\sim 2 \text{ W/mK}$ to $\sim 10 \text{ W/mK}$ between 100 K and 400 K. Investigating the effects of the two factors C_1 and C_2 on the thermal conductivity of the solid part of the lunar soil k_s shows, that the parameters for the Apollo 16 sample result in a conductivity up to two orders of magnitudes lower than the other possibilities, particularly in low temperature and low pressure regions. This phenomenon is thought to be caused by the sample's high agglutinate content, which was generated by the melting and

outgassing of solar wind-implanted particles to form glassy breccia with vesicles. (Reiss 2018a)

The radiative term k_{rad} , which is the second of equation (4—16), is dependent on the real part of the complex effective refractive index n :

$$n^2 = n_f^2 \cdot \left(\frac{3(1 - \theta) \cdot \frac{n_s^2 - n_f^2}{n_s^2 + 2n_f^2}}{1 - (1 - \theta) \frac{n_s^2 - n_f^2}{n_s^2 + 2n_f^2}} \right) \quad (\text{B—5})$$

where n_s and n_f are refractive indices of the fluid and the solid respectively (Parzinger 2014). The radiative conduction thus can be calculated by:

$$k_{rad} = \frac{16\sigma n^2}{3E} \cdot T^3 \quad (\text{B—6})$$

with the Stefan-Boltzmann constant σ , the extinction coefficient E , and the real part of the complex effective refractive index n .

The third term, the gas conductivity k_{gas} is mainly dependent on the gas pressure and thus Knudsen Number Kn . The Knudsen number is used to differentiate between ordinary and Knudsen diffusion. While there is no exact definition of the boundary between these two mechanisms it is commonly said that for $Kn \ll 0.1$, where the void spaces are much larger than the mean free path, ordinary diffusion is the dominating diffusion process. Accordingly, for $Kn \gg 1.10$ Knudsen diffusion dominates. (Reiss 2018a)

For $Kn < 10$, the Smoluchowski effect is responsible for a decreasing Knudsen Number while the gas conductivity is increasing (Griesinger et al. 1999):

$$k_g = \frac{k_{g,0}}{1 + 2\beta \cdot Kn} \quad (\text{B—7})$$

with the gas thermal conductivity at atmospheric pressure $k_{g,0}$, the gas specific constant β (~1.41 for water at 373.2 K (Griesinger et al. 1999)) and the Knudsen Number

$$Kn = \frac{\lambda}{d_v} \quad (\text{B—8})$$

with the mean free path λ and the diameter of the void spaces between the particles d_v . The former can be calculated as

$$\lambda = \frac{k_B T}{\sqrt{2} p \pi d_g^2} \quad (\text{B—9})$$

with the Boltzmann constant k_B , the temperature T , the pressure p , and the effective diameter of a gas molecule d_g .

The interaction between the solid and the gas results in the final term k_{sg} . The model developed by Swimm et al. (2009) can be used to assess this contribution to the overall conductivity. This approach discretizes the contact area using 1000 hollow cylinders

and an additional shape factor to contribute to the deviation from perfectly spherical contact zones, which is resulting in the term:

$$k_{sg} = (1 - \varphi_{uc}) \frac{2r}{r^2 \pi} \sum_{i=1}^{1000} \left(\frac{h_{g,i}}{k_{gas,i} A_i} + \frac{h_{s,i}}{k_s A_i} \right)^{-1} \quad (\text{B—10})$$

with the particle radius r . All additional factors can be calculated as follows:

$$\theta_{uc} = \frac{1}{2} (3\theta - 1) \quad (\text{B—11})$$

$$a = \frac{d}{2} F_{ell}^{-\frac{1}{3}} \quad (\text{B—12})$$

$$b = \frac{d}{2} F_{ell}^{\frac{2}{3}} \quad (\text{B—13})$$

$$h_{s,i} = 2r - 2b \cdot \left(1 + \sqrt{1 - \left(\frac{i}{a} \frac{r}{1000} \right)^2} \right) \quad (\text{B—14})$$

$$h_{g,i} = 2r - h_{s,i} \quad (\text{B—15})$$

$$A_i = \pi \left(\frac{r}{1000} \right)^2 \cdot (2i - 1) \quad (\text{B—16})$$

Comparing the particle shapes of lunar soil samples and the simulant JSC-1A, the shape factor $F_{ell} = 0.6$ can be assumed (Parzinger 2014).